SANDIA REPORT

SAND2010-0326
Unlimited Release
Printed January 2010

Phonon Engineering for Nanostructures

Subhash L. Shinde, Edward S. Piekos, John P. Sullivan, Thomas A. Friedmann, David H. Hurley, Sylvie Aubry, Diane E. Peebles, and John A. Emerson

Prepared by
Sandia National Laboratories
Albuquerque, New Mexico 87185 and Livermore, California 94550

Sandia is a multiprogram laboratory operated by Sandia Corporation, a Lockheed Martin Company, for the United States Department of Energy under Contract DE-AC04-94AL85000

Issued by Sandia National Laboratories, operated for the United States Department of Energy by Sandia Corporation.

Printed in the United States of America. This report has been reproduced directly from the best available copy.

Available to DOE and DOE contractors from
U.S. Department of Energy
Office of Scientific and Technical Information
P.O. Box 62
Oak Ridge, TN 37831

Telephone: (865)576-8401
Facsimile: (865)576-5728
E-Mail: reports@adonis.osti.gov
Online ordering: http://www.osti.gov/bridge

Available to the public from
U.S. Department of Commerce
National Technical Information Service
5285 Port Royal Rd
Springfield, VA 22161

Telephone: (800)553-6847
Facsimile: (703)605-6900
E-Mail: orders@ntis.fedworld.gov
Online order: http://www.ntis.gov/help/ordermethods.asp?loc=7-4-0#online

SAND2010-0326
Unlimited Release
Printed January 2010

Phonon Engineering for Nanostructures

Subhash L. Shinde (PI)
Advanced Microsystems Packaging Department

Edward S. Piekos
Microscale Science and Technology Department

John P. Sullivan
CINT Science Department

Thomas A. Friedmann
Nanomaterials Sciences Department

David H. Hurley
Idaho National Laboratory

Sylvie Aubry
Stanford University

Diane E. Peebles (PM)
Nanomaterials Sciences Department

John A. Emerson
Organic Materials Department

Sandia National Laboratories
P. O. Box 5800
Albuquerque, NM 87185-0352

Abstract

Understanding the physics of phonon transport at small length scales is increasingly important for basic research in nanoelectronics, optoelectronics, nanomechanics, and thermoelectrics. We conducted several studies to develop an understanding of phonon behavior in very small structures. This report describes the modeling, experimental, and fabrication activities used to explore phonon transport across and along material interfaces and through nanopatterned structures. Toward the understanding of phonon transport across interfaces, we computed the Kapitza conductance for Σ29(001) and Σ3(111) interfaces in silicon, fabricated the interfaces in single-crystal silicon substrates, and used picosecond laser pulses to image the thermal waves crossing the interfaces. Toward the understanding of phonon transport along interfaces, we designed and fabricated a unique differential test structure that can measure the proportion of specular to diffuse thermal phonon scattering from silicon surfaces. Phonon-scale simulation of the test ligaments, as well as continuum scale modeling of the complete experiment, confirmed its sensitivity to surface scattering. To further our understanding of phonon transport through nanostructures, we fabricated microscale-patterned structures in diamond thin films.

Acknowledgments

This work was performed under the Laboratory-Directed Research and Development (LDRD) program at Sandia National Laboratories (project 105906) and was also supported by the Center for Integrated Nano-Technologies (CINT), a U.S. Department of Energy, Office of Science Nanoscale Science Research Center (NSRC) national user facility. Experimental assistance by Don Bethke, John Nogan, David Pietrzak, and Doug Pete is gratefully acknowledged. We also thank Jonathan Rivera for help with the diamond growth and characterization, Nancy Missert for use of her SEM and XRD system, Art Spaltenstein for assistance in preparing specimens, Catalina Ahlers for bonding of the silicon wafers, and Rhonda Reinert for patiently compiling all the available and scattered results into a single highly readable report.

Contents

Figures

Table

Nomenclature

AM	acoustic-mismatch
APS	American Physical Society
ASIC	application-specific integrated circuit
BEN	bias-enhanced nucleation
BTE	Boltzmann transport equation
CINT	Center for Integrated Nano-Technologies
CMOS	complementary metal oxide semiconductor
CVD	chemical vapor deposition
cw	continuous wave
DM	diffuse-mismatch
DSMC	direct simulation Monte Carlo
EELS	electron energy-loss spectroscopy
FIB	focused-ion-beam
FWHM	full-width at half maximum
GaN	gallium nitride
H	hydrogen
HF	hydrofluoric acid
INL	Idaho National Laboratory
Ir	iridium
LA	longitudinal acoustic
LDRD	Laboratory-Directed Research and Development
LO	longitudinal optical
MC	Monte Carlo
MD	molecular dynamics
MEMS	microelectromechanical systems
MRS	Materials Research Society
PLD	pulsed laser deposition
SAW	surface acoustic wave
SEM	scanning electron microscopy, scanning electron microscope
Si	silicon
SOI	silicon-on-insulator
SRH	Shockley-Read-Hall
SW	Stillinger-Weber
TA	transverse acoustic
TEM	transmission electron microscopy
XRD	X-ray diffraction
YSZ	yttria stabilized zirconia

Phonon Engineering for Nanostructures

1 Introduction

Understanding the physics of phonon transport at small length scales is increasingly important for fundamental advances in nanoelectronics, optoelectronics, nanomechanics, and thermoelectrics. Such understanding is also critical for larger-scale device technologies that are pushing the limits of thermal engineering. For example, power densities in high-power gallium nitride (GaN) devices are reaching values in excess of 500 W/cm^2. Optimal "thermal spreading" is thus critical for device performance and longevity. With the dimensions of complementary metal oxide semiconductor (CMOS) devices and the device layers in silicon-on-insulator (SOI) wafers now approaching 100 nm, an understanding of phonon transport is required to enable the optimal design of a widening variety of current and future devices.

The importance of phonon transport to a cross section of scientists and engineers is growing, as evidenced by the increasing number of publications and new symposia about the topic. Still, large gaps exist in our knowledge of phonon transport with arbitrary interfaces, crystal defects, delocalized electrons/collective electronic excitations, and solid acoustic vibrations, to name a few. Closing these gaps will enable the creation of structures that provide novel thermal solutions, such as phonon wave-guides, as well as open design space in nanoscale electronics and nanomechanics.

The goal of this LDRD project, conducted from fiscal year (FY) 2007 through FY 2009, was to develop an understanding of phonon transport at small length scales through experiments on idealized test structures combined with advances in modeling. The project involved a tight coupling between sensitive experiments on specially prepared structures and simulation at multiple scales. The experiments included ultrafast laser-based imaging of phonon transport across precisely-defined grain boundaries and a unique test platform for assessing phonon-surface interactions. The simulations ranged from molecular dynamics modeling of grain boundaries to Monte Carlo modeling of nanoscale structures to continuum modeling of entire experiments. Practical benefits of this work include thermal management of high-power devices, harvesting of thermal energy, the creation of novel acoustic-wave devices for sensing or signal processing and the promise of a whole new class of phonon-engineered devices where microscale effects are enabling features.

1.1 Technical Approach

Phonon interaction modes can be emphasized or attenuated by modifying the geometry, materials, and temperature. For example, thermal conductivity in bulk materials at room temperature is dominated by phonon-phonon and phonon-impurity interactions. As structures shrink to the nanoscale, confinement effects can change the dispersion relation that dictates available phonon modes [1]. Introducing material interfaces can also drastically affect phonon transport due to effects stemming from mismatched dispersion relations and the atomic structure of the interfaces [2]. As for light, periodic structures have been shown to introduce phonon band

gaps, or forbidden frequencies, as well as the ability to redirect low-frequency surface phonons in a low-loss fashion.

To exploit these mechanisms for engineering purposes, they must be understood at a deeper level than is currently available. The research performed in this project involved a concurrent computational and experimental investigation of these effects, with each technique guiding refinement of the other until they were in agreement and a predictive capability was established. With this knowledge in hand, we studied increasingly complex structures, leading to demonstration of ~~"p~~phonon engineered" systems.

The study of phonon transport in nanoscale structures is important for understanding and using nanoscale and nanostructured materials in diverse applications. The problem is one of characterizing the interaction of phonons with interfaces in the material. Thus, our project focused on three areas of investigation: (1) developing an understanding of phonon transport across interfaces, (2) developing an understanding of phonon transport along interfaces, and (3) developing and patterning epitaxial diamond thin films to study phonon transport in confined structures. Note that the term ~~"i~~nterface" is used interchangeably with the term ~~"b~~oundary" throughout this report.

1.2 Document Overview

Section 1 has provided an overview of the project's goal and technical approach. Section 2 discusses the modeling, experimental, and measurement activities that were performed to gain an understanding of phonon transport across interfaces. In Section 3, we describe the activities pursued to gain an understanding of phonon transport along interfaces. Section 4 documents the modeling and experimental activities used to develop and pattern epitaxial diamond thin films. A summary of the project's significant accomplishments, communications, issues, and future opportunities follows in Section 5.

Additional detailed studies written by team members about their various contributions to the project form the contents of the appendices. These appendices expand on the activities discussed in the body of the report. Appendix A compares theoretical and simulation-based predictions of grain-boundary Kapitza conductance in silicon, and includes calculations performed to compute the Kapitza conductance in silicon/silicon dioxide systems. This appendix supplements the modeling and simulation work discussed in Section 2. Appendix B describes a calculation that impacted the sample design and measurement method employed in the investigation of phonon transport across interfaces discussed in Section 2. Appendix C and Appendix D are published papers explaining detailed experimental studies conducted to image carrier and phonon transport in silicon using ultrashort optical pulses. The experiments were part of a successful effort to measure phonon transport across interfaces and supported the investigation discussed in Section 2. Appendix E discusses the modified Holland model that was used to model phonon-phonon and phonon-impurity scattering in the Monte Carlo simulations. These scattering mechanisms control the bulk thermal conductivity as a function of temperature in the material and are thus a critical part of any simulation in a geometry of nonvanishing size at nonvanishing temperature. These simulations were a part of the investigation of phonon transport along interfaces discussed in Section 3. Appendix F provides additional details about the modeling work described in

Section 3 to gain further understanding of transport along interfaces by assessing phonon-surface interaction.

Note that references are included separately for each section and appendix, where applicable. Further, the presentation of an individual appendix either follows the format of this document or, in the case of published papers, retains the basic format of its original publication.

1.3 References

[1] A. Balandin. ―Thermal conductivity of semiconductor low-dimensional structures."*Phys. Low-Dim Structures* 1–2: 1 (2000).

[2] G. Chen. A. Narayanaswamy, and C. Dames. ―Engineering nanoscale phonon and photon transport for direct energy conversion." *Superlattices and Microstructures* 35, 161–172 (2004).

2 Phonon Transport Across Interfaces

Section 2 describes our investigation of phonon transport across interfaces, a mechanism that can be applied to polycrystalline materials and superlattices. We wanted to explore phonon scattering across boundaries, as depicted in Figure 2-1.

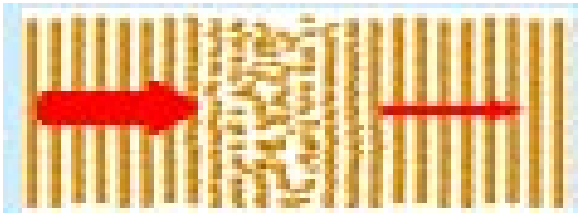

Figure 2-1. Phonon scattering across boundaries.

The objective of our study was to develop an experimental system involving specimens with well-defined boundaries in silicon so that we could measure phonon transport across the boundaries at a wide range of temperatures. The atomic structure of many of these boundaries has been well characterized using techniques like high-resolution transmission electron microscopy (HRTEM), and these data were used in the molecular dynamics models that guided this study to simulate phonon transport across the boundaries. The interfaces of interest were the Σ3(111) boundary and the Σ29(001) boundary. Molecular dynamics simulations enable the investigation of detailed atomic-scale effects, such as interface and impurity scattering. Basically, we sought to model the phonon transport across these boundaries, fabricate the boundaries in the laboratory, characterize the fabricated specimens, and measure the phonon transport across the fabricated specimens with a sensitive measurement technique.

Section 2.1 introduces concepts relevant to the modeling performed for this study. Section 2.2 describes the modeling activities that contributed to our understanding of phonon transport across boundaries and impacted the design of the experimental system. Section 2.3 describes the process we followed to fabricate the boundaries. Characterization and measurement of the boundaries are discussed in Section 2.4. Although some of the activities in Sections 2.2 through 2.4 were conducted in parallel, they are discussed separately herein. Section 2.5 lists the references cited in this work.

2.1 Introduction

Molecular dynamics simulations can be used to compute the Kapitza conductance of material geometry (like dislocations, defects, grain boundaries etc.). This is most often done using the direct heat flux method or the lattice dynamics method. In the direct heat flux approach, a heat current is applied and the time-averaged temperature gradient is computed. The thermal conductivity is then obtained from Fourier's law of thermal conduction at a given system length; the thermal conductivity can be deduced from the temperature gradient. An extrapolation over an entire sample length is necessary to determine the thermal conductivity of a bulk crystal in a given crystal direction at a given temperature.

The basic idea behind the lattice dynamics method is to create localized wave packets through a superposition of normal modes of a bulk perfect crystal. The wave packets are then propagated using molecular dynamics simulation. After interacting with an interface, the energy transmission coefficient is determined for each polarization and wave vector as the fraction of incident energy that propagates across the interface. The Kapitza conductance can then be determined from the energy transmission coefficient, the phonon group velocity, and the dispersion relation. The direct heat flux method is used to obtain a value for the thermal conductivity or Kapitza conductance at a given temperature, while the lattice dynamics method is often used to obtain a better description of interfacial phonon scattering for a range of temperatures.

2.2 Modeling and the Stack Design

The activities discussed below demonstrate how molecular dynamics simulations were tightly coupled to the design and evolution of the physical experimental system. Modeling influenced and was influenced by the fabrication process.

2.2.1 Calculation of Kapitza Conductance

We performed molecular dynamics simulations to determine the transmission coefficients for acoustic phonons at all frequencies and angles of incidence on a silicon Σ3(111) grain boundary. From this information, the Kapitza conductance was calculated. The results from our calculations of the Kapitza conductance are shown in Figure 2-2 compared to a similar result from a Σ29(001) boundary characterized by work in a previous project. We found that the Σ3(111) boundary is more ordered than the Σ29(001), so its higher conductance was expected. We were surprised, however, that the difference was not large. These calculations gave a good idea of the upper and lower bounds for phonon scattering from silicon-silicon (Si-Si) boundaries.

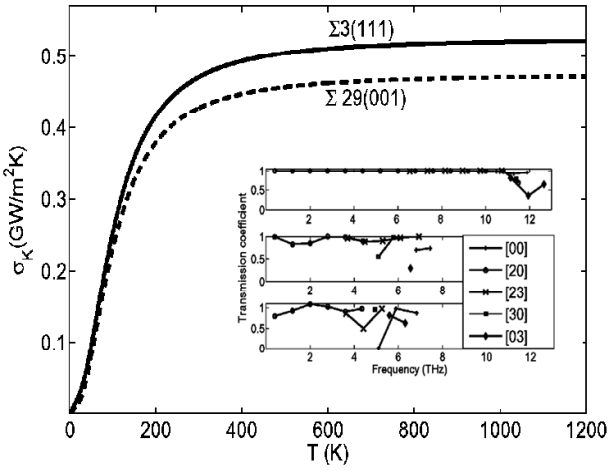

Figure 2-2. Kapitza conductance vs. temperature for two silicon grain boundaries determined from calculated phonon transmission coefficients.

2.2.2 Further Investigations of the Kapitza Conductance

We compared heat-flux molecular dynamics results to theoretical calculations based on wave-packet molecular dynamics results for the Kapitza conductance of the two grain boundaries of interest in silicon. We found a much higher conductance for the Σ3(111) twin boundary than for the Σ29 (001) grain boundary. The results from the two methods showed reasonable agreement for the Σ29(001) grain boundary, but disagreement by a factor of about 10 for the Σ3(111) boundary. Appendix A, Section A.1 presents a published paper describing this work. In this paper, a new formulation is proposed for computing the Kapitza conductance.

In another investigation, we studied the Kapitza conductance of several Si-SiO_2 interfaces, including α-quartz, β-quartz, cristobalite, and tridymite. We computed the Kapitza conductance of an Si-SiO_2 interface where Si-SiO_2 is α-quartz at 300 K. The thermal conductivity was estimated to be 3.2 GW/M^2 K, which was comparable to the value obtained by Mahajan et al. [1]. See Appendix A, Section A.2 for a detailed description of our study.

2.2.3 Genesis of the Stack Design

Our modeling of the Kapitza conductance indicated that the difference between the thermal conductivity of the two boundaries, Σ3(111) and Σ29(001), was small. For this reason, we decided to fabricate high-quality twist boundaries by wafer-bonding stacks of 10 to 20 thin (<100 m) silicon wafers with known twist angle to produce multiple boundaries and increase the measurement sensitivity. Figure 2-3 provides examples of two twist boundary sets. We planned to use laser flash measurements for estimating the overall thermal conductivity of specimens with well-defined twist boundary stacks.

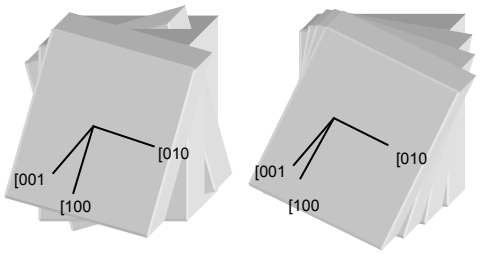

Figure 2-3. Examples of flipped or chiral twist boundary sets.

2.2.4 Development of a Twisted Stack Model

To test the feasibility of the new design, we developed a model for the twist boundary stack that calculates the predicted thermal conductivity of a stack as a function of the number of layers, temperature, layer thickness, etc. We used this information to determine the measurement system requirements. For the baseline design of a stack of ten 100 m silicon layers twisted into a Σ29 configuration, the analysis showed that the measurement system must resolve a difference of only 0.4 W/m K at room temperature, which would be a severe challenge to resolve using the planned laser flash measurement. We found that our proposed stack design of 10 layers could not produce a thermal conductivity that was sufficiently different from the baseline (untwisted) case

to be discernable by laser flash measurements and other available measurement techniques. See Appendix B for a description of the model.

2.2.5 Consideration of Alternate Approaches

The results of the twist boundary stack model led us to consider an alternative approach to measuring the twisted stacks. We designed an alternative to through-the-stack measurement that relies on the difference in heat spreading in 2-D structures with and without interfacial resistance in an effort to increase measurability. The stack is placed on a large heat sink and a small heater is placed on top of it. We compared the temperature distribution in one simulation where there is no interfacial resistance with a simulation where there is considerable thermal resistance between the layers. The temperature measured on the upper surface at a given point would differ in the two cases because the interfacial resistance causes greater lateral heat spreading. However, the simulations showed that this difference was likely too small to reliably measure, and thus the alternative approach was abandoned.

The results of the twist boundary stack model also led us to develop another approach to fabricating the twist boundary stacks, This second approach consisted of multiple-stacked controlled silicon-silicon dioxide-silicon (Si-SiO_2-Si) interfaces, whereas the first approach consisted of multiple-stacked Si-Si interfaces. (See Section 2.3 for fabrication details.)

2.3 Fabrication of Twist Boundaries

When it became clear from the modeling (described in Section 2.2.3) that multiple-stacked Si-Si interfaces would be difficult to measure experimentally, we decided to focus on individual twist boundaries in silicon single-crystal wafers and identify picosecond laser-based technique(s) for measuring the Kapitza resistance of the individual boundaries. Toward the end of the project, we also bonded Si and SiO_2 surfaces to create Si-SiO_2-Si boundaries for our studies.

As mentioned previously, there are a host of special boundaries that have been well characterized and a very detailed understanding of the atomic arrangements at the boundaries has been developed based on coincident site lattice (CSL) models [2]. For this study, we selected a highly ordered (Σ3 boundary) structure and a highly disordered (Σ29 boundary) structure. The Σ3 structure is essentially a twin boundary created by twisting a (111) crystallographic surface with respect to the other by 60 degrees. The Σ29 structure is a disordered boundary created by twisting one (100) surface with respect to the other by 43.6 degrees. This is very convenient since silicon single-crystal wafers can be purchased with (100), (110), or (111) crystallographic surface orientations. The wafers are mirror polished and generally have a very thin oxide (SiO_2) layer. The wafer-to-wafer bonding therefore required techniques for (1) precise rotation of one wafer respect to the other, (2) surface cleaning and activation procedures to remove all the surface oxide, followed by hydrogen (H) termination of the surfaces to be bonded, and (3) bonding at low temperatures (< 200°C) followed by high-temperature annealing in a reducing ambient to drive off any remaining surface oxide layer at the bonded interface.

Initially, we conducted experiments that focused on optimizing the wafer-bonding processes to yield void-free bonds across multiple wafers. The two interface types (Si-Si and Si-SiO_2-Si) required different approaches. A schematic of the process for Si-SiO_2-Si stacks is shown in

Figure 2-4. We were able to fabricate up to five layer stacks with this approach. We carried out similar process steps (with some modifications) for Si-Si bonding, with the addition of an HF etch to remove the surface oxide.

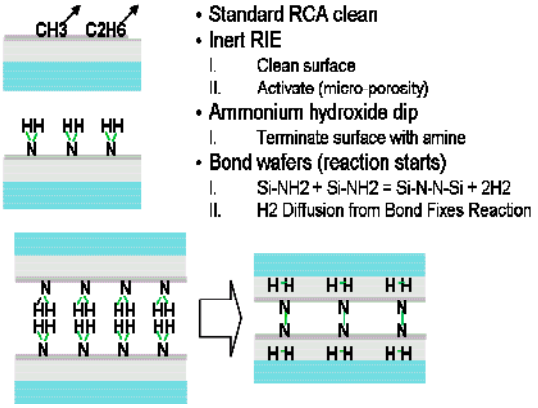

Figure 2-4. Bonding process for Si-SiO_2-Si interfaces.

We studied the quality of the bonds using scanning acoustic microscopy. This technique is depth sensitive, allowing for examination of all interfaces. As shown in Figure 2-5, the bond quality at the interfaces for these initial experiments was not optimal for Si-SiO_2 or for Si-Si bonds. Based on these results, we made process modifications aimed at producing fewer voids.

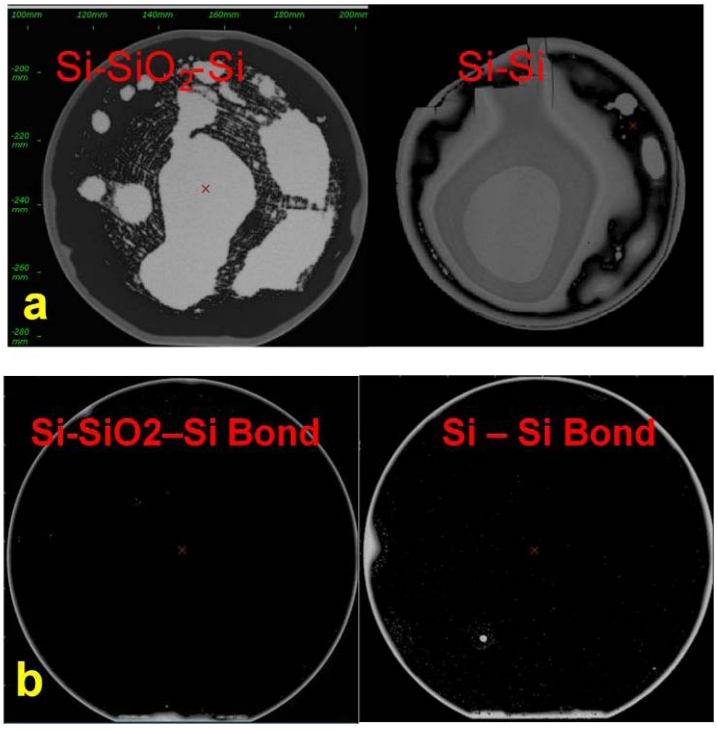

Figure 2-5. (a) Interface voids in earlier bonded wafers and (b) Void-free bonding with improved processing.

Subsequently, we carried out extensive experimental work to optimize the fabrication process for creating twist boundaries with known orientation from silicon single crystals. This work involved developing various surface-activation techniques and special processing to remove any surface oxide, careful fixturing to create precise rotation between the bonded wafers, and optimization of the annealing to remove any oxygen from the interface. We then performed acoustic imaging of the interface to locate the voids. Specimens were diced from void-free regions and mirror polished edge-on to prepare the surface for measurements.

2.4 Characterization and Measurement

We completed fabrication of the Σ29(001) and Σ3(111) boundaries using the newly developed alignment and bonding process, and conducted electron backscatter diffraction measurements to characterize the bicrystal interface. Inverse pole diagrams showing the crystal orientation in false color for the Σ3 and Σ29 boundaries are shown in Figures 2-6(a) and 2-6(b), respectively. The boundary demarcation for the coherent twin boundary (Σ3) is difficult to distinguish, whereas the boundary demarcation is obvious for the twist boundary (Σ29).

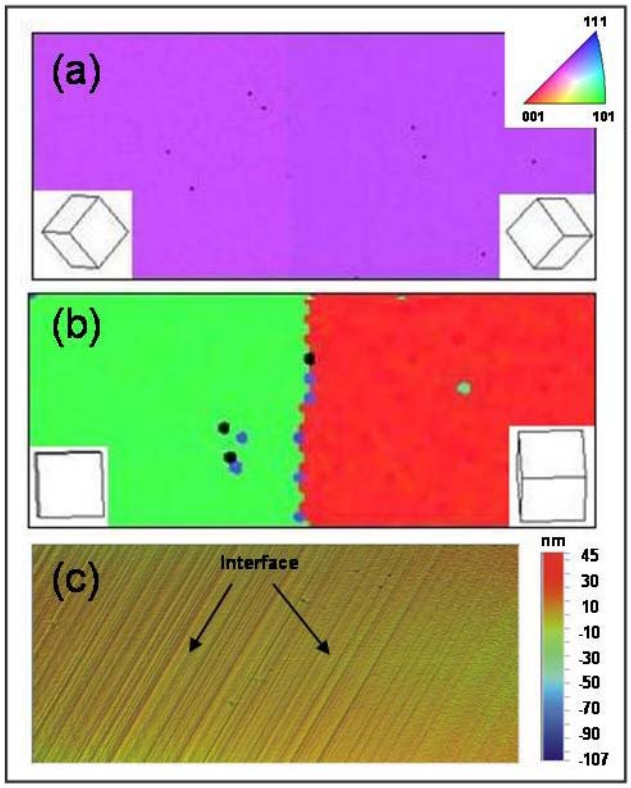

Figure 2-6. (a) and (b): Crystal orientation shown in false color for the Σ3 and the Σ29 boundaries respectively; (c): optical profilometry of the boundary region.

In addition to characterizing the crystal misorientation across the bicrystal boundary it is important to visualize changes in topography of the sample surface near the boundary region. In

a previous study it was shown that these changes in topography associated with polishing can greatly influence laser-based thermal diffusivity measurements. For the samples in this phonon transport study, the surface was polished using diamond paste to avoid preferential etching near the boundary region. Figure 2-6(c) shows an optical profilometry micrograph of the boundary region of the sample surface. Using electron backscatter data and prominent surface features such as scratches as fiducial marks, the faint line across the center of this image is identified as the bicrystal interface. This image confirms that the polishing method did not preferentially etch the boundary region eliminating any significant changes in topography.

We sent fabricated Si-Si specimens to Dr. David Hurley of Idaho National Laboratory to measure the phonon transport flow across their boundaries using ultrafast laser pulse imaging. His imaging technique uses a pump-and-probe laser with a pulse width around one picosecond. The probe laser, operating at similar frequencies, is able to resolve the propagation of the diffusive and acoustic phonon components as a function of distance. The measured Kapitza resistance of a sample Σ29 specimen was much larger than predicted for a perfect interface, an issue that became more understandable in the HRTEM results discussed next. Appendices C and D contain two published papers that discuss the imaging technique used to measure our specimen.

Additionally we carried out cross-sectional HRTEM of the measured Σ29 boundary to verify the orientation across the boundary and also to establish the presence of any second phase. Figure 2-7 shows these results. Figures 2-7a and 2-7b depict the orientation change in going from one side of the boundary to the other. The <100> directions of the two crystals are misoriented by $43.5° \pm 0.1°$, which is the misorientation needed to create the Σ29 boundary. The bright field image (2-7c), and the high-resolution image (2.7d) show that there is a second phase at this interface. The extent of this region was determined to be about 4 nm. We also carried out electron energy-loss spectroscopy (EELS) using a probe size of 2 nm. The EELS peak positively identified this phase as SiOx (silicon oxide). Its stoichiometry cannot be fully determined by this technique, however, since the specimens were annealed at 1000°C, we believe that it is SiO_2. The presence of this phase at the Σ29 interface explains why the Kapitza resistance of this boundary is higher than that calculated using molecular dynamics simulations.

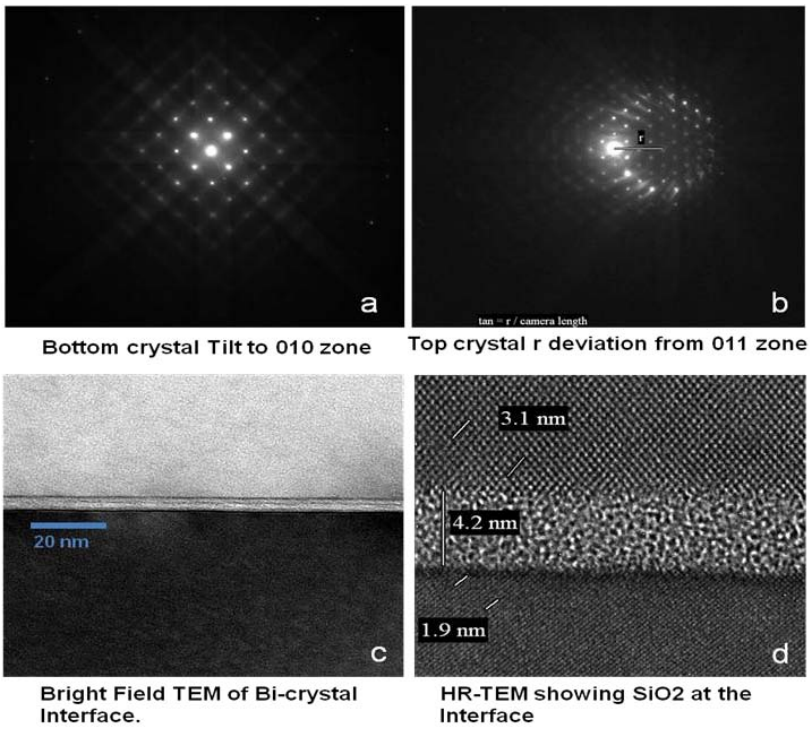

Figure 2-7. Cross-sectional TEM on Σ29 boundary

2.5 Summary

In our investigation of phonon transport across interfaces, we computed the Kapitza conductance for Σ29(001) and Σ3(111) boundaries in silicon and proposed a new formulation for computing the Kapitza conductance. We fabricated these boundaries in single-crystal silicon substrates and imaged thermal waves crossing the boundaries using picosecond laser pulses. To achieve these results, we demonstrated a great amount of flexibility in exploring alternative fabrication and measurement approaches. We achieved a good match between experiment and theory with the addition of the phonon-imaging technique offered by our collaboration with Dr. David Hurley. Modeling work conducted early in the project showed that many of the common thermal property measurement techniques, such as thermal flash and steady-state electrical heating, are insufficiently sensitive for correlating the thermal resistance of a boundary with its atomic structure. The imaging technique we used was advantageous because it could resolve the angular dependence of transmitted and reflected phonons, which is an important component of testing the models.

Two of the key findings from the models developed in this project are that the Kapitza resistances of typical silicon grain boundaries are relatively small, and they do not appear to vary greatly as a function of grain boundary structure. This result was surprising as bulk structural disorder can greatly influence thermal conductivity in materials (isotopic impurities in diamond result in a 30% drop in thermal conductivity, and neutron irradiation, which introduces vacancies and extended defects, can easily reduce the thermal conductivity nearly tenfold). Furthermore, we have shown that structures with multiple (around ten) grain boundaries in series are still not

expected to generate large changes in thermal conductivity, which poses severe limitations on suitable experimental techniques.

Our preliminary work with Si-Si interfaces has given us valuable experience in developing the stringent processing requirements for creating interfaces with known atomic structures. In the case of Si-Si interfaces, we successfully achieved large-area intimate interfaces. This was achieved through (a) knowledge of the exact crystallographic orientation of the surface, the crystallographic directions in the plane of the surface, and surface chemistry; (b) developing a methodology for aligning two single-crystal surfaces to the required accuracy and creating temporary bonding; (c) defining the temperature, time-at-temperature for permanent bonding, as well as the atmosphere in the enclosure to assure the required stoichiometry at the interface; and (d) developing a controlled dicing and surface polishing methodology that produces cross sections with no steps or grooves at the bonded interface, thus enabling the picosecond measurement of phonon transport across these interfaces.

2.6 References

[1] S. S. Mahajan, G. Subbarayan, and B. G. Sammakia. –Estimating Kapitza resistance between Si-SiO_2 interface using molecular dynamics simulations," *2008 11th Intersociety Conference on Thermal and Thermomechanical Phenomena in Electronic Systems (ITHERM '08)*, pages 1055–62 (2008).

[2] D. Wolf and S. Yip. eds., *Materials Interfaces: Atomic-Level Structure and Properties*, Chapman and Hall, London, 1992.

3 Phonon Transport Along Interfaces

Section 3 describes our investigation of phonon transport along interfaces. The interaction of phonons with surfaces and interfaces is of particular interest in 1-D and 2-D systems, such as nanowires and phonon waveguides. We wanted to explore phonon scattering from boundaries, specifically thermal phonon scattering from a surface, as depicted in Figure 3-1. Free surfaces are inherently different from internal interfaces, e.g., grain boundaries. The acoustic mismatch at free surfaces is extreme, and they often have a high defect density. For small systems dominated by surfaces, the phonon-surface scattering can play a dominant role in phonon transport.

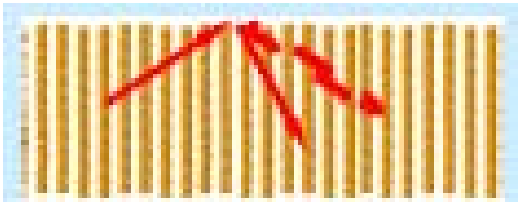

Figure 3-1. Phonon scattering from a surface. We may consider two scattering outcomes: specular scattering (dashed) or diffuse scattering (solid).

The objective of our study was to develop and demonstrate a structure for identifying the nature of thermal phonon scattering from the surface of monocrystalline silicon. The structure was designed so that measurements, combined with modeling, will enable quantification of the fraction of phonon-scattering processes that results in specular rather than diffuse reflections. Section 3.1 introduces concepts relevant to the topic of phonon scattering. In Section 3.2, we discuss how we designed, fabricated and modeled the new structure. We present our conclusions in Section 3.3, followed by a listing in Section 3.4 of the references cited in this work

3.1 Introduction

Reducing the dimensions of a material to the nanoscale may dramatically increase the thermoelectric performance [1, 2]. This increased thermoelectric performance is a result of decreased thermal conductance at small sample dimensions, viz. for sample sizes less than or comparable to the phonon mean free path. Unfortunately, our ability to predict the thermal conductance of nanoscale structures is rather limited. In nanoscale crystalline materials, such as nanowires and thin membranes, the surface scattering of phonons controls thermal conductance even at elevated temperatures where the phonon mean free paths and phonon wavelengths are small [3, 4, 5, 6].

One would presume that phonon scattering from a surface should be well-described by modeling the scattering of waves from an interface with variable roughness, and indeed this is the basis for some of the earliest models of phonon-surface scattering, leading to the well-known relation that specular reflection of a phonon from a surface is expected with a probability $\approx \exp(-8\pi^2\eta^2/\lambda^2)$, where η is a measure of the amplitude of surface roughness and λ is the phonon wavelength [7].

For surfaces that are smooth, this model predicts a predominance of specular surface scattering for the low-energy phonons that dominate at low temperatures and a predominance of diffuse scattering for the short-wavelength phonons that dominate thermal transport at higher temperatures. Indeed, at low temperatures (< 1 K), specular phonon scattering was found for atomically smooth silicon surfaces on macroscopic samples [8]. However, subsequent low-temperature experiments using smooth GaAs thin membranes revealed a sizable proportion of diffuse phonon scattering (up to 60% diffuse) [9]. At higher temperatures where T approaches Θ_D, the Debye temperature, diffuse surface scattering may be expected to dominate. To see this effect, it is necessary to use samples with critical dimensions less than the phonon mean free path, and this typically requires nanoscale (< ~ 100 nm) structures such as thin films and nanowires.

If diffuse surface scattering dominates at elevated temperatures, we would not expect to see a strong effect on phonon transport due to surface roughness; however, the opposite situation occurs. For example, Hochbaum et al. [1] observed a factor of 10 decrease in thermal conductance in silicon nanowires following chemical roughening of the surfaces. Furthermore, many measurements on thin films and nanowires show a strong size effect, even at length scales where phonon confinement is not expected to play a dominant role [3, 4, 5, 6] To model the size effect, it is common to invoke a ―surface roughness" fitting parameter [10, 11]. While this does provide agreement with experimental data, the surface scattering is required to range from near fully diffuse to near fully specular. This begs the question, how do we predict the thermal conductance of a nanoscale channel if we do not know the nature of surface phonon scattering? Given the strong dependence of conductance on surface scattering, estimates may easily be off by an order of magnitude.

Molecular dynamics simulations might offer some hope for understanding the nature of phonon scattering from interfaces; however, these simulations suggest that the surface scattering may be more exquisitely sensitive to surface structure than generally thought. For example, Markussen et al. found that surface vacancies can dramatically reduce the thermal conductivity of silicon nanowires [12]. Furthermore, Heino has reported that the thermal conductivity of silicon sheets depends dominantly on the crystallographic orientation of the surface, with sheets terminated by (110) surfaces showing much higher thermal conductivity (factor of 2) than sheets terminated with (100) or (112) surfaces [13]. This is despite the fact the surfaces are ―atomically flat" and highly perfect. These results highlight the clear need for detailed studies of the relationship between atomic structure and phonon-interface scattering.

3.2 Design, Fabrication, and Modeling

In this section, we describe the design, fabrication, and modeling of a silicon micromachined structure to measure phonon surface scattering in crystalline silicon. When a phonon scatters from a surface, we can consider the phonon to be diffusely or specularly scattered. For experiments to date, the measurement of surface scattering from thermal phonons has been an indirect process. Typically, one measures a thermal conductance that is then fit to a theory that allows for specular or diffuse surface scattering [8, 9, 10, 11]. The problem with this approach is that the models of the thermal conductance depend sensitively on the diffuse/specular scattering probability, yet high-precision experimental measurements of absolute thermal conductance in

nanoscale specimens are challenging. To overcome this problem, we created a differential thermal conductance structure to accentuate the effect of phonon scattering from surfaces.

3.2.1 Design

Our structure, shown in Figure 3-2, is formed from a silicon-on-insulator (SOI) wafer and consists of three suspended silicon platforms that are supported by long, narrow silicon beams. These beams provide thermal isolation from the frame. The structure is similar to the suspended silicon nitride membrane thermal conductance test structures developed by Shi et al. [6, 14], with the major difference being that we added another platform to enable differential thermal conductance measurements. The center platform is connected to its neighbors on each side by narrow silicon ligaments that are monolithic to the platform, thus eliminating any interfaces between the platforms and silicon ligaments. The ligaments have a bladelike cross section: each ligament has a width of 100 nm, a length of 1000 nm, and a thickness of 2000 nm. Hence we may refer to the ligaments as "nanochannels." The key aspect of the structure is that one ligament is straight while the other ligament is bent. Phonons with a mean free path exceeding 1000 nm may travel with few or no surface-scattering events in the straight ligament, whereas these phonons must undergo multiple surface-scattering processes in the bent ligament. The high-aspect-ratio cross section of the wires ensures that the dominant scattering processes are from the sides of the ligaments rather than from the top and bottom surfaces.

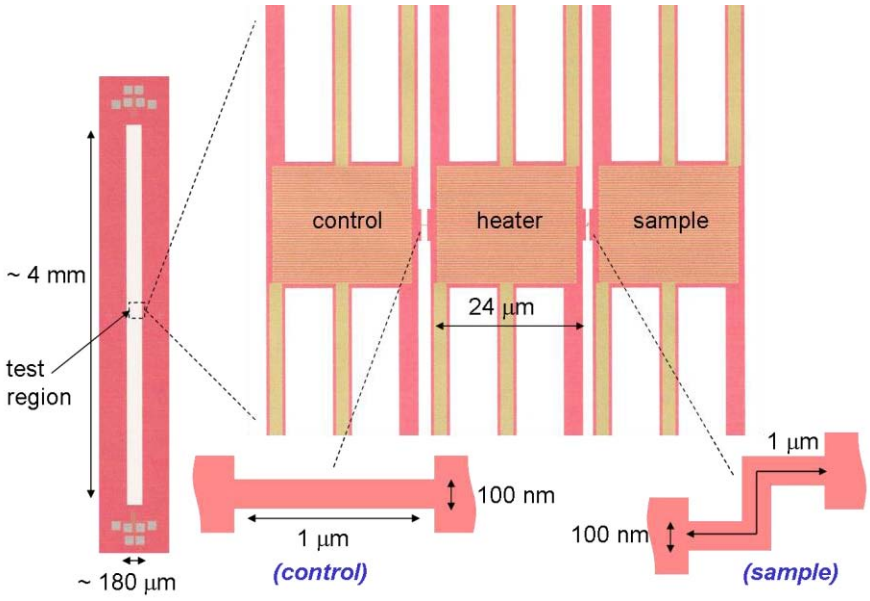

Figure 3-2. Design of the differential thermal transport platform consisting of three suspended platforms supported by > 2000 μm long silicon ligaments and bridged by straight and bent ligaments of 100 nm width, 1 μm length, and 2 μm depth.

By measuring the thermal conductance ratio of the straight and bent ligaments of otherwise identical description, effects common to both ligaments are cancelled and phonon-interface interactions are highlighted. The differential conductance is measured by supplying heat to the

center silicon platform and measuring the subsequent temperature rise in each of the two neighboring silicon platforms. The thermal conductance ratio is determined from measurements of the temperature ratios between the center heater and outer platforms. By varying the ambient temperature from ~ 77 K to room temperature, we change the phonon mean free path from greater than 1000 nm to less than 400 nm, enabling tuning of the effect of phonon boundary-scattering and changing the mean phonon wavelength.

Table 3-1 summarizes the physical dimensions of the structure and some selected electrical and thermal properties of the heater lines and connecting ligaments. Heating and thermometry is enabled by patterning thin metal lines down the supporting silicon ligaments and on top of the silicon platforms. Four electrical leads are provided to each heater and thermometer, enabling 4-point resistance measurements. The ratio of lead resistance to heater resistance of the center heater is approximately 0.4, ensuring that most heat generation occurs on the center platform with only small Joule heating of the leads.

Each platform is thermally isolated from the surrounding chip by six silicon ligaments of 2100 μm length, 3 μm width, and 2 μm thickness. The thin silicon ligaments connecting the platforms have nominal dimensions of 1 μm length, 100 nm width, and 2 μm thickness. The ratio of the thermal conductance of the thin ligaments to the six long supporting ligaments is greater than 10 if we assume the same thermal conductivity for all structures. This condition is chosen to ensure sufficient heating of the outer platforms (and a corresponding temperature rise) under steady-state heating conditions. Under actual experimental conditions, we expect the thermal conductivity of the thin ligaments to be reduced from the bulk value, leading to a lower ratio of thermal conductance and slightly less heating of the outer platforms.

Table 3-1. Dimensions of the Differential Thermal Transport Structure

	Platform			Supporting ligaments			Thin bridging ligaments		
	Length (μm)	Width (μm)	Depth (μm)	Length (μm)	Width (μm)	Depth (μm)	Length (μm)	Width (μm)	Depth (μm)
Silicon structural dimensions	24	24	2	2100	3	2	1	0.1	2
Thermal conductance ratio of bridging ligaments/supporting ligaments = 12									

	Leads		Heater/Thermo-meter	
	Length (μm)	Width (μm)	Length (μm)	Width (μm)
Metal lines	2300	2	1057	0.2
Lead resistance/heater resistance = 0.44				

For the measurement of differential thermal flux or thermal conductance, it is sufficient to measure a temperature ratio between one of the outer platforms and all other platforms as well as the frame. This temperature ratio is determined by measuring the resistance ratio of the thin metal lines that act as resistance thermometers, and this resistance ratio is conveniently measured using a bridge electrical circuit. Specifically, a resistance calibration is performed by measuring the resistance of the metal lines at discrete temperatures via temperature cycling in a cryostat. This generates calibration curves such as $R_{heater}(T)$ and $R_{straight}(T)$. When the temperature differences between the center heater and outer silicon platforms are small, the resistance ratios scale linearly with the temperature ratios of the platforms.

3.2.2 Fabrication

We fabricated the differential thermal transport structure from SOI wafers containing an undoped (> 1000 ohm·cm) silicon device layer, which was 2 μm thick, on top of a 2 μm thick buried oxide layer on an undoped handle wafer 500 μm thick. Numerous process flow sequences were attempted. We obtained the best results by using a process flow that consisted of the following:

1. Electron beam patterning to define the heater and resistor lines in the regions of the center and outer silicon platforms
2. Cr-Pt deposition (35 nm total thickness) and lift-off
3. Optical lithography patterning of the electrical leads connecting to the e-beam–patterned lines
4. Cr-Pt deposition and lift-off of the electrical leads (> 35 nm total thickness)
5. Optical lithography patterning of the platforms and supporting ligaments
6. Plasma etching (CF_4-based) through the silicon device layer and slightly into the oxide layer to define the silicon platforms and supporting ligaments
7. Focused-ion-beam (FIB) machining to define the thin nanoscale silicon ligaments
8. Wet etching (dilute HF) to remove the buried oxide layer and produce free-standing platforms

Figure 3-3 shows a scanning electron microscopy (SEM) image of the metal heater lines and electrical leads defined using electron beam and optical lithography. In earlier processing sequences, the metal lines were fabricated after silicon etching of the platform structures; however, we found that this approach leads to large topology and poor e-beam resist exposure near the edges of the elevated platforms. Fabricating the metal lines first eliminates topology issues during the e-beam writing steps.

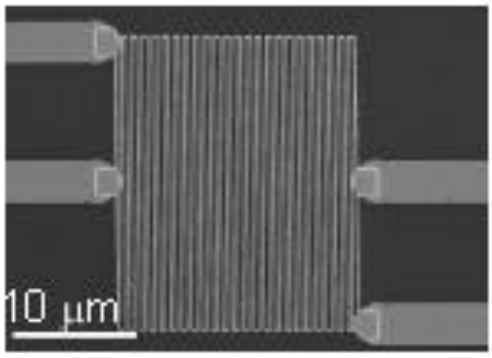

Figure 3-3. Patterned metal lines defining the heater/thermometer and the larger electrical leads.

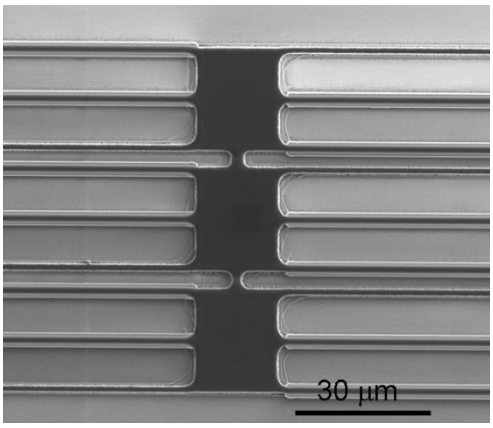

Figure 3-4. Structure following silicon etching to define the platforms and supporting ligaments.

Figure 3-4 above shows an SEM image of the silicon platform and supporting ligament structures following plasma etching through the silicon and removal of the etch mask. A CF_4-based reactive-ion-etch plasma is used to achieve a high silicon etch rate through 2 μm of silicon while using a photoresist-based etch mask (< 2 μm of AZ5214). A region of silicon is left between the center and outer platforms. In subsequent steps, this silicon was machined away using FIB to define the thin nanoscale ligaments.

In earlier processing sequences, we attempted to etch the silicon platforms simultaneously with the nanoscale ligaments. Two lithography steps were employed: (1) an optical lithography step followed by Al lift-off to define the platform and supporting ligaments and (2) an e-beam writing step followed by Al lift-off to define the nanoscale ligaments. These steps were followed by slow silicon etching using CF_4-based reactive-ion-etch plasmas or Bosch etching. In all cases, however, we observed undercutting beneath the Al etch mask, causing complete removal of the nanoscale ligaments (see Figure 3-5).

To create the nanoscale ligaments with the requisite 20:1 aspect ratio, we found that FIB machining produces the best results. Figure 3-6 shows SEM images of bent and straight ligaments following FIB machining. The machining process takes several minutes to tens of minutes per ligament. This process may limit the large-scale fabrication of structures, but it was sufficient for these studies. One advantage of the FIB machining step is reduced sidewall roughness compared to reactive ion etching processes (see Figure 3-7). A disadvantage of the FIB machining is possible ion damage at the sidewall surfaces of the ligaments as a result of ~ 10 keV gallium ion implantation. The

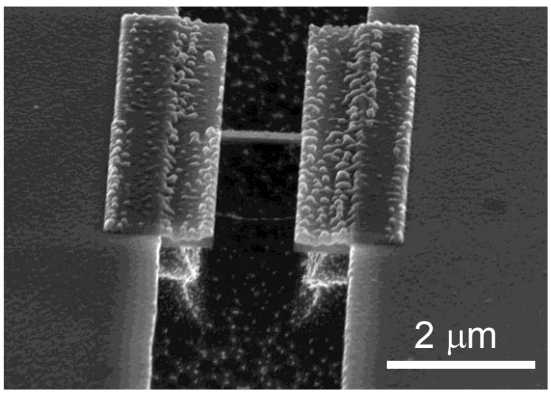

Figure 3-5. Reactive ion etching used to define the silicon platforms and nanoscale ligaments leads to undercutting and loss of the ligament (only the bridging aluminum etch mask remains in the image).

geometry of the sample (surfaces parallel to the ion beam) minimizes the implantation range. Furthermore, silicon thermal oxidation and wet etching following FIB machining could be used to remove the damaged surface layer.

Initial attempts at releasing the differential structure resulted in poor yield (fractured or missing supporting beams and platforms). These initial attempts used conventional dilute HF etching (1:5, HF:DI H_2O), followed by rinsing and drying under lightly flowing dry $N_{2(g)}$. We tried some preliminary release experiments based on the work of Mantiziba et al., using polystyrene microspheres to prevent stiction [15]. This approach seems promising, and future releases will be performed using this process.

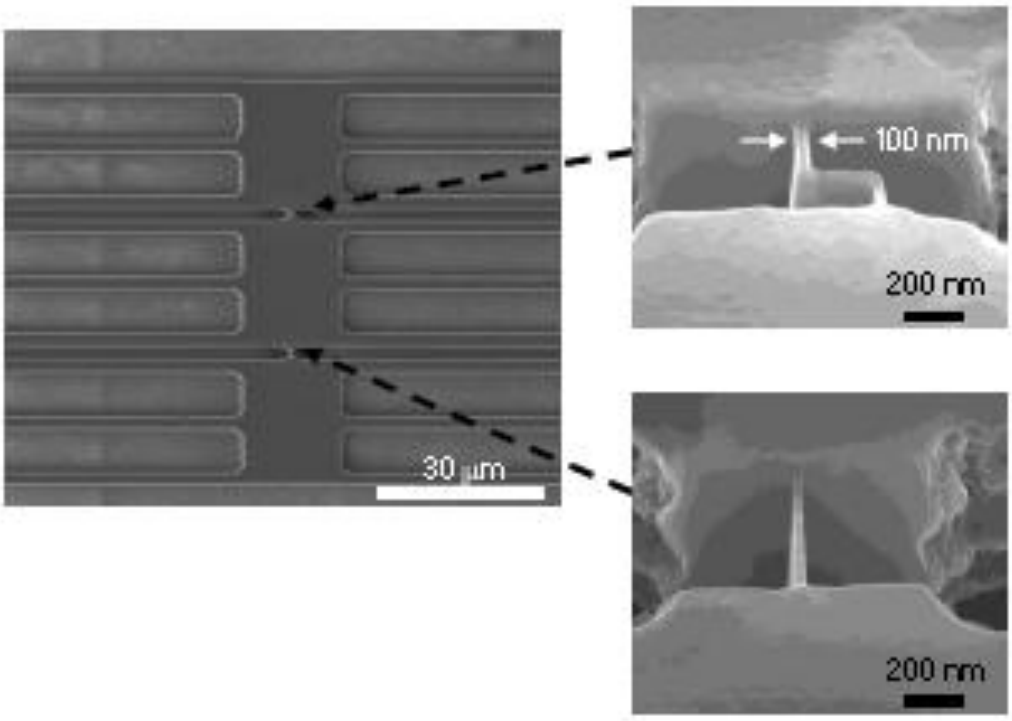

Figure 3-6. Differential structure following FIB machining to define the thin straight and bent ligaments.

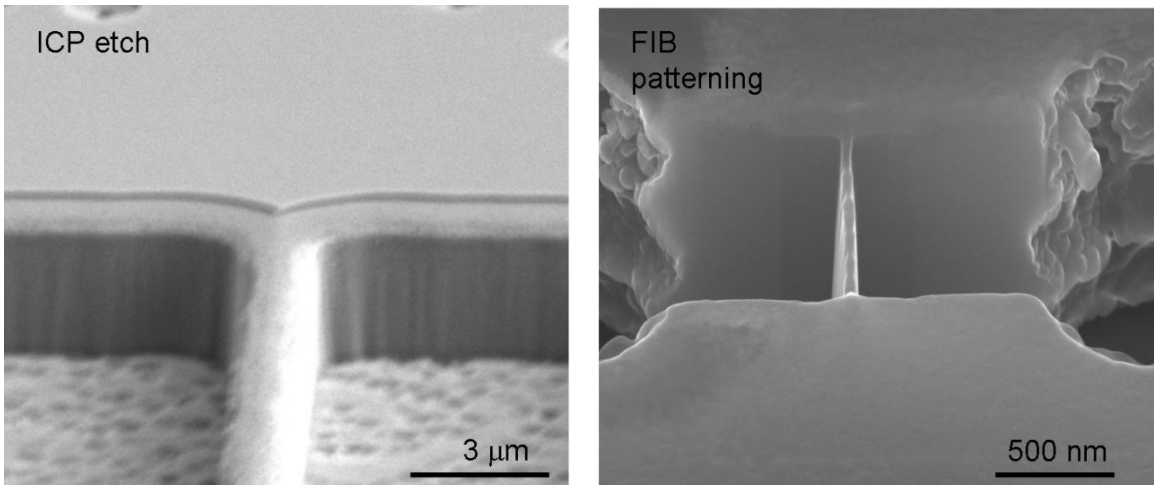

Figure 3-7. Comparison of sidewall roughness resulting from reactive-ion etching (ICP) and FIB patterning.

3.2.3 Modeling

For the differential structure, we are interested in the ratio of the heat flux flowing across the thin straight and bent ligaments. Using Fourier's law for 1-D heat transport, we may equate the steady-state flux through the straight and bent ligaments and into the platforms with the heat flux flowing out of the platforms:

$$(1)\quad \dot{Q}_{straight} = U_{ligaments}(T_{straight} - T_{ambient})$$

$$(2)\quad \dot{Q}_{bent} = U_{ligaments}(T_{bent} - T_{ambient})$$

where $\dot{Q}_{straight}$ is the heat flux flowing through the straight thin ligament, $U_{ligaments}$ is the lumped thermal conductance of the six silicon ligaments supporting the silicon platform, $T_{straight}$ is the temperature of the outer silicon platform connected to the straight ligament, and $T_{ambient}$ is the temperature at the silicon frame (the external reservoir). Assuming the ligaments supporting the outer platforms are identical ($U_{ligaments}$ is the same), then the ratio of heat flux between the bent and straight ligament is

$$(3)\quad \frac{\dot{Q}_{bent}}{\dot{Q}_{straight}} = \frac{(T_{bent} - T_{ambient})}{(T_{straight} - T_{ambient})} = 1 - \frac{(1 - T_{bent}/T_{straight})}{(1 - T_{ambient}/T_{straight})}$$

For direct comparison to thermal simulation, it is convenient to extract the ratio of the thermal conductances of the bent to the straight ligaments, $U_{bent}/U_{straight}$:

$$(4)\quad \frac{U_{bent}}{U_{straight}} = \frac{(T_{bent} - T_{ambient})(T_{heater} - T_{straight})}{(T_{straight} - T_{ambient})(T_{heater} - T_{bent})} = \frac{(T_{bent}/T_{straight} - T_{ambient}/T_{straight})(T_{heater}/T_{straight} - 1)}{(1 - T_{ambient}/T_{straight})(T_{heater}/T_{straight} - T_{bent}/T_{straight})}$$

where T_{heater} is the temperature of the center heater platform.

To deduce the proportion of specular and diffuse phonon scattering from silicon surfaces, we must compare the measured bent-to-straight ligament flux or conductance ratios to thermal transport simulations. The large size of the nanoscale silicon ligaments (0.2 μm^3 or ~ 1×10^{10} atoms) precludes direct molecular dynamics simulations, but it is well within the accessible range for Monte Carlo simulations. A thorough investigation of the conductance ratio between straight and bent ligaments has recently been reported by Piekos et al. [16], and that work is described in Appendix F of this report.

Monte Carlo simulations of phonon transport based on the Boltzmann transport equation were performed as a function of the specularity parameter of the sidewalls of the ligaments. For full specular scattering from the surface (specularity parameter = 1), tangential phonon momentum was preserved. For full diffuse scattering (specularity = 0), the tangential phonon momentum was randomized. For intermediate values of the specularity parameter, a probability of specular reflection following phonon-surface interaction was set equal to the specularity parameter.

The simulation results predict a ratio of thermal conductance between the bent and straight ligament of less than ~ 0.6 for 100% specular reflection (specularity parameter = 1) to greater than 0.8 for 100% diffuse reflection in the range of 200 K to 400 K (see Figure 3-8). This observation is consistent with our expectations—for predominantly specular reflection, many fewer phonon-surface scattering events occur for the straight ligament as compared to the bent ligament, leading to a large difference in thermal flux. For diffuse scattering, the mean scattering length of the phonons is similar between the two geometries, and hence the flux difference is smaller.

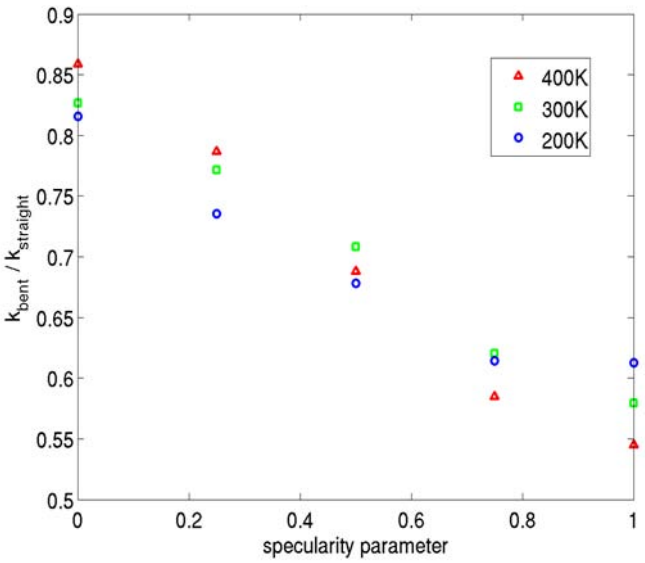

Figure 3-8. Ratio of the thermal conductivity of the bent and straight ligaments as determined from Monte Carlo phonon-transport simulations.

The experimental determination of the specularity parameter of the silicon surface is achieved by comparing the measured conductance ratio of the

ligaments to the curves of the conductance ratio deduced from Monte Carlo simulation. The Monte Carlo simulations suggest that the flux differences for these two geometries should be sufficient to give rise to a measurable differential heating of the outer silicon platforms and, hence, a detectable signal. To determine the expected temperature rise of the heater and outer platforms following application of electrical current to the central heater, we have performed full 3-D continuum electrothermal modeling.

The effective thermal conductivities for each ligament, at three temperatures and five specularity parameters, determined from Monte Carlo simulations, were used to provide a noncontinuum subgrid input to large-scale electrothermal simulations of the complete test structure and measurement procedure. Sandia's strength in massively parallel multiphysics simulation eliminates the need to depend on idealized analytic models to convert the electrical measurements to accommodation coefficients. Simulations were performed using SIERRA / CALORE [17] loosely coupled in four computational grids. The electrical problem in the metal heater/sensor on each of the three platforms, as well as its associated leads, was solved using temperature data from the thermal simulation. The thermal problem on a large (700K element) grid that contained all three platforms, both ligaments, and all metal heater / sensor lines and their respective leads was solved using Joule heating data from the electrical simulations. Solutions on all grids were iterated until a steady state was reached in both the electrical and thermal domains. A typical run on 64 Infiniband-connected nodes, each consisting of dual 3.6 GHz EM64T processors, on the Sandia Thunderbird cluster required approximately eight hours to complete. A temperature field for fully specular ligaments at 300 K is shown in Figure 3-9. In this simulation, a current of 0.1mA was applied to the heater and a 15 K temperature rise was observed in the center platform.

In addition to allowing the electrical data from the experiment to be converted to the desired specularity parameter with a minimum of simplifying assumptions, these simulations also allow the test behavior to be predicted before physical testing begins. For example, Figure 3-10 shows the observed resistance difference between the sensor platforms as a function of specularity parameter at two different temperatures using the same heater current. It may be seen that, because reducing temperature increases the thermal conductivity of the supporting legs, as well as the electrical conductivity of the heater, a fixed current produces a diminishing signal because the temperature increase of the heater platform is reduced.

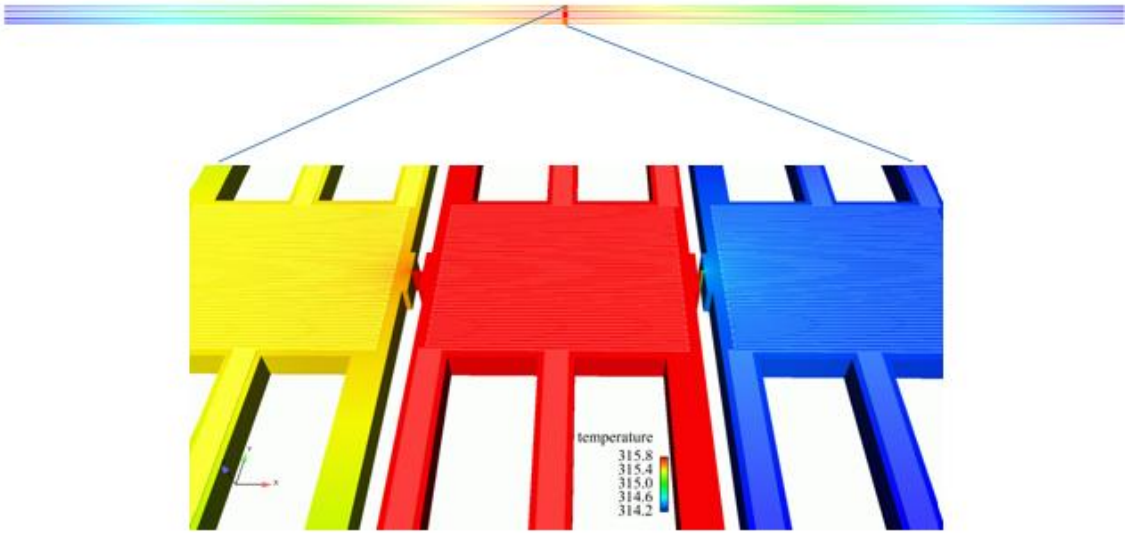

Figure 3-9. Temperature distribution of differential structure with 0.1 mA heater current at 300 K ambient temperature. The thermal conductivity of each ligament was derived from Monte Carlo simulations with fully specular reflection. The lower limit of the temperature scale was increased in the figure inset to highlight the temperature difference between platforms.

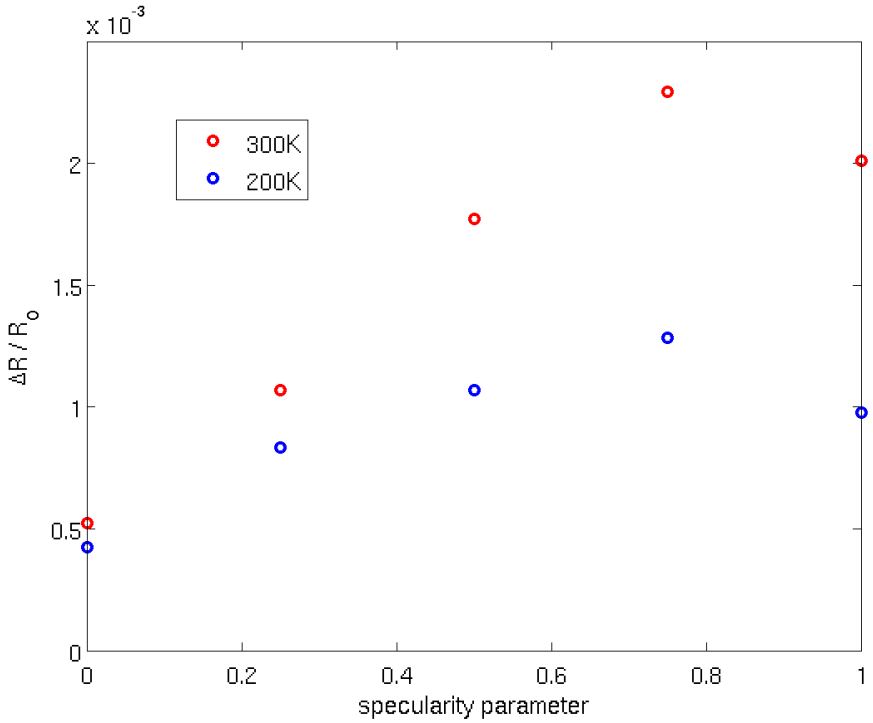

Figure 3-10. Predicted resistance difference between sensor platforms as a function of specularity parameter at two temperatures with 0.1 mA heater current. Sensitivity to specularity parameter decreases with decreasing temperature at fixed current because temperature rise of center platform is reduced due to increasing thermal conductivity in support legs and decreasing resistance in heater.

3.3 Conclusions

In this study, we developed a structure for measuring the degree of specular or diffuse phonon scattering from the surface of silicon. The structure uses three thermally isolated single-crystal platforms that are bridged by straight and meandering monocrystalline silicon ligaments of nanoscale cross section. Through measurement of the ratio of the thermal conductance of the silicon ligaments and comparison to Monte Carlo simulation of phonon transport, we may deduce the specularity parameter of the silicon surface. A fabrication process has been developed to achieve the structure, using a sequence of optical and electron-beam lithography and FIB machining on SOI substrates. Structures have been successfully fabricated up to the final step of oxide etching and thermal isolation—the last step before thermal measurement. We believe that this structure will be useful for understanding many phenomena associated with phonon transport along boundaries. As means for measuring accommodation are few for gases and nonexistent for phonons, we have filed two technical advances based on the concept.

In addition, a variant of the new differential structure is part of a chip-based research platform called the CINT Cantilever Array Discovery Platform™ 2.0. This is a second-generation platform that was released in September 2009. This structure and others are freely available to users of the Center for Integrated Nano-Technologies (CINT). CINT is a Department of Energy/Office of Science Nanoscale Science Research Center, which operates as a national user facility devoted to establishing the scientific principles that govern the design, performance, and integration of nanoscale materials. The facilities and capabilities of CINT are available to interested nanoscience researchers through a peer-reviewed user proposal process. For more information, see http://cint.lanl.gov/.

3.4 References

[1] A. I. Hochbaum, R. Chen, R. D. Delgado, W. Liang, E. C. Garnett, M. Najarian, A. Majumdar, and P. Yang. "Enhanced thermoelectric performance of rough silicon nanowires," *Nature* 451: 163 (2008).

[2] A. I. Boukai, Y. Bunimovich, J. Tahir-Kheli, J.-K. Yu, W. A. G. III, and J. R. Heath. "Silicon nanowires as efficient thermoelectric materials," *Nature* 451**:** 161 (2008).

[3] M. Ashegi, Y. K. Leung, S. S. Wong, and K. E. Goodson. "Phonon-boundary scattering in thin silicon layers," *Appl. Phys. Lett.* 71: 1798 (1997).

[4] W. Liu and M. Ashegi. "Phonon-boundary scattering in ultrathin single-crystal silicon layers," *Appl. Phys. Lett.* 84: 3819 (2004).

[5] D. G. Cahill, W. K. Ford, K. E. Goodson, G. D. Mahan, A. Majumdar, H. J. Maris, R. Merlin, and S. R. Philpot, "Nanoscale thermal transport," *J. Appl. Phys*. 93: 793 (2003).

[6] D. Li, Y. Wu, P. Kim, L. Shi, P. Yang, and A. Majumdar. "Thermal conductivity of individual silicon nanowires," *Appl. Phys. Lett.* 83: 2934 (2003).

[7] R. Berman, E. L. Foster, and J. M. Ziman. "Thermal conduction in artificial sapphire crystals at low temperatures: I. Nearly perfect crystals," *Proc. Royal Society London A* 231: 130 (1955).

[8] T. Klitsner, J. E. VanCleve, H. E. Fischer, and R. O. Pohl. "Phonon radiative heat transfer and surface scattering," *Phys. Rev. B* 38: 7576 (1988).

[9] T. S. Tighe, J. M. Worlock, and M. L. Roukes. "Direct thermal conductance measurements on suspended monocrystalline nanostructure," *Appl. Phys. Lett.* 70: 2687 (1997); W. Fon, K. C. Schwab, J. M. Worlock, and M. L. Roukes. "Phonon scattering mechanisms in suspended nanostructures from 4 to 40 K," *Phys. Rev. B* 66: 045302 (2002).

[10] B. Yang and G. Chen. "Partially coherent phonon heat conduction in superlattices," *Phys. Rev. B* 67: 195311 (2003).

[11] L. H. Liang and B. Li. "Size-dependent thermal conductivity of nanoscale semiconducting systems." *Phys. Rev. B* 73: 153303 (2006).

[12] T. Markussen, A.-P. Jauho, and M. Brandbyge. "Electron and phonon transport in silicon nanowires: Atomistic approach to thermoelectric properties," *Phys. Rev. B.* 79: 035415 (2009).

[13] P. Heino. "Simulations of nanoscale thermal conduction," *Microsyst. Technol.* 15: 75 (2009).

[14] L. Shi, D. Li, C. Yu, W. Jang, D. Kim, Z. Yao, P. Kim, and A. Majumdar. "Measuring thermal and thermoelectric properties of one-dimensional nanostructures using a microfabricated device," *J. Heat Trans.* 125: 881 (2003).

[15] F. Mantiziba, I. Gory, G. Skidmore, and B. Gnade. "Wet-etch release process for silicon-micromachined structures using polystyrene microspheres for improved yield," *J. MEMS* 14: 598 (2005).

[16] E. S. Piekos, J. P. Sullivan, T. A. Friedmann, and S. L. Shinde. "Monte Carlo simulation of structures for assessing phonon-surface interaction," manuscript in preparation.

[17] Calore, 2008: Calore Development Team, "Calore: A Computational Heat Transfer Program, Volume 2: User Reference Manual, Version 4.6," Sandia report SAND2008-0098P, Sandia National Laboratories, Albuquerque, NM, 2008.

4 Development and Patterning of Epitaxial Diamond Thin Films

To study phonon transport in patterned structures, we grew diamond films by chemical vapor deposition (CVD) on iridium and fabricated diamond microelectromechanical systems (MEMS). Section 4.1 explains why we selected diamond and the challenges it poses for MEMS. Section 4.2 describes the processing steps that were taken to grow diamond and fabricate MEMS. The results of the various processing steps are given in Section 4.3. In Section 4.4, we discuss how our diamond-growth process and results compared to those of other researchers. Section 4.5 gives our conclusions, with the cited references listed in Section 4.6.

4.1 Introduction

Diamond has interesting properties for MEMS [1]. It has high hardness (~ 100 GPa), a low friction coefficient (< 0.1), and low adhesion. Single-crystal diamond also has interesting electronic properties including high electron mobility and high band gap that are potentially suitable for high-temperature electronics. In addition, single-crystal diamond should have lower defect density that would imply lower thermal-mechanical dissipation losses in mechanical resonators [2, 3]. Many forms of diamond have been made into MEMS including microcrystalline diamond [4, 5, 6], nanocrystalline diamond [7], and tetrahedrally amorphous carbon [1].

To date, MEMS have not been built on single-crystal diamond for several reasons. First, there is no reliable means of growing large-area thin films with the requisite quality. Second, single-crystal material must have low intrinsic stress and a low-stress gradient to prevent in- and out-of-plane deformation in free-standing structures. Third, since diamond tends to nucleate sparsely on heteroepitaxial substrates, it is difficult to produce thin layers (~ 1 μm) with low defect concentrations.

To use single-crystalline diamond for MEMS applications, a researcher needs to develop a technology to grow large areas. Recent advances in diamond growth technology make this possibility more realistic, specifically the development of reasonably large-area diamond nucleated on iridium substrates [8]. Ohtsuka et al. [8, 9] were the first to discover that highly oriented diamond films could be grown on Ir(100) surfaces using bias-enhanced nucleation (BEN). Several other groups have reported enhanced nucleation of diamond on various iridium-coated substrate combinations including MgO, [9, 10, 11, 12] $SrTiO_3$ [13, 14], a-plane sapphire [15, 16], CaF_2 [17], and yttria-stabilized zirconia (YSZ) [18, 19] on Si(100). From a MEMS perspective, the last development listed is perhaps the most exciting because it offers the possibility of growing large areas of diamond single-crystal material. In addition, low-stress material is possible as silicon and diamond have reasonably close thermal-expansion coefficients. Also, reasonably high nucleation densities have been demonstrated, resulting in high-quality thin layers.

4.2 Experiment

In this section, we describe our attempts to grow diamond on oriented Ir(100)/YSZ(100)/Si (100) substrates. The process described below consists of the following steps: (1) growth of the YSZ layer on Si(100) using pulsed laser deposition (PLD), (2) sputter deposition of the Ir(100) buffer layer to produce highly oriented Ir(100) surfaces, (3) growth of oriented diamond films on the Ir(100) surface by conventional CVD, (4) characterization, and (5) fabrication of the diamond into simple single-level MEMS devices using conventional processing technologies.

4.2.1 Pulsed Laser Deposition of YSZ Thin Films

We used PLD to deposit the YSZ films onto heated 4-inch Si(100) surfaces (cleaned in buffered hydrofluoric acid) in a vacuum chamber (base pressure 4×10^{-9} Torr) using an excimer laser (248 nm) with a focused energy density of ~ 2 J/cm^2. The laser beam impinged on the cylindrical axis of a 1-inch-diameter $(Y_2O_3)_{.10}(ZrO_2)_{0.90}$ hot-pressed target that was rotated and translated to prevent cratering of the target surface. Before deposition, the target was conditioned to remove surface contaminants and particles. We used a two-step process (similar to Wang et al. [20]) to increase the crystalline quality of the deposited films. The initial deposition was performed for 15 seconds with a 10 Hz laser repetition rate at 800°C under nominal base-vacuum conditions (~ 1.0×10^{-7} Torr while the laser was firing). Under these conditions, the affinity of oxygen for yttrium is greater than for silicon so that the initial YSZ layer can form epitaxially on the silicon surface. We then introduced O_2 gas at a 5 sccm flow rate with 1.5 mTorr into the chamber and continued the deposition at 10 Hz for 30 minutes, resulting in a ~ 300 Å thick film. Finally, we measured the temperature with a type-K thermocouple buried in the heater assembly. Tests with a second thermocouple on the substrate surface indicated there was ~ 100°C lower temperature on the sample surface. This offset was subtracted from the temperature data presented here.

4.2.2 Sputter Deposition of Iridium

The same vacuum chamber used to deposit the YSZ layer was also employed to deposit the iridium overlayer. Without breaking vacuum, the sample was cooled to ~ 670°C over a 30-minute time span while maintaining the oxygen background pressure and flow. Once temperature stability was achieved, the O_2 flow was discontinued and Ar gas at a 4 sccm flow rate and 2 mTorr pressure was introduced into the chamber. We used a 3-inch iridium sputter target on a US Gun MAK II source mounted 15 cm from the substrate surface. The RF power was 300 W and the iridium deposition was 30 minutes in duration. The resultant film thickness was ~ 2000 Å as measured with a stylus profilometer yielding a deposition rate of ~ 1.0 Å per second.

4.2.3 Diamond Deposition by Microwave Plasma CVD

The CVD diamond was grown in a modified ASTEX 1.5 kW reactor. To concentrate the plasma, we mounted the sample on a graphite puck (3 cm diameter × 0.5 cm height) on the sample stage; we also mounted a water-cooled stainless steel bias ring (7.5 cm diameter) 3 cm above the sample surface. The setup was similar to that described by Shreck et al. [13]. The ring was biased positive with respect to the grounded sample stage. To measure the sample

temperature, we used both a type-K thermocouple (sheathed and electrically insulated) pressed to the backside of the sample and an optical pyrometer. The emissivity of an iridium surface near 700°C was set at 0.19, and remarkably the two instruments agreed to within ~ 10°C. A typical run would commence by heating the sample to near 630°C in vacuum. Next, the sample surface was cleaned for 10 minutes using a hydrogen microwave plasma (300 sccm, 18 Torr, and 900 W). Then methane gas (6 sccm flow, 2% CH_4/H_2) was introduced into the chamber waiting three minutes for the gas concentration to equilibrate before application of the DC bias (200–350 V) for one hour. After the bias was switched off, a 0.5-hour nucleation step was used under conditions designed to produce pyramidal grains with (111) facets. Then, over a half-hour period the methane flow rate, pressure, and temperature were linearly changed to final values of 3 sccm, 28 mTorr, and 700°C, respectively, and held constant for the final growth step (3–48 hours). These conditions were designed to promote the growth of (100)-faceted diamond. The entire diamond-growth process was controlled using a computer running a custom Labview™ software package.

To measure stresses during growth, we fitted the diamond reactor with a laser-based (670 nm) wafer-curvature measurement system (k-Space Associates MOSS). The system can resolve changes in a radius of curvature > 5 km under optimal conditions. This capability corresponds to a film stress resolution of ± 10 MPa for the 0.5 mm thick silicon substrates used in this experiment. We took data points at an ~ 1 sample/second interval by averaging 10 separate consecutive measurements.

4.2.4 Characterization

To record the Raman spectra, we used a 514.5 nm Ar-Ion laser line fiber coupled to a Kaiser Optics Mark II holoprobe head with an 80x microscope objective at 10 mW power. The light was dispersed in an Acton SpectraPro-500i 0.5 m spectrometer using a 1200-groove/mm grating onto a 1024 × 1024 CCD chip (Princeton Instruments) with a 25 μm pixel size, giving a 1.2 cm^{-1} spectral resolution.

We used a JEOL JSM-IC845A scanning electron microscope (SEM) for surface imaging and a Philips X'Pert-MPD diffractometer with an unfiltered copper X-ray source for structure analysis.

4.2.5 MEMS-Based Processing

We used conventional lift-off–based lithography techniques to pattern and etch the diamond films. The films were patterned with a titanium hard mask using a contact aligner to expose resist (AZ 5214) followed by e-beam deposition of 1500 Å of titanium and lift-off in acetone. The diamond was etched in an RF plasma (300 W, –400 V DC bias) parallel-plate tool (Plasmatherm 720) using an O_2/CF_4 chemistry of 30/1 sccm flow rate and 30 mTorr pressure. We added the CF_4 to prevent micromasking effects, which are presumably due to deposition of metal contaminants onto the unmasked areas. Typical etch rates under these conditions were ~ 2 μm per hour.

4.3 Results

4.3.1 PLD Deposition of YSZ Buffer Layer

Figure 4-1 shows the θ/2θ diffractogram of the Ir/YSZ layers grown on silicon. The YSZ layer has a (100) orientation with the underlying silicon substrate. The oxygen pressure during the second YSZ growth step is the main factor controlling the orientation of the YSZ layer, with higher pressures consistently yielding mixed (111)/(100) orientations. The overlaying iridium layer is also (100) oriented, indicating that the original crystallographic information from the silicon substrate was preserved. There is a small (111) component to the iridium layer as can be seen in Figure 4-1 by the presence of the (111) (2θ = 40.7°) and (222) (2θ = 88.04°) peaks. The (111) peak is more than four orders of magnitude less intense than the (100) peak.

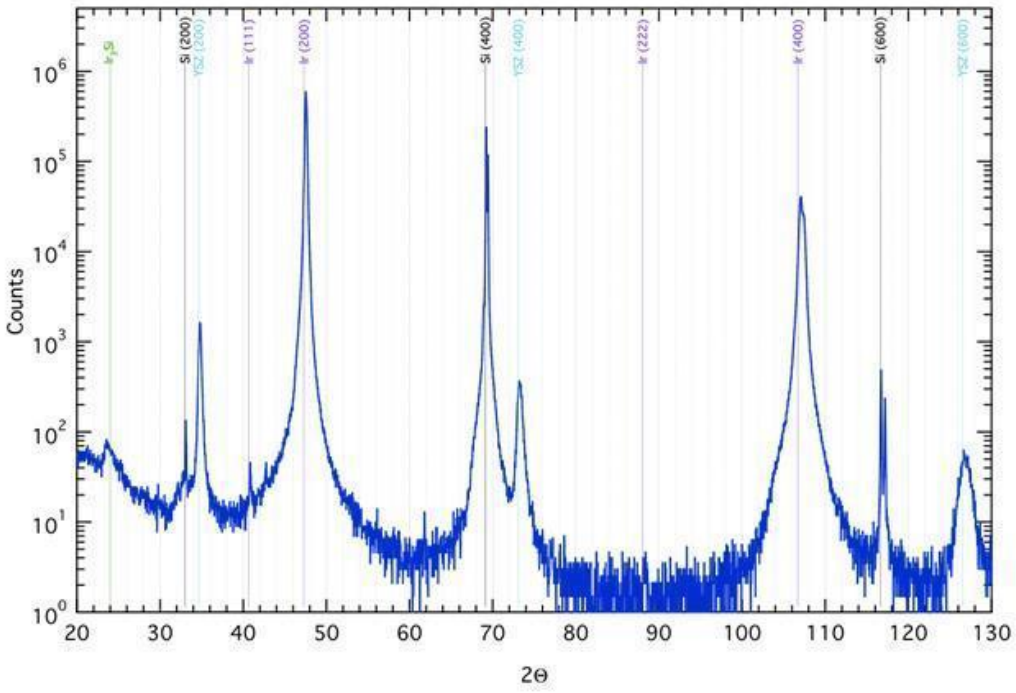

Figure 4-1. X-ray diffraction θ/2θ scan of an Ir/YSZ layer on silicon.

The broad feature centered near 24° in Figure 4-1 appears only after the deposition of the iridium layer, and we believe it is associated with the formation of an iridium silicide. As discussed below, we often see the formation of Ir_3Si after diamond deposition. The feature at 24° resolves into sharp (002) and (110) peaks indexed to the tetragonal Ir_3Si [21].

The intensity ratio of the Ir (111) to (100) peaks as a function of deposition temperature is shown in Figure 4-2. There is a fairly broad minimum near 650°C where the deposited iridium film is (100) oriented. At lower temperatures, the film orientation changes to a (111) orientation. These results are similar to those obtained by Gsell et al. [18] and Dai et al. [22] regarding orientation of the iridium films.

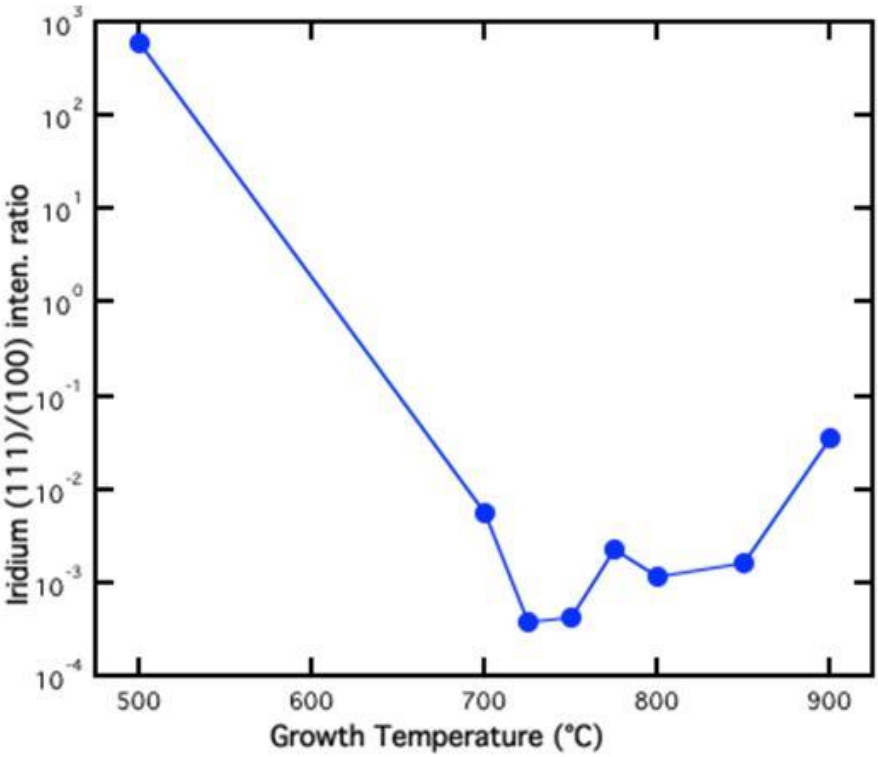

Figure 4-2. Ratio of the x-ray peak height of the Ir(111) to the Ir(100) as a function of substrate temperature.

4.3.2 Diamond Deposition Results

Figure 4-3 depicts a $\theta/2\theta$ diffractogram of a typical ~ 3 μm thick diamond film grown for 16 hours on an iridium layer using the BEN process. For this particular film, the bias was 350 V during the nucleation step. In our reactor, we typically found that voltages below 300 V did not produce nucleation of diamond as the subsequent growth step yielded no diamond. In contrast, voltages above 300 V yielded immediate diamond growth upon cessation of the bias as determined by oscillations in the intensity of the reflected laser light from the in situ stress monitor. Rocking-curve analysis of the diamond (400) peak revealed that the full-width at half maximum (FWHM) is 2.2°. The (400) rocking-curve peak (not shown) is also split into two peaks 3.5° from 0°, indicating that the textured growth process was not optimized for pure (100) growth [23]. Also present in Figure 4-3 are a number of new lines that index to Ir_3Si. This phase crystallizes sometime during the diamond growth process, indicating a breakdown of the YSZ buffer layer. It is possible that the silicon and iridium make contact either through pinholes in the YSZ or through microcracks brought on by thermal stresses, but we note that Gsell et al. [18] do not report silicide formation for their e-beam evaporated iridium process. Perhaps the more energetic sputter deposition technique causes some intermixing of the iridium into the YSZ layer, as the broad silicide peak is evident in Figure 4-1 after the iridium deposition prior to diamond growth. Interestingly, the silicide appears to show two distinct orientations, both (110) and (001), with respect to the Si(100) substrate. In spite of these problems, the original iridium layer appears to be intact, suggesting that the silicide formation is limited and not catastrophic for the subsequent diamond nucleation and growth.

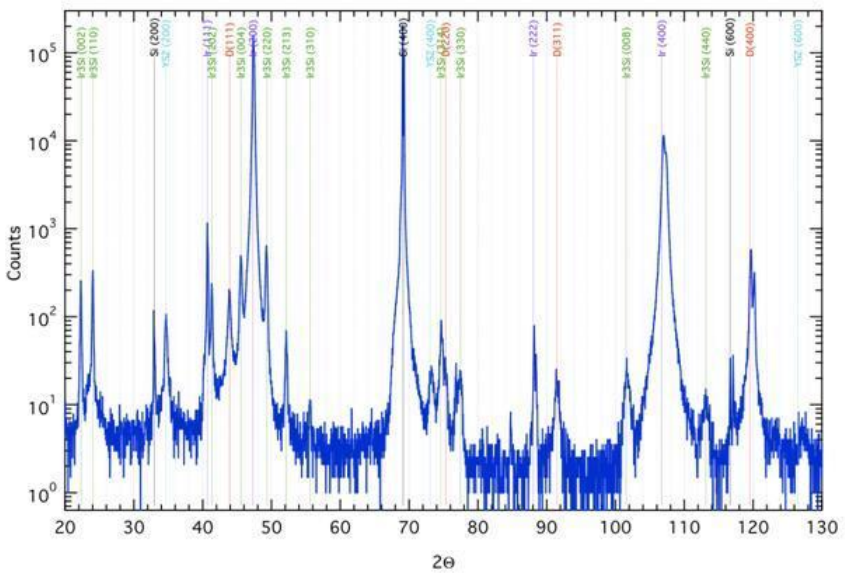

Figure 4-3. X-ray diffraction θ/2θ scan of a diamond/Ir/YSZ stack on silicon. Note the Ir_3Si peaks.

Figure 4-4 is a SEM micrograph of the diamond surface that reveals oriented (100) diamond facets. Figure 4-5 shows the Raman spectra from this film, revealing a sharp (5.1 degree FWHM) diamond Raman peak at 1333.2°. The shift from the single-crystal peak suggests an intrinsic tensile stress of ~ 0.8 GPa [24]. The Raman spectra also show some background fluorescence and the presence of limited nondiamond carbon.

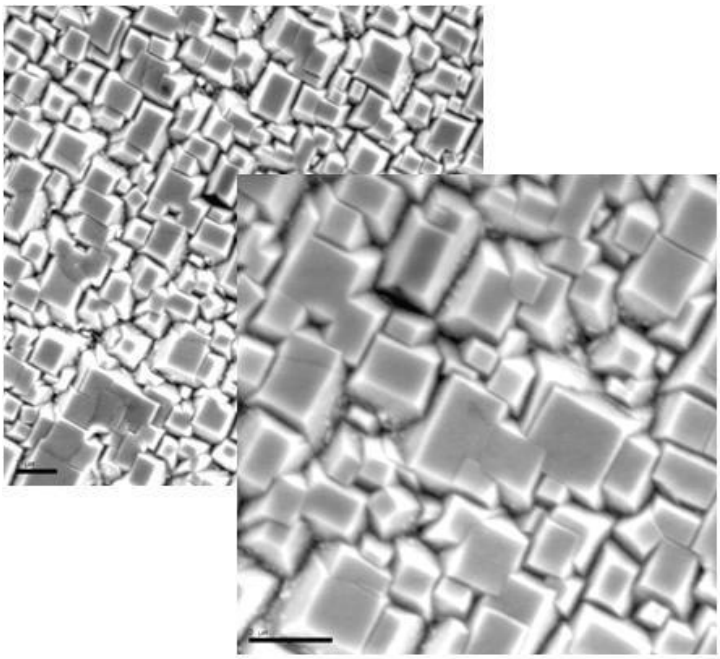

Figure 4-4. SEM micrograph showing an aligned diamond sample with (100) growth surfaces.

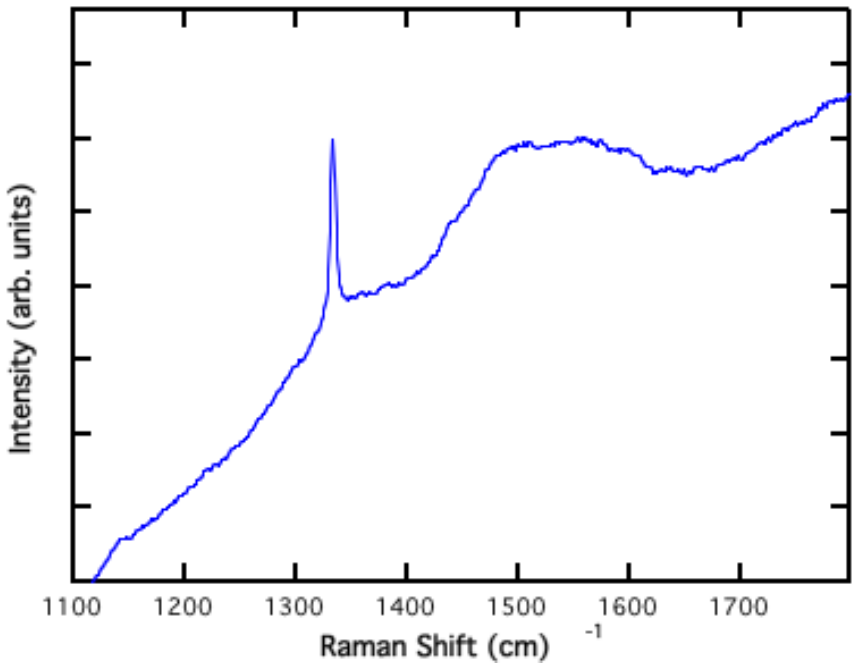

Figure 4-5. Raman intensity versus wave number for an aligned diamond sample.

Figure 4-6 depicts the stress-thickness profile versus time for a different diamond film than the one discussed above but grown under similar conditions. The compressive thermal stress of the Ir/YSZ layer builds as the temperature is ramped up to the growth temperature. There is a further compressive excursion when the plasma is initiated and the reactor comes to steady-state temperature conditions. Application of the bias causes another temperature excursion, eventually leading to constant stress thickness with time, followed by cessation of the bias and nucleation of the diamond film, and then steady-state conditions for diamond growth. The slope of the stress-thickness curve is proportional to the tensile stress in the growing diamond film of 110 MPa. Upon cessation of the growth, the sample cools to room temperature introducing thermal mismatch stresses between the various layers. The thermal stresses act to reduce the total stress upon cooling, leading to a lower-stress diamond film. We found that the diamond is adherent to the iridium layer, showing no signs of delamination. Due to the thermal excursion caused by heat generated by the application of the DC bias, we could not identify a systematic change in the stress due to the thin carbon-rich nucleation layer. As the sensitivity of the measurement increases with the square of the thickness of the silicon substrate, further experiments with thinned silicon may reveal a stress associated with the nucleation layer. During the BEN step there was no change in the stress-thickness profile, indicating that neither was diamond growing on the surface nor was the iridium layer being sputtered away.

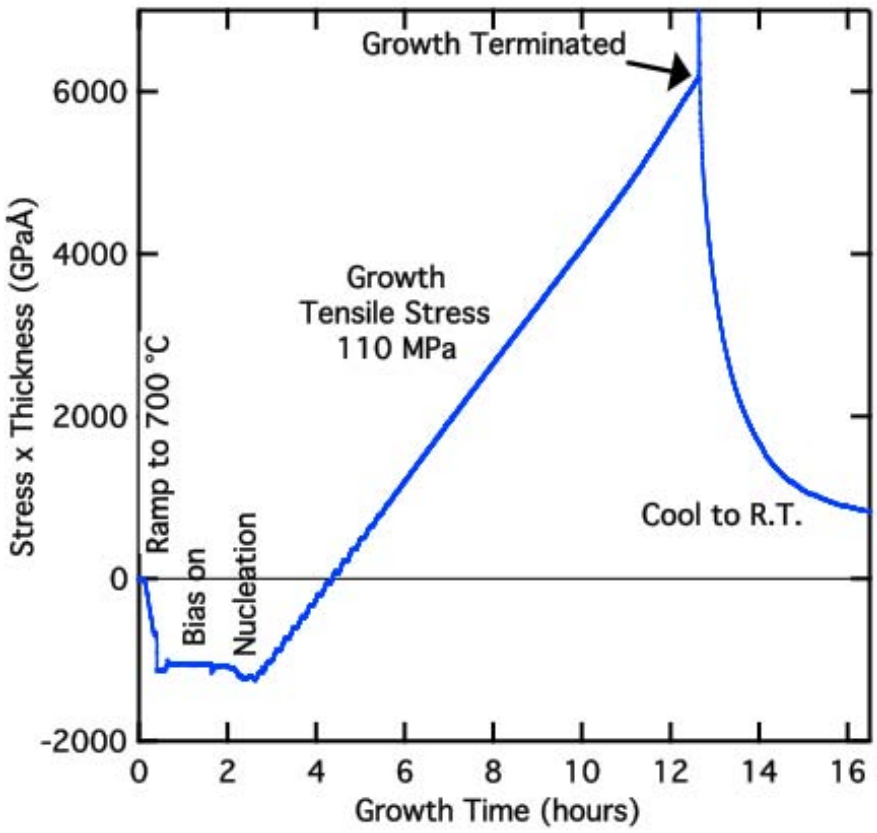

Figure 4-6. Stress thickness versus growth time for a diamond sample showing the entire growth cycle.

4.3.3 MEMS Devices

Figure 4-7 is a SEM micrograph of released diamond MEMS devices. The picture shows both single- and double-clamped cantilever beams. The double-clamped beams are not buckled, which indicates that the film has either zero or low tensile stress in agreement with the in situ stress measurements. The single-clamped beams are remarkably straight, with the radius of curvature > 1 m. This flatness is consistent with the linear stress-thickness profile observed during diamond growth. We note that the YSZ iridium layer is still attached to the underside of the released structures, so the resultant curvature is due to the sum of the three materials. A definitive statement regarding the actual magnitude of the diamond out-of-plane stress gradient would require etching away the buffer layers, but the high degree of flatness suggests that these gradients are low.

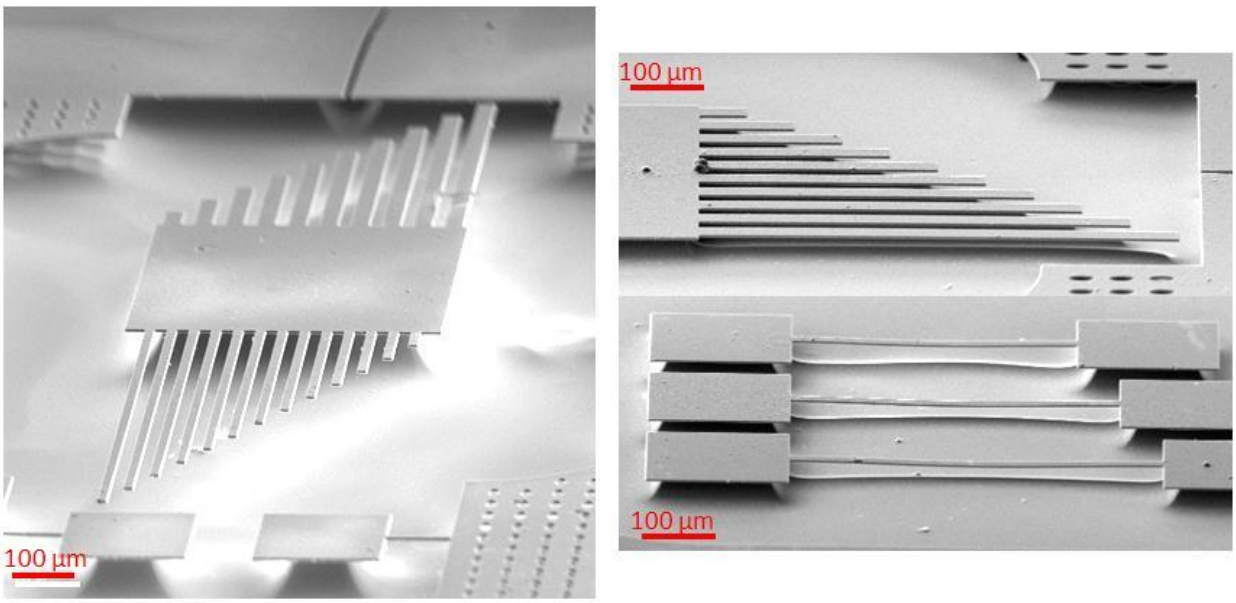

Figure 4-7. SEM micrographs of the released diamond single-layer MEMS structures.

4.4 Discussion

4.4.1 Optimization of the YSZ and Iridium Layers

One of the main differences of our work compared to that of Gsell at al. [18] is the use of sputtering to deposit the iridium layer. This choice appears to produce YSZ buffer layers that are less effective at eliminating silicide formation. Incipient silicide formation is present after the iridium growth step, but crystalline Ir_3Si does not appear until after the slightly higher-temperature (~ 700°C) but longer-time diamond growth. Of crucial concern is how this silicide layer affects the diamond nucleation. For example, if the silicide layer is separated from the top iridium layer by a largely intact YSZ layer (as suggested by the X-ray diffraction [XRD] results), this may be of little importance to the diamond growth. Further cross section transmission electron microscopy (TEM) work is necessary to reveal the mechanism of silicide formation and definitively answer this question.

The diamond layers grown in this study were not as highly oriented as those grown by others [14, 16], indicating that we were not able to effectively control either or both of the nucleation and subsequent textured diamond-growth steps. We found that bias voltages above 300 V were necessary to nucleate diamond and that diamond did not grow at lower voltages, revealing the importance of the bias procedure. To understand the subtleties of the diamond growth process, further separate studies of the nucleation and textured growth steps must be performed. Recent work [25] on DC plasma biasing seems to produce more-uniform nucleation results and is a promising direction for future work. We note that our typical diamond films were much thinner than the optimum results published by Schreck et al. [14] and that controlled textured growth improves the quality of the diamond layer with growth thickness. As we were mainly interested in thinner diamond for the MEMS work, this necessarily means our films will be of initially poorer quality, placing greater constraints on the initial nucleation process.

The in situ stress results provide a highly useful tool for both fundamental understanding and process control of the diamond growth. Under the growth conditions used in this study, tensile diamond films were produced with a linear stress-thickness (constant stress) profile. Many possibilities exist, such as dopants, temperature, and methane concentration, for changing the intrinsic stress of the diamond, opening the door to engineered stress profiles.

One promising result of this study is the ease of fabricating released structures that are quite flat. For polysilicon MEMS, tight process control is needed to produce flat structures, and strain gradients must be engineered by fairly complex doping, annealing, and/or growth temperature control. One disadvantage of our process is that the Ir/YSZ buffer layer underlies the released structures. Iridium can be plasma etched in a dry process, but whether this is possible on the underside of released structures has not been demonstrated and may require a backside etch of the silicon substrate. On the other hand, it is possible to pattern the exposed iridium layer either before the diamond is grown (selective growth) or once the diamond has been etched from above, so that the iridium layer can be used as an electrical contact to specific devices.

4.5 Conclusion

Using bias-enhanced nucleation, we grew diamond thin films on oriented Ir(100)/YSZ(100)/Si(100) substrates that when processed into released MEMS devices were flat (> 1 m radius of curvature). The sputter-deposited iridium layer tended to produce crystalline Ir_3Si with two preferred orientations ((110) and (100)) upon subsequent diamond growth. The YSZ buffer layer did not provide a perfect barrier against formation of iridium silicides; however, these silicides did not seem to materially affect the diamond growth nor the flatness of MEMS.

4.6 References

[1] J. P. Sullivan, T. A. Friedmann, and K. Hjort. "Diamond and amorphous carbon MEMS," *MRS Bull*. 26: 309–311 (2001).

[2] N. Sepulveda, J. Lu, D. M. Aslam, and J. P. Sullivan, "High-performance polycrystalline diamond micro- and nanoresonators," *J. Micro. Sys*. 17(2): 473 (2008).

[3] C. E. Nebel. "Electronic properties of CVD diamond," *Semi. Sci. Tech*. 18 (3)**:** S1–S11 (2003).

[4] E. Kohn, P. Gluche, and M. Adamschik. "Diamond MEMS–A new emerging technology," *Diamond and Related Materials* 8: 934–940 (1999).

[5] T. Shibata. "Micromachining of diamond thin film," *New Dia. Frontier Carbon Techn*. 10(3): 161–175 (2000).

[6] N. Sepulveda, D. Aslam, and J. P. Sullivan. "Polycrystalline diamond MEMs resonator technology for sensor applications," *Diamond and Related Materials* 15(2/3): 398–403 (2006).

[7] A. R. Krauss, O. Auciello, D. M. Gruen, A. Jayatissa, A. Sumant, J. Tucek, D. C. Mancini, N. Moldovan, A. Erdemir, D. Ersoy, M. N. Gardos, H. G. Busmann, E. M. Meyer, and M. Q. Ding. "Ultrananocrystalline diamond thin films for MEMs and moving mechanical assembly devices," *Diamond and Related Materials* 10:1952–1961 (2001).

[8] K. Ohtsuka, K. Suzuki, A. Sawabe, and T. Inuzuka. "Epitaxial growth of diamond on iridium," *Jpn. J. Appl. Phys.* Pt. 2 35:L1072–L1074 (1996).

[9] K. Ohtsuka, H. Fukuda, K. Suzuki, and A. Sawabe. "Fabrication of epitaxial diamond thin film on iridium," *Jpn. J. Appl. Phys*. Part 2 Lett. 36: L1214–L1216 (1997).

[10] A. Sawabe, H. Fukuda, and K. Suzuki. "Heteroepitaxial growth of diamond," *Elec. Comm. Jap., Part 2 Elec.* 81(7):28–37 (1998).

[11] T. Saito, S. Tsuruga, N. Ohya, K. Kusakabe, S. Morooka, H. Maeda, A. Sawabe, and K. Suzuki. "Epitaxial nucleation of diamond on an iridium substrate by bias treatment, for microwave plasma-assisted chemical vapor deposition," *Diamond and Related Materials* 7: 1381–1384 (1998).

[12] T. Fujisaki, M. Tachiki, N. Taniyama, M. Kudo, and H. Kawarada. "Fabrication of heteroeptaxial diamond thin films on Ir(001)/MgO(001) substrates using antenna-edge-type microwave plasma-assisted chemical vapor deposition," *Diamond and Related Materials* 11: 478–481 (2002).

[13] M. Schreck, H. Roll, and B. Stritzker. "Diamond/Ir/SrTiO3: A material combination for improved heteroepitaxial diamond films," *Appl. Phys. Lett*. 74(5): 650–652 (1999).

[14] M. Schreck, H. Roll, J. Michler, E. Blank, and B. Stritzker. "Stress distribution in thin heteroepitaxial diamond films on Ir/SrTiO3 studied by x-ray diffraction, Raman spectroscopy, and finite element simulations," *J. Appl. Phys*. 88(5)**:** 2456–2466 (2000).

[15] Z. Dai, C. Bednarski-Meinke, R. Loloee, and B. Golding. "Epitaxial (100) iridium on A-plane sapphire: A system for wafer-scale diamond heteroepitaxy," *Appl. Phys. Lett*. 82(22): 3847–3849 (2003).

[16] Z. Dai, C. Bednarski-Meinke, and B. Golding. "Heteroepitaxial diamond film growth: the a-plane sapphire-iridium system," *Diamond and Related Materials* 13(4–8): 552–556 (2004).

[17] C. H. Lee, J. Qi, S. T. Lee, and L. S. Hung. "Epitaxial diamond on a Si/CaF2/Ir substrate," *Diamond and Related Materials* 12(8): 1335–1339 (2003).

[18] S. Gsell, T. Bauer, J. Goldfuss, M. Schreck, and B. Stritzker. "A route to diamond wafers by epitaxial deposition on silicon via iridium/yttria-stabilized zirconia buffer layers," *Appl. Phys. Lett*. 84(22)**:** 4541–4543 (2004).

[19] M. Schreck, S. Gsell, M. Fischer, T. Bauer, M. Schreck, and B. Stritzker. "Yttria-stabilized zirconia films of different composition as buffer layers for the deposition of epitaxial

diamond/Ir layers on Si(001)," *Diamond and Related Materials* 15(4–8): 479–485 (2006).

[20] S. J. Wang, C. K. Ong, L. P. You, and S. Y. Xu. –Epitaxial growth of yittria-stabilized zirconia oxide thin film on natively oxidized silicon wafer without an amorphous layer," *Semicon. Sci. Tech.* 15(8)**:** 836–839 (2000).

[21] G. Kimmel. –U3Si(Do_c) crystallographic type," *J. Less-Comm. Met*. 59**:** P83–P86 (1978).

[22] Z. Dai, A. Li, C. Bednarski, L. I. McCann, and B. Golding. –Epitaxial iridium growth on strontium titanate," *Mater. Res. Soc. Symp. Proceed*. 684**:** P11.35.1 (2001).

[23] C. Wild, P. Koidl, W. Müller-Sebert, H. Walcher, R. Kohl, N. Herres, R. Locher, R. Samlenski, and R. Brenn. –Chemical-vapor-deposition and characterization of smooth (100)-faceted diamond films," *Diamond and Related Materials* 2**:** 158–168 (1993).

[24] Y. von Kaenel, J. Stiegler, J. Michler, and E. Blank. –Stress distribution in heteroepitaxial chemical vapor deposited diamond films," *J. Appl. Phys*. 81(4)**:** 1726–1736 (1997).

[25] T. Aoyama, N. Amano, T. Goto, T. Abukawa, S. Kono, Y. Ando, and A. Sawabe. –Characterization of planar-diode bias-treatment in DC-plasma hetero-epitaxial diamond growth on Ir(001)," *Diamond and Related Materials* 16(3)**:** 594–599 (2007).

5 Summary

This section summarizes the key accomplishments of this LDRD project, describes the different media through which we communicated our results, discusses several of the main issues that we addressed, and considers future opportunities available to Sandia based on the project's success.

5.1 Key Accomplishments

This LDRD project yielded significant accomplishments in each of the three focus areas:

- Regarding phonon transport across interfaces, we computed the Kapitza conductance for Σ29(001) and Σ3(111) boundaries in silicon and proposed a new formulation for computing the Kapitza conductance. We fabricated these boundaries in single-crystal silicon substrates and imaged thermal waves crossing the boundaries using picosecond laser pulses. Our investigation of phonon transport across interfaces was performed in collaboration with Dr. Sylvie Aubry of Stanford University and Dr. David Hurley of Idaho National Laboratory.

- Through our investigation of phonon transport along interfaces, we designed and fabricated a differential test structure that is capable of quantifying phonon-surface interaction. As part of this work, we performed large-scale parallel Monte Carlo simulations to model the test ligaments and electrothermal simulations to model the complete test structure. The differential test structure was recently adopted by CINT as a standard platform for measuring the differential thermal conductance of nanowires.

- To further enhance our understanding of phonon transport, we grew diamond thin films by microwave plasma CVD on Ir/YSZ/Si surfaces and then fabricated MEMS devices from these films. The films show high quality and orientation. The MEMS devices were quite flat, showing very little out-of-plane bending that indicates very low out-of-plane stress gradients. Importantly, the ability to grow high-quality epitaxial diamond on silicon has only been duplicated by a few other groups in the world.

5.2 Communication of Results

Members of the Sandia team who contributed to this LDRD project were actively engaged in communicating the results and challenges of this work in phonon interaction. These communications took various forms. Four papers were published or in various stages of being published, five manuscripts were in preparation, one proposal was submitted. Two technical advances related to differential structures were filed. The project also organized two symposia on specific aspects of phonon engineering and made 13 presentations about the work. The list below identifies these achievements.

Publications (4)

- S. Aubry, C. Kimmer, A. Skye, and P. Schelling. "Comparison of theoretical and simulation-based predictions of grain-boundary Kapitza conductance in silicon," *Phys. Rev. B* 78: 064112–064120 (2008). [See Appendix A, Section A.1.]
- D. H. Hurley, O. B. Wright, O. Matsuda, and B. E. McCandless. "Imaging carrier and phonon transport in Si using ultrashort optical pulses," *Proc. SPIE* 7214: 721406 (2009). [See Appendix C.]
- D. H. Hurley, O. B. Wright, O. Matsuda, and S. L. Shinde. "Time resolved imaging of carrier and thermal transport in silicon," *Journal of Applied Physics*, in press. [See Appendix D.]
- D. H. Hurley, S. L. Shinde, and V. E. Gusev. "Lateral looking time-resolved thermal wave microscopy," submitted to *Journal of the Korean Physical Society* on December 14, 2009.

Manuscripts in Preparation (5)

- D. H. Hurley et al. "Time resolved thermal wave imaging across a Si-Si Twist boundary," *PRL*, to be submitted.
- E. S. Piekos et al. "A modified Holland model for Monte Carlo simulation of silicon and germanium," *Journal of Heat Transfer*, to be submitted.
- E. S. Piekos et al. "Monte Carlo simulation of structures for assessing phonon-surface interaction," Journal TBD, to be submitted.
- T. A. Friedmann et al. "Growth of chemical vapor deposited diamond on iridium and subsequent fabrication of diamond MEMS," *Diamond and Related Materials*, to be submitted.
- J. P. Sullivan et al. "Structure for determining phonon surface scattering by measuring differential heat conductance," *Journal of Heat Transfer*, to be submitted.

Proposals (1)

- Full Single Investigator, Small Group (SISGR) proposal submitted on April 21, 2009, to Basic Energy Sciences (BES) titled "Phonon transport in materials for energy harvesting"

Technical Advance Filings (2)

- "Device for Differential Thermal Conductance Measurements"
- "Apparatus for Assessing Gas-Surface Interaction"

Symposia Organization (2)

- S. L. Shinde organized a symposium on "Phonon Engineering – Theory and Applications" for the MRS Fall Meeting, November 26–30, 2007, Boston, MA.

– S. L. Shinde organized a symposium on ~~–~~Phonon Engineering for Enhanced Materials Solutions – Theory and Applications" for the MRS Fall Meeting, November 30–December 4, 2009, Boston, MA.

External Presentations (13)

– Three presentations at the Materials Research Society (MRS) Fall Meeting, November 26–30, 2007, Boston, MA

- ~~–~~Phonon-mediated Thermal Transport in Microsystems," S. Aubry, C. Kimmer, P, Schelling, E. S. Piekos and L. M. Phinney
- ~~–~~Computational Investigation of Thermal Property Measurement Techniques," E. S. Piekos and L. M. Phinney
- ~~–~~Growth and Processing of Diamond Films for Nanoscale Thermal Management Applications," T. A. Friedmann, J. P. Sullivan, and S. L. Shinde

– Two presentations at the MRS Fall Meeting, December 1–5, 2008, Boston, MA

- ~~–~~Structure for Measurement of Phonon Scattering from Silicon Nanowire Surfaces," J. P. Sullivan," T. A. Friedmann, E. S. Piekos, S. L. Shinde, and J. R. Wendt
- ~~–~~Growth and MEMS Processing of Diamond Films on Ir Buffer Layers on Silicon," T. A. Friedmann, J. P. Sullivan, E. S. Piekos, and S. L. Shinde

– One presentation at the American Physical Society (APS) March Meeting, March 16–20, 2009, Pittsburgh, PA

- ~~–~~Platform for Measurement of Phonon Scattering from the Surface of Silicon Nanostructures," J. P. Sullivan, T. A. Friedmann, E. S. Piekos, S. L. Shinde, and J. R. Wendt

– Five presentations at the MRS Fall Meeting, November 30–December 4, 2009, Boston, MA

- ~~–~~Nucleation, Growth, and Processing of Oriented Diamond Films for MEMS Applications," T.A. Friedmann, J. P. Sullivan, S. L. Shinde, and E. S. Piekos
- ~~–~~Theoretical and Simulation-Based Predictions of Grain Boundary Kapitza Resistance in Semiconductors," S. Aubry (Stanford), P. Schelling (University of Central Florida), C. Kimmer (University of Louisville), and X. Zhou and R. Jones (Sandia National Laboratories, Livermore)
- ~~–~~Structure for Measurement of Phonon Scattering from Si Nanowire Surfaces," J. P. Sullivan, T.A. Friedmann, E. S. Piekos, S. L. Shinde, and J.R. Wendt
- ~~–~~Monte Carlo Simulation of Phonon Transport in a Surface Scattering Measurement Structure," E. S. Piekos, J. P. Sullivan, T. A. Friedmann, and S. L. Shinde
- ~~–~~Time Resolved Thermal Transport Measurements Across a Si-Si Twist Boundary," D. H. Hurley, S. L. Shinde, and S. Aubry

- One presentation at the Symposium on Laser Spectroscopy, November 11–12, 2009, Daejeon, Korea
    - "Lateral Looking Time-Resolved Thermal Wave Microscopy," D. H. Hurley, S. L. Shinde, and V. E. Gusev
- One presentation at Photonics West, January 25–29, 2009, San Jose, CA
    - "Imaging Carrier and Phonon Transport in Si Using Ultrashort Optical Pulses," D. H. Hurley, O. B. Wright, O. Matsuda, B. E. McCandless, and S. L. Shinde

5.3 Issues Addressed

We were aware at the beginning of this project that many basic questions regarding phonon behavior remain unanswered. Simply working in this area therefore placed us firmly on the leading edge. Even among researchers of phonon behavior, this project was unique because it combined modeling, experimentation, and device design from the outset. This combination of viewpoints, tightly coupled at every stage, presented the best possibility of increasing our fundamental knowledge and applying this knowledge in revolutionary ways. While great care was taken to design well-controlled experiments and build sophisticated models, we recognized that some risk is always present when making comparisons. We minimized this risk by closely coupling the measurement and modeling activities to foster extensive communication in both directions.

In our investigation of phonon transport across interfaces, we faced several challenges: calculation of the Kapitza conductance of selected grain boundaries, actual fabrication of the twisted boundary stacks, and measurement of the Kapitza conductance of the individual boundaries. To assist in the modeling effort, we collaborated with Dr. Sylvie Aubry of Stanford University. While there were challenges in fabricating multiple controlled twist boundaries in silicon, we made substantial improvements in the process through optimization of surface treatments and annealing. And after exploring several techniques for measuring the Kapitza conductance of our fabricated samples, we developed a collaboration with Dr. David Hurley of Idaho National Laboratory for ultrafast laser imaging.

Our development of the differential thermal test structure was challenging from both fabrication and measurement perspectives. We minimized the risk by (1) using a structure that is similar in concept to a very successful design by Majumdar's group at U.C. Berkeley and (2) by performing simulations before fabrication to ensure that the desired effects would be measurable.

Growth of epitaxial diamond thin films on silicon requires development of the capability of growing the requisite buffer layers followed by diamond nucleation and growth. We made substantial progress in depositing epitaxial diamond films on iridium thin films deposited on the YSZ buffer layers, which were in turn deposited on silicon single crystals.

5.4 Future Opportunities

This LDRD project developed a critical understanding of phonon transport using modeling and experiments of phonon flow both across and along interfaces. At all stages of the project,

from design to data analysis, we maintained a tight coupling between modeling and experimentation. We used a variety of techniques to simulate phonon flow, including molecular dynamics, Monte Carlo, and continuum modeling. Similarly, using a combination of fabrication techniques, we created nanostructures in silicon and high-quality diamond.

Through a tightly coordinated team effort, we have demonstrated that a physics-based, bottom-up approach to heat transfer can enable needed innovation in thermal management for high-power applications, as well as the design of ground-breaking devices whose functionality is derived from phonon behavior unique to nanoscale geometries. Understanding and controlling phonon transport in small-scale structures is critical for Sandia's efforts in engineering structures where the phonon transport is ~~"e~~ontrolled." Such control will open a new set of applications in diverse areas viz. thermal management to allow colocation of high- and low-power devices to enable miniaturization, more efficient operation of SAW devices by controlling phonon reflections from interfaces, generalized schemes for phonon channeling with applications in acoustics and energy harvesting, and phonon-engineered devices where phonon-electron interactions are used to create new functionalities. By communicating our results widely and collaborating with researchers at other institutions, we have expanded the opportunities in the phonon transport field for Sandia. This project has direct relevance to technologies like MESA-SAR, where high-power devices such as high-power amplifiers that run at 150°C need to be placed next to low-power application-specific integrated circuits (ASICs) that must remain below 80°C. Channeled phonon transport will enable miniaturization of these systems and is crucial for realizing the miniaturization needed in space-based systems. The physics models developed in this LDRD project are also highly relevant to Sandia's work in thermoelectrics for energy harvesting and in electronics and optoelectronics. Contributions in these areas will provide a differentiating strength in Sandia's pursuit of new funding opportunities in energy efficiency and new energy technologies.

Appendix A. Phonon Transport Across Interfaces: Simulations of the Kapitza Conductance

The contents of this appendix describe simulations performed to compute the Kapitza conductance for silicon (Si) grain boundaries and silicon/silicon dioxide (Si/SiO_2) interfaces. These simulations supported the study of phonon transport across interfaces discussed in Section 2. Section A.1 contains a manuscript pertaining to the Si grain boundaries. This work was published in *Phys. Rev. B*, 78:064112–064120 (2008). The authors of the original paperwork were S. Aubry, C. Kimmer, A. Skye, and P. Schelling. Section A.2 describes the simulations related to the Si/SiO_2 interfaces. Sections A-1 and A-2 share the same set of references, as listed in Section A.3.

A.1 A Comparison of Theoretical and Simulation-Based Predictions of Grain-Boundary Kapitza Conductance in Silicon

We present a comparison between molecular-dynamics (MD) simulation and theoretical calculations using input from wave-packet simulations of the Kapitza conductance of two different grain boundaries in silicon. We find that for a Σ3(111) twin boundary with minimal disruption of the lattice the Kapitza conductance is extremely high in contrast to previous results obtained for the Σ29(001) grain boundary. Theoretical predictions based on input from wave-packet simulations appear to show reasonable agreement with MD results for the Σ29(001) grain boundary, but disagreement by a factor of about 10 for the Σ3(111) boundary. The origin of the apparent discrepancies is analogous to previously noted difficulties in comparing theoretical predictions to experimental measurements of the Kapitza conductance. We show why the apparent discrepancies are large when the interface phonon transmission is high and relatively small when the phonon transmission is low. We demonstrate how the theoretical predictions and MD simulation results can be compared in a consistent and meaningful way, thereby removing the apparent contradictions. These questions also are discussed in the important context of relating MD results to experimental observations. Finally, we show how insights obtained from theoretical and simulation comparisons might lead to new approaches to understand and tailor the interaction between bulk and interfacial properties.

A.1.1 Introduction

As devices become smaller and smaller, material geometries such as grain boundaries increasingly dominate heat transfer processes. Understanding how grain boundaries and more generally material geometries affect thermal transport in semiconductors is thus nowadays indispensable.

At grain boundaries or interfaces between dissimilar materials there is an added resistance to phonon-mediated heat transport [1, 13]. The thermal resistance, usually called the Kapitza resistance, results in a temperature discontinuity ΔT at the interface. The Kapitza resistance R_K relates the thermal current J to the observed temperature discontinuity ΔT as $J = \frac{\Delta T}{R_K}$. Alternately,

the transport properties of the interface can be quantified using the Kapitza conductance $\sigma_K = \frac{1}{R_K}$.

Theoretical studies usually rely on the acoustic-mismatch (AM) or diffuse-mismatch (DM) models, which make predictions for σ_K using simple descriptions of interfacial phonon scattering. Molecular-dynamics (MD) simulation has recently emerged as a promising approach for investigating phonon scattering [8, 9, 10]. While MD can determine σ_K within a single simulation, it is still important to relate the fundamental phonon-scattering properties to the overall σ_K. By establishing a direct relationship between phonon scattering and σ_K, important insight can be obtained to establish the relevance of simple theoretical models. In addition, by gaining further insight into the details of scattering at the interface, it might be possible to engineer interfaces that have tailored properties such as very high or low σ_K.

With the goal of obtaining detailed insight into interfacial scattering properties, the wave-packet simulation method was developed [3, 9, 10]. The basic idea is to create localized wave packets through a superposition of normal modes of a bulk perfect crystal. The wave packets are then propagated using MD simulation. After interacting with an interface, the energy transmission coefficient $\alpha(\lambda, \vec{k})$ is determined for each polarization λ and wave vector $\vec{k}$ as the fraction of incident energy that propagates across the interface. To determine σ_K, we use the expression [7, 17]

$$\sigma_K(T) = \frac{1}{\Omega}\sum_{\lambda,\vec{k}}^{+} \hbar\omega(\lambda,\vec{k}) v_z(\lambda,\vec{k}) \frac{\partial N_0[\omega(\lambda,\vec{k}),T]}{\partial T} \alpha(\lambda,\vec{k}), \tag{A-1}$$

where Ω is the system volume, $\omega(\lambda,\vec{k})$ is the frequency of a normal mode with polarization λ and wave vector $\vec{k}$, $v_z(\lambda,\vec{k})$ is the component of the phonon group velocity perpendicular to the interface plane, and $N_0[\omega(\lambda,\vec{k}),T]$ is the equilibrium Bose distribution. The plus sign on the summation indicates that modes with positive group velocity only are included. It is important to note that this expression is applicable for grain boundaries where the material on either side of the interface is identical. For hetero-interfaces, the modes on either side of the interface have to be explicitly included in an expression for σ_K. To compare Equation A-1 with direct MD simulation it is necessary to take the high temperature or classical limit since MD is a classical simulation method. We have previously shown [3] that the predictions using Equation A-1 with $\alpha_{\lambda,\vec{k}}$ determined using wave-packet simulations agree fairly well with direct MD simulation for the case of a high-energy $\Sigma 29(001)$ grain boundary in silicon. In particular, using Equation A-1 we obtained $\sigma_K = 0.68$ GW/m^2 K compared with $\sigma_K = 0.80$ GW/m^2 K as determined with direct MD simulation at $T = 500$ K.

In this paper, we present results for a $\Sigma 3(111)$ twin boundary in silicon that show dramatic disagreement between the predictions of Equation A-1 and the results of direct MD simulation. We show that this situation is analogous to the conceptual difficulties encountered in relating theoretical models to experiment. In particular, it has been shown by Katerberg et al. [2] and also Pettersson and Mahan [7] that comparison between experiment and theory depends on an understanding of what temperature difference ΔT is measured in an experiment. We propose a

simple modification to Equation A-1 that improves dramatically the agreement between theoretical predictions and direct MD simulation for the case of weak phonon scattering at the highly ordered Σ3(111) grain boundary. For the case of strong scattering at the disordered Σ29(001) grain boundary, where the agreement between Equation A-1 and MD simulation is already reasonably good, the modification of Equation A-1 has a much smaller effect.

In Section A.1.2, we describe the simulation details. In Section A.1.3, we present the results, including a comparison between predictions using Equation A-1 and direct MD results. We also develop a modification of Equation A-1 and demonstrate improved agreement between the theoretical predictions and the MD simulations. In Section A.1.4, we present the discussion and conclusions, including some insight into how bulk and interface properties might be coupled.

A.1.2 Methodology

We obtained the structure used to study the Σ3(111) grain boundary by first orienting the crystal so that the [111] direction lies along the z-axis of the simulation cell. We then define a (111) plane at $z = 0$ and rotate atoms above this plane by $\phi = 60°$ about a [111] axis while keeping the atoms below the plane fixed. This operation does not change any of the bond lengths or angles at the interface but does disrupt the periodicity of the perfect crystal lattice. A cross section of the resulting interface is shown in Figure A-1. Periodic boundary conditions were applied in all three dimensions resulting in two grain boundaries in the supercell. The dimensions of the supercell in the grain-boundary plane (i.e., the $x - y$ plane) were $L_x = 3\sqrt{\frac{3}{2}}a$ and $L_y = 5\sqrt{\frac{1}{2}}a$. The length of the simulation cell along the z axis was chosen to be $L_z = 600\sqrt{3}a$. The entire simulation cell had 108, 000 atoms. We made two different calculations of transmission coefficients and Kapitza conductance for two different system sizes. All the results presented below are for the larger system described above except mentioned otherwise.

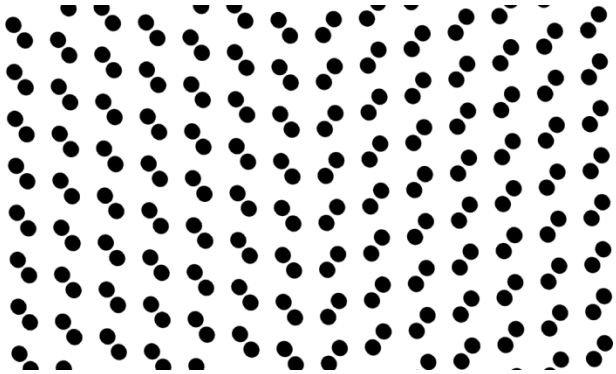

Figure A-1. A cross section of the Σ3(111) grain boundary.

We used the Stillinger-Weber (SW) potential for silicon that results in a lattice parameter $a = 0.543$ nm [12]. Because the bond lengths and bond angles in this structure are unchanged from the bulk perfect crystal, the SW potential predicts no energy difference between bulk and grain boundary atoms. This is due to the short-ranged nature of the SW potential since any

disruption of the lattice periodicity should result in some increase in the potential energy. However, the energy of this twin boundary should be very low. Furthermore, the loss of periodicity at the interface will still result in phonon scattering. We therefore believe that this model is appropriate for the problem at hand, although undoubtedly the quantitative results may be different for a more realistic potential.

We perform MD simulations to determine the Kapitza conductance using both the direct method and the wave-packet method. More details about the direct heat flux method can be found in [8, 9, 10], and more details about the lattice dynamics method can be found in [3] and references therein. In the direct method, a heat source and sink are used to generate a thermal current within a MD simulation. The thickness of the heat source and sink was $10a$ (i.e., 5.43 nm). At every MD time step, 9×10^{-4} eV of kinetic energy was added to the source region and removed from the sink region by rescaling the velocities of the atoms. Given the dimensions of the simulation supercell described above and the MD time step of $dt = 0.55$ fs, the heat current was about $J = 33.9$ GW/m^2. While this is rather large compared to some previous studies, we have found that a large heat current is necessary to establish a significant temperature discontinuity at the interface. The simulation began with 0.05 ns of simulation time at a constant temperature of $T = 500$ K, followed by 1.60 ns of simulation with the heat source and sink turned on. To obtain a time-averaged temperature profile, we included only the last 1.10 ns of the simulation. We have verified that the temperature profile is very steady for the final 1.10 ns of the simulation, demonstrating that the system readily achieves a steady state. We made a linear fit to the temperature gradient on either side of the interfaces, and used the difference in the temperature at the interface determined from the fits to compute ΔT.

For wave-packet simulations, we used the same approach described in an earlier work [3]. We determined the energy-transmission coefficients $\alpha(\lambda, \vec{k})$ as a function of wave vectors $\vec{k}$ and acoustic branch λ using MD. The first Brillouin zone was sampled by performing a simulation for each branch λ. The wave vector components k_x and k_y are fixed for each simulation while k_z (i.e., the component normal to the interface) is varied for each wave packet. We considered 41 wave vectors in this study. The central wave vector and frequencies of each wave packet is chosen to achieve a uniform frequency sampling of the dispersion relation for each branch. One simulation for each branch and pair (k_x, k_x) consistent with the periodic simulation box was performed. Typically, simulations for optical modes are prohibitively expensive because group velocities are rather low, requiring long simulation times. As described below, we estimate the contribution from the optical branches based on a few limited simulations of longitudinal optical (LO) modes with normal incidence on the boundary.

We have performed simulations corresponding to a complete set of nonnormal incidence phonon branches for LA and TA modes. Each branch was sampled at a frequency interval of 0.8 THz. In other words, a separate wave packet was added to the simulation for each 0.8 THz of frequency. As previously noted [3], the accuracy of the quadrature used to evaluate Equation A-1 can be investigated. We find that the 0.8 THz sampling is accurate to within 15% in the high-temperature limit.

A.1.3 Simulation Results and Theoretical Predictions

In Figure A-2 we show the computed temperature profile in the MD simulation cell using the direct method. The temperature discontinuity is extremely small, indicating that the grain boundary is having a very small effect on the thermal transport. The temperature discontinuities are 1.80 K and 4.23 K at the two boundaries. The average for the two grain boundaries gives $\Delta T = 3.02$ K. Using this value and the incident heat current $J = 33.9$ GW/m^2, we obtain $\sigma_K = 11$ GW/m^2 K. However, due to the fairly large estimated error in ΔT ($\pm$ 1.5 K), we were able to definitively place σ_K between about 7.0 GW/m^2 K and 22 GW/m^2 K. This is the largest computed value of σ_K for an Si grain boundary by nearly a factor of about 10, and is comparable to some values recently obtained for diamond grain boundaries [16].

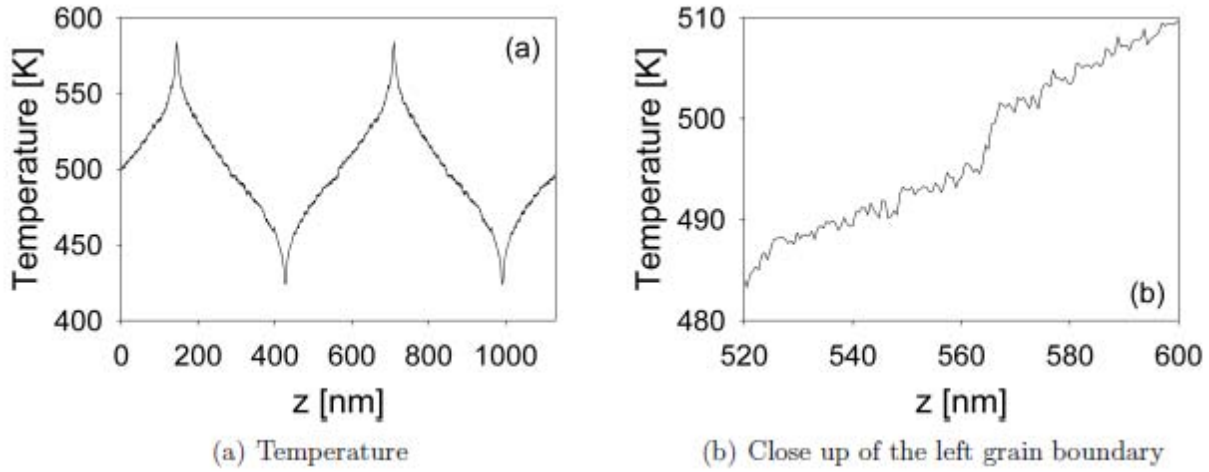

(a) Temperature (b) Close up of the left grain boundary

Figure A-2. Time-averaged temperature profile obtained from direct MD simulation of thermal transport though Σ3 grain boundaries. (a) The boundaries' positions are at about $z = 282$ nm and $z = 565$ nm. The actual simulation cell spans from $z = 0$ to $z = 565$ nm. (b) The temperature near the grain boundary at $z = 565$ nm is shown in closer perspective to see the temperature discontinuity at $z = 565$ nm.

The wave-packet simulations confirm the expectation that interfacial scattering is very weak. In Figure A-3 we show the transmission coefficient versus frequency for several LA branches. With the exception of some of the high-frequency modes, the scattering of LA modes is almost imperceptible, with $\alpha \sim 1$ for much of the spectrum. By contrast, TA modes display somewhat stronger scattering as shown in Figure A-4. Results presented in Figures A-3 and A-4 are for a system $L_z = 600\sqrt{3}a$ long. We have calculated transmission coefficients for a smaller system for comparison. Both systems give very similar results. In comparison to previous results for the Σ29(001) grain boundary [3], strong correlation between frequency and α is less apparent. For example, while the LA modes seem to scatter only for frequencies above $\sim$ 10 THz, the TA modes show much stronger dependence on the particular wave vector and polarization. In general, the computed values of α for the current study are much higher in comparison to those found for the Σ29(001) grain boundary.

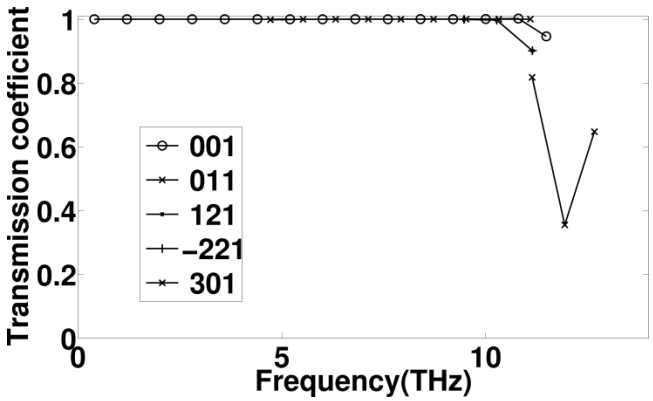

Figure A-3. Energy-transmission coefficients as a function of frequency computed for various LA branches. Each branch is labeled by the particular values of *m* and *n* as $[\mathrm{mn1}]$. For instance, the case of normal incidence corresponds to the branch labeled [001] (i.e., $m = 0$ and $n = 0$).

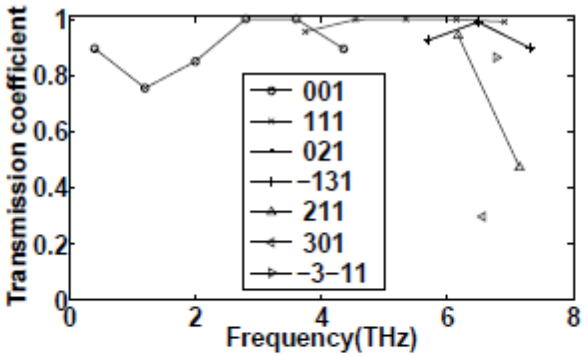

(a) TA branch along $(10\bar{1})$

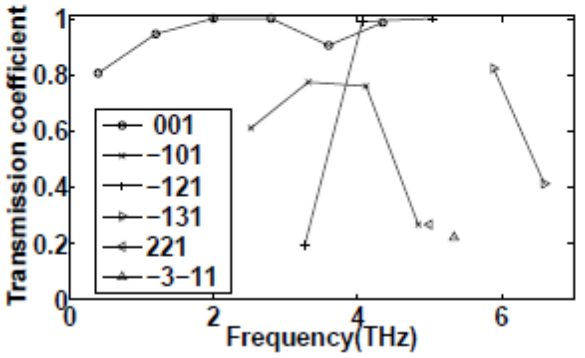

(b) TA branch along $(\bar{1}2\bar{1})$

Figure A-4. (a)Transmission coefficient plotted as a function of frequency for various TA branches polarized along $[10\bar{1}]$. (b) Transmission coefficient plotted as a function of frequency for various TA branches polarized along $[\bar{1}2\bar{1}]$.

Figure A-5 shows the results for the calculation of the Kapitza conductance using Equation A-1. We use wave-packet simulations only to determine α for the LA and TA modes. To estimate the contribution from the optical branches, we assume $\alpha = 0.25$ for all of the optical branches. This value is based on our previous study of a few optical modes incident on the Σ29(001) grain boundary. The results are shown for the acoustic modes both with and without the estimated contribution from the optical modes. We see from Figure A-5 that the LO and TO modes account for about 10% of the energy transport. For comparison, we have also added to Figure A-6 the prediction based on the DM model which for a grain-boundary corresponds to $\alpha = 0.5$. Not surprisingly, the relatively large values of α obtained from the wave-packet simulations yield predictions for σ_K that are significantly higher than the DM model. To explore finite-size effects, we also studied a smaller system with $L_x = 2\sqrt{\frac{3}{2}}a$, $L_y = 2\sqrt{\frac{1}{2}}a$ and $L_z = 300\sqrt{3}a$ with a total of 24, 000 atoms. We find for this smaller system a value of σ_K that is only about 8% higher than the results found for the larger system. This indicates that the larger simulated system represents an adequate sampling of the Brillouin zone. Finally, we also determined σ_K in the so-called radiation limit where $\alpha = 1$ for the entire spectrum. In the high-temperature limit where classical statistics are valid, we obtain $\sigma_K = 1.96\ \mathrm{GW/m^2\ K}$.

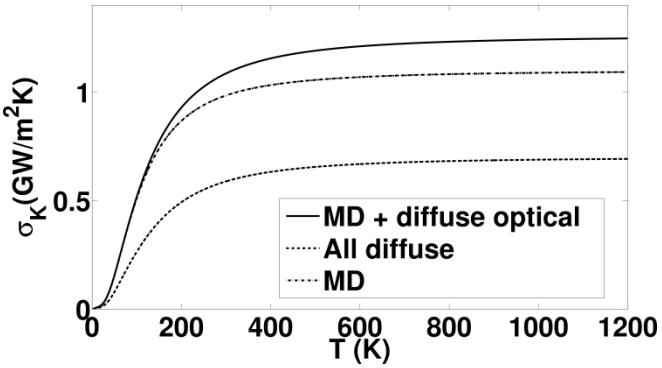

Figure A-5. The Kapitza conductance σ_K computed using Equation A-1 with transmission coefficients determined from MD simulation (dashed line). The solid line shows the calculated Kapitza conductance using the MD data for the acoustic branches plus an assumed uniform transmission coefficient of 0.25 for the optical branches. The lowest curve shows σ_K assuming diffuse scattering for the acoustic branches and a transmission coefficient of 0.25 for the optical modes.

Comparison between the theoretical predictions and the direct MD simulation results apparently exhibit a very large discrepancy for the Σ3(111) grain boundary. The relevant comparisons between the direct MD result and theoretical calculations based on Equation A-1 are shown in Table A-1. The theoretical predictions which use the wave-packet result give a value of nearly 63% the radiation limit. This demonstrates the very weak scattering of the interface, and also can somewhat justify the assumption of $\alpha = 0.25$ for the optical modes. In particular, even when we assume optical modes are strongly scattered, we obtain a value for σ_K that is not much less than the radiation limit. By contrast, the direct MD simulation results in a value for σ_K that is much greater than the radiation limit.

The rather dramatic disagreement between the theoretical model and the direct MD simulations has a straightforward explanation. The origin of the disagreement has been discussed by previous authors in the slightly different but closely related context of comparing theoretical predictions based on the AM, DM, or a more general model represented by Equation A-1, to experiment. In particular, it has been noted that in the limit of $\alpha = 1$ (i.e., the radiation limit), the theory predicts a finite resistance. This seems contradictory especially when one considers that $\alpha = 1$ is what one expects for an imagined interface in an ideal crystal.

However, Pettersson and Mahan have previously shown that the origin of the difficulty is in understanding exactly what temperature difference ΔT is measured in experiment [7]. For example, they observed that for an imagined interface with $\alpha = 1$, if the temperature difference ΔT is determined from the phonon distribution *incident* on the interface, Equation A-1 can be shown to be consistent with the usual theory of thermal diffusion. This observation suggests that Equation A-1 is appropriate in spite of the apparent paradox that h_K is finite even for an imagined interface.

Within the context of the AM model, the analogous theory to that presented in Equation A-1 due to Little [5] leads to a prediction $\sigma_K = 4\epsilon_1\alpha_{12}T^3$ where ϵ_1 is a parameter for material 1 and α_{12} is the energy-transmission coefficient for phonons incident from material 1 to material 2 averaged over all possible angles of incidence. It was noted by Simons [11] that, in addition to giving a finite resistance for an imagined interface, the phonon distribution used in the Little model did not result in a thermal current in the bulk. Using a nonequilibrium phonon distribution within the AM model, Simons [11] obtained the expression $\sigma_K = (4\epsilon_1\alpha_{12}T^3)(1 - \frac{1}{2}\beta_{12} - \frac{1}{2}\beta_{21})^{-1}$ where β_{12} and β_{21} are parameters closely related to α_{12}. When the interface weakly scatters phonons and the limit $\alpha \longrightarrow 1$ applies, it is appropriate to take $\alpha_{12} = \beta_{12} = \beta_{21}$. In the Simons theory, when an interface has $\alpha = 1$ (i.e., an imagined interface), then σ_K is infinite, and $h_K = 0$. Comparison of the Little and Simons theories shows that they make similar predictions for σ_K when scattering is very strong (i.e., small α), but exhibit strong disagreement when scattering is weak (i.e., $\alpha \sim 1$).

While the Little and Simons theories at first sight appear to be incompatible, Katerberg [2] showed that they are in fact equivalent as long as one knows exactly how to define ΔT. The relevant temperatures are shown schematically in Figure A-6. Katerberg showed that the Little theory is appropriate if the temperatures used to determine ΔT are consistent with the distribution of phonons incident on the interface. In other words, if a thermometer is in fact measuring the distribution of incident phonons with temperatures T_2 and T_1, then the Little theory is appropriate. By contrast, if the thermometer in the experiment is measuring the phonon distribution near the interface (i.e., $\Delta T = T_b - T_a$ in Figure A-6) then the Simons theory is appropriate.

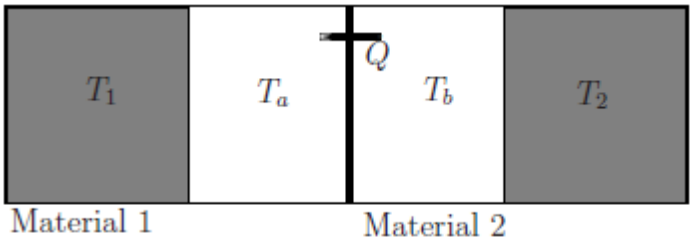

Figure A-6. The different temperatures involved in the direct heat flux method ($\Delta T = T_b - T_a$) and the lattice dynamics method ($\Delta T = T_2 - T_1$).

In light of these considerations, the apparently strong disagreement between direct MD results and the wave-packet predictions used in Equation A-1 can be understood. In the direct MD simulation, the temperature difference we use to compute ΔT is equivalent to $T_b - T_a$ in Figure A-6. However, based on the observations by Katerberg, the theory given by Equation A-1 should be appropriate when the temperature difference is characteristic of the phonon distribution incident on the interface (i.e., $\Delta T = T_2 - T_1$ in Figure A-6). In the case of the $\Sigma 3(111)$ grain boundary, the wave-packet results indicate that much of the spectrum corresponds to the limit $\alpha \longrightarrow 1$. In this limit, we expect the disagreement between the theoretical prediction from Equation A-1 and direct MD results to be large. As we have shown in Table A-1, that is indeed the case.

To bring the theoretical predictions into better agreement with direct MD results, it is necessary to make the appropriate comparison. Two possible approaches exist. One approach is to attempt to compute or estimate the temperature distribution of the normal modes incident on the interface. The other approach is to attempt to modify the theory in a manner analogous to the Simons AM model predictions.

Directly computing the distribution of normal modes incident on the interface is not a simple task. In principle, the atomic displacements and velocities can be used to compute the distribution of normal modes near the interface and isolate those that are incident on the interface from those that are traveling away from the interface. This is certainly possible, but would be extremely computationally intensive because the distribution of energy in each normal mode would have to be time averaged over the entire MD simulation. Also, the displacements and velocities would have to be convoluted with a window function (e.g., a Gaussian window) near the interface to isolate the relevant distributions. Alternately, a simple estimate can be made that illustrates the appropriate comparison. It has previously been shown that the mean free path in SW silicon is about $l_\infty = 100$ nm for $T = 500$ K. We follow Pettersson and Mahan [7] and assume that the temperature of normal modes incident on the interface can be determined from the local average temperature one mean free path away from the interface. In particular, using T_2 and T_1 to refer to the temperatures associated with modes incident on the interface at angle of incidence θ, we find

$$T_1 = T - \frac{T_b - T_a}{2} - \frac{dT}{dz} l_\infty cos\theta \qquad \text{(A-2)}$$

and

$$T_2 = T + \frac{T_b - T_a}{2} + \frac{dT}{dz} l_\infty cos\theta. \tag{A-3}$$

For the simulation of the Σ3(111) boundary, the average temperature gradient near the interface for the results in Figure A-2 is $\frac{dT}{dZ} = 0.274$ K/nm. Averaging over angles and including the $T_b - T_a = 3$ K discontinuity at the grain boundary, we obtain $\Delta T = T_2 - T_1$ to be about 24.5 K. Using this value for ΔT instead of the 3 K used to obtain σ_K in Table A-1, we find $\sigma_K = 1.38$ GW/m^2 K. Even with this very rough estimate, the comparison to the theoretical prediction of $\sigma_K = 1.23$ GW/m^2 K is already quite reasonable.

For the Σ29(001) grain boundary, wave-packet simulations and direct MD already are in reasonable agreement. In this case, the corrections are relatively small because the computed temperature discontinuity at the interface is large. The approximate temperature gradient for the Σ29(001) grain boundary simulations was 0.27 K/nm with an applied thermal current of $J = 15.36$ GW/m^2. The temperature discontinuity at the grain-boundary from a previous MD study [10] was found to be 19.2 K. Applying the same estimates as above to obtain the temperature of the normal modes incident on the grain boundary, we obtain for $\Delta T = T_2 - T_1$ a value of about 43.1 K. Using this temperature difference, we obtain the estimate $\sigma_K = 0.36$ GW/m^2 K. This is smaller by just over a factor of 2 from σ_K estimated from the discontinuity of 19.2 K determined from $\Delta T = T_b - T_a$ (i.e., from the temperatures near the grain boundary).

The main point to make is that estimated corrections to permit meaningful comparisons between the theoretical calculations and direct MD simulation are relatively small for the weakly-scattering Σ29(001) grain boundary. By contrast, the estimated corrections are large for the case of weak scattering at the Σ3(111) grain boundary. This is consistent with Katerberg's observation that the Little and Simons theories should disagree most strongly when the scattering is weak [2].

Next, we consider an alternate theory to that in Equation A-1 that can be compared directly to the MD simulation where ΔT is determined in the usual way from the temperature discontinuity at the interface (i.e., $\Delta T = T_b - T_a$). From Katerberg [2], it is clear that we need something equivalent to the Simons theory but more generally applicable beyond the AM model for phonon scattering. We begin by expressing the current in terms of the temperature distribution of normal modes incident on the interface. For waves incident on the grain boundary at temperatures T_1 and T_2, we have

$$J = -\frac{1}{\Omega} \sum_{\lambda \vec{k}}^{+} \hbar\omega(\lambda, \vec{k}) v_z(\lambda, \vec{k}) \alpha(\lambda, \vec{k}) \frac{dN_0[\omega(\lambda, \vec{k}), T]}{dT} (T_2 - T_1). \tag{A-4}$$

The next step is to relate $T_b - T_a$ to the temperature difference $T_2 - T_1$. It is first important to note that the relevant temperature for each normal mode will depend on where the last

scattering event in the bulk occurred. In other words, $T_2 - T_1$ should be considered to depend on the particular mode in branch λ with wave vector k. We introduce $\tau(\lambda, \vec{k})$ as the phonon lifetime to give the temperature of the incident waves in analogy to Equation A-2 and Equation A-3,

$$T_1 = T - \frac{T_b - T_a}{2} - \frac{dT}{dz} v_z(\lambda, \vec{k})\, \tau(\lambda, \vec{k}) \tag{A-5}$$

and

$$T_2 = T + \frac{T_b - T_a}{2} - \frac{dT}{dz} v_z(\lambda, \vec{k})\, \tau(\lambda, \vec{k}). \tag{A-6}$$

If we take the interfacial current given by Equation A-4 and set it equal to the standard expression for the bulk current in the presence of a temperature gradient $\frac{dT}{dz}$,

$$J = -\frac{1}{\Omega} \sum_{\lambda \vec{k}} \hbar\omega(\lambda, \vec{k}) v_z^2(\lambda, \vec{k}) \tau(\lambda, \vec{k}) \frac{dN_0[\omega(\lambda, \vec{k}), T]}{dT} \frac{dT}{dz} \tag{A-7}$$

and then use $J = \sigma_K (T_b - T_a)$ to define the σ_K (i.e., in terms of the discontinuity at the interface $T_b - T_a$), we obtain

$$\sigma_K = \frac{1}{\Omega} \left[\sum_{\lambda \vec{k}}^{+} \hbar\omega(\lambda, \vec{k}) v_z(\lambda, \vec{k}) \alpha(\lambda, \vec{k}) \frac{dN_0}{dT} \right] \times \frac{\sum_{\lambda \vec{k}} \hbar\omega(\lambda, \vec{k}) v_z^2(\lambda, \vec{k}) \tau(\lambda, \vec{k}) \frac{dN_0}{dT}}{\sum_{\lambda \vec{k}} \hbar\omega(\lambda, \vec{k}) v_z^2(\lambda, \vec{k}) \tau(\lambda, \vec{k}) (1 - \alpha(\lambda, \vec{k}) \frac{dN_0}{dT}}. \tag{A-8}$$

This expression is derived to apply to the case where the temperature discontinuity is defined in terms of the temperatures near the interface (i.e., $\Delta T = T_b - T_a$). When Equation A-8 is applied to the case of an imagined interface with $\alpha = 1$ for each mode, we see that σ_K diverges. This means that for an imagined interface, $h_K = 0$ and $T_b - T_a = 0$. By contrast, the theoretical expression for σ_K in Equation A-1 is finite for the limit $\alpha = 1$. While Equation A-1 and Equation A-8 make very different predictions when $\alpha \to 1$, in the limit where $\alpha \to 0$ the two expressions converge to the same result. It is clear that Equation A-8 is comparable to the Simons theory, whereas Equation A-1 is closely related to approach due to Little. Hence, we

expect that Equation A-8 is appropriate for comparison to MD simulation results when σ_K is defined in terms of the temperature discontinuity $T_b - T_a$.

To compare the predictions made by Equation A-8 to direct MD simulation, we have to evaluate the summations in some approximation because $\tau(\lambda, \vec{k})$ is not exactly known. One reasonable approximation is to assume a constant relaxation time τ for each normal mode due to anharmonic phonon-phonon interactions. We also take the limit of classical statistics where the heat capacity of each mode is k_B. In this approximation, the expression for the Kapitza conductance is

$$\sigma_K = \frac{\frac{k_B}{\Omega}\left[\sum_{\lambda\vec{k}}^{+} v_z(\lambda, \vec{k})\alpha(\lambda, \vec{k})\right]\left[\sum_{\lambda\vec{k}} v_z^2(\lambda, \vec{k})\right]}{\sum_{\lambda\vec{k}} v_z^2(\lambda, \vec{k})\left[1 - \alpha(\lambda, \vec{k})\right]}. \tag{A-9}$$

Another reasonable approach is to assume a constant mean free path. In other words, if we assume that for each mode $v_z(\lambda, \vec{k})\tau(\lambda, \vec{k})$ is a constant independent of λ and $\vec{k}$, we then obtain the expression

$$\sigma_K = \frac{\frac{k_B}{\Omega}\left[\sum_{\lambda\vec{k}}^{+} v_z(\lambda, \vec{k})\alpha(\lambda, \vec{k})\right]\left[\sum_{\lambda\vec{k}}^{+} v_z(\lambda, \vec{k})\right]}{\sum_{\lambda\vec{k}}^{+} v_z(\lambda, \vec{k})\left[1 - \alpha(\lambda, \vec{k})\right]}. \tag{A-10}$$

A comparison of the predictions using Equations A-1, A-9, and A-10 is given in Table A-1. We see from the results in Table A-1 that Equation A-9 appears to agree more closely with direct MD. In particular, the results for the Σ3(111) grain boundary are in much better agreement, whereas the Σ29(001) results remain reasonably close. It is important to acknowledge that while the Σ3(111) results are in much better agreement with either Equation A-9 or Equation A-10, the Σ29(001) grain boundary is actually in slightly better agreement with Equation A-1. However, we believe that the approach outlined here is more appropriate than the previous approach based on Equation A-1.

Table_A-1. Values of σ_K in GW/m^2 K Determined by Direct MD Simulation and Theoretical Calculations Based on Equations A-9 and A-10 with Input from Wave-Packet Simulations

Method	Σ3(111)	Σ29(001)
Direct MD (T = 500 K)	11.0	0.80
Theory (Equation A-1)	1.23	0.68
Theory (Equation A-9)	8.35	1.52
Theory (Equation A-10)	6.34	1.40

Results in Table A-1 for direct MD simulation and theory based on Equation A-1 of the Σ29(001) grain boundary are taken from [3]. The theoretical predictions given include estimated contributions from the optical branches.

The transmission coefficient within a particular phonon branch for the Σ29(001) grain boundary has been observed to be primarily a function of the incident phonon frequency $\omega(\lambda, \vec{k})$ [3]. To estimate the uncertainty in any estimates using the available MD data and Equations A-9 and A-10, we fit the Σ29(001) data to a quintic polynomial function of frequency for each phonon branch. With the fit function, the convergence of the summations over the first Brillouin zone can be studied for various sampling or discretization schemes. We determine the relative difference between the uniform-frequency sampling scheme used to sample the Brillouin zone with MD and the complete summation over wave vectors compatible with the periodic simulation cell. We obtain an error of 24.5% for Equation A-9 and an error of 9.25% for Equation A-10. The uncertainty using Equation A-1 is 16%, which shows that assuming the $v_z\tau$ to be constant tends to reduce the uncertainty while assuming the relaxation time constant tends to increase it. These trends in the uncertainties can follow from the general observation that the modes with smallest $\vec{k}$ tend to have $\alpha \to 1$ while those with the smallest group velocity tend to $\alpha \to 0$. The smallest-$\vec{k}$ modes with high transmission (i.e., those having large group velocity) are weighted the most leading to greater relative error due to the v_z^2 term in Equation A-10.

We cannot make the same comparison for the Σ3(111) grain boundary because the transmission coefficients are not as well approximated as a function of frequency. We can, however examine the convergence of the sum in each formula that is independent of the transmission coefficient. We estimated an error of 14% in the calculations of the sum in the numerator of Equation A-9, and an error of 5% for Equation A-10. For the Σ29(001) grain boundary, the uncertainties in these formulas follow the same trends noted in the previous paragraph, with an uncertainty of 18.3% from Equation A-9 and 6.8% for Equation A-10.

We discuss some of the limitations and uncertainties that remain in the next section.

A.1.4 Discussion and Conclusions

We have presented results for phonon scattering and Kapitza conductance for two different grain boundaries in silicon. In comparing theoretical predictions to MD simulation results, we have shown that it is important to consider the appropriate definition for the temperature discontinuity. When MD simulation uses the temperature discontinuity at the interface $T_b - T_a$ shown in Figure A-6, then it is more appropriate to use a definition for σ_K given by either Equation A-9 or Equation A-10 than Equation A-1. In the case of weak interfacial scattering, such as the Σ3(111) grain boundary studied here, the modified expressions for σ_K in Equation A-9 or Equation A-10 are able to treat the limit where σ_K exceeds the so-called radiation limit.

As Katerberg had previously shown when contrasting the Simons and Little theories, the difficulty lies in understanding what approach is equivalent to experiment. In particular, it is important to understand whether the experimental system measures the discontinuity at an interface as $T_2 - T_1$ or $T_b - T_a$. In an MD simulation, $T_b - T_a$ is very straightforward to determine, whereas $T_2 - T_1$ is not. Therefore, we have instead developed a theory for σ_K using a

definition based on the temperature discontinuity $T_b - T_a$ and interface transmission coefficients $\alpha(\lambda, \vec{k})$. For the Σ3(111) grain boundary, characterized by very weak scattering, the new theory is in much better agreement with direct MD simulation.

There is still a high degree of uncertainty that leaves the theoretical predictions only within a factor of about two of the direct MD results. In particular, the theory depends on some approximate treatment of scattering in the bulk. While the new approach given by either Equation A-9 or Equation A-10 is much better for the Σ3(111) grain boundary, the agreement for the Σ29(001) boundary is somewhat worse. To achieve better agreement, we think a more detailed understanding of bulk scattering is needed. For example, we might imagine going beyond the approximations outlined above and use the standard expression for normal and Umklapp scattering rates $\tau(\lambda, \vec{k})^{-1} = B\omega(\lambda, \vec{k})^2$. We have in fact tried this, but found that our results did not converge uniformly as we improved our sampling of the Brillouin zone due to the $\left(\frac{1}{\omega}\right)^2$ dependence of the scattering time. It was therefore not possible to obtain an unambiguous result. However, it should still be possible to further improve upon the constant relaxation time and mean-free-path approximations to achieve better results.

These observations help elucidate the practical and conceptual challenge of making comparisons between theoretical models and experiments. For example, many experimental configurations measure $T_2 - T_1$. In this case, the direct MD simulations, which most conveniently compute $T_b - T_a$ may not result in predictions for σ_K that can compare meaningfully to experiment. Instead, one can determine $T_b - T_a$ from direct MD simulation, and then use Equations A-2–A-3 to estimate $T_2 - T_1$ and hence obtain a value of σ_K that can be directly compared to experiment. By contrast, sometimes one is able to determine an ~~–~~effective" conductivity κ_{eff}. For example, in a polycrystalline or nanocrystalline material, we can assume

$$\kappa_{eff} = \frac{\kappa}{1 + \frac{\kappa}{\sigma_\kappa d}}, \tag{A-11}$$

where κ is the bulk thermal conductivity and d is the grain size. In this case, it is more appropriate to consider σ_K in terms of the discontinuity $T_b - T_a$.

Another interesting possibility suggested by this work is that there is a close connection between σ_K and the scattering that is occurring in the bulk. In particular, when σ_K is defined based on $T_b - T_a$. Equation A-8 suggests that σ_K depends on the details of bulk scattering and not solely on what happens at the interface. This point is established through comparison of the predictions obtained from Equation A-9 to those of Equation A-10, which differ only in how bulk scattering is approximately treated. However, it is interesting to consider what might happen with dopants or point defects that have scattering rates $\tau^{-1} = A\omega^4$, or even the limit of nanoscale grain size. In this case, scattering due to details in the bulk of the material, or at neighboring grain boundaries, appears to have an effect on the discontinuity $T_b - T_a$. The connection between bulk and interface scattering is largely unexplored, but may provide a path

for greater understanding or control of interfacial properties. For nanoscale systems, our results also suggest the possibility that interfacial scattering events cannot be treated separately.

A.2 Kapitza Conductance of Si/SiO_2 Interfaces

A.2.1 Introduction

Silicon–silicon dioxide interfaces are important in semiconductor transistors. For instance, they can be used as gate oxide [6]. The unique role of silicon in semiconductor technology is due largely to the remarkable properties of the Si/SiO_2 interface and other electrically active defects. Although silicon is crystalline and silicon dioxide is amorphous, the interface is essentially perfect, with an extremely low density of dangling bonds or other electrically active defects [14]. Silicon-on-insulator devices suffer from the problem of severe self-heating, as the insulating oxide layer with a very low thermal conductivity inhibits heat removal. In metal-oxide silicon structures, it was shown that the interfacial resistance plays a significant role in self-heating of the devices [6]. These show that there is a critical need to understand transport and other properties of $Si\text{-}SiO_2$ interfaces.

Despite its essential role, the atomic structure of Si/SiO_2 interfaces is still unclear. In this work we focused on known silicon-dioxide structures such as α-quartz, β-quartz, cristobalite, and tridymite.

At grain boundaries or interfaces between dissimilar materials there is an added resistance to phonon-mediated heat transport [1, 13]. The thermal resistance, usually called the Kapitza resistance, results in a temperature discontinuity ΔT at the interface. The Kapitza resistance R_K relates the thermal current J to the observed temperature discontinuity ΔT as

$$J = \frac{\Delta T}{R_K}. \tag{A-12}$$

Alternately, the transport properties of the interface can be quantified using the Kapitza conductance

$$\sigma_K = \frac{1}{R_K}.$$

A.2.2 Thermal Conductance in Si/SiO2 Systems

To compute the Kapitza conductance in Si/SiO_2 systems, we used a method analogous to compute the thermal conductivity explained in [18] and the Kapitza resistance using the direct heat flux method described in [10].

The thermal conductivity of a homogeneous system can be computed using an equilibrium MD simulation and the Green-Kubo formalism. However, for an inhomogeneous system such as

interfaces or grain boundaries, this approach is not appropriate, because the Kapitza conductance is a local property, which cannot be correctly treated under the assumption that the system is homogeneous. Another approach is to use a nonequilibrium MD simulation method. The basic idea is to create a thermal current in the MD simulation cell, and then use the resulting temperature profile to compute the thermal conductivity. For a bulk perfect crystal, the temperature gradient in the presence of a thermal current allows us to calculate the perfect crystal thermal conductivity [8, 18]. For an interface, the temperature discontinuity ΔT at the interface can be used to compute the Kapitza conductance from Equation A-12.

To create a thermal current along the length of the simulation L, we rescale the particle velocities at each MD time step in two thin slabs each of thickness w. In one slab located at $z = 0$, we add energy $\Delta\epsilon$ at each MD step, and we remove energy $\Delta\epsilon$ from another slab located at $z = L/2$ thereby conserving the total energy at all times. We also are careful to conserve linear momentum. The resulting thermal currents J_z flow from the hot region with $+\Delta\epsilon$ to the cold region with $-\Delta\epsilon$.

The simulation cell contains a pure silicon part and a silicon dioxide part. The silicon dioxide is chosen among the following silicon dioxide known structures: α- quartz, β-quartz, cristobalite, and tridymite and are described later.

A.2.3 Watanabe's Si/SiO_2 Potential

In order to simulate a silicon–silicon dioxide interface and to determine its Kapitza resistance, it is important to identify a potential that represents its structure and captures the transport behavior. The potential developed by Watanabe et al. [15] is a new interatomic potential function that is applicable to most of Si, O mixed systems, from SiO_2 to Si crystals. It is an extended form of the SW potential for silicon [12]. This is a distinctive advantage in large-scale MD (molecular dynamics) simulations. However, it omits long-range Coulomb interaction that exists in silica. In spite of drastic simplification, it can reproduce the stability of silica polymorphs and the radial distribution function of a-SiO_2. This potential is applicable to the Si/SiO_2 interface, which can be treated by very few potentials.

Any potential-energy function Φ describing interactions among N identical particles can be revolved into one body, two-body, three body, etc., contributions:

$$\Phi(1, \dots, N) = \sum_i v_1(i) + \sum_i \sum_{j,j>i} v_2(i,j) + \sum_{i,j,k} \sum_{i<j<k} v_3(i,j,k) + \cdots + v_N(1, \dots, N).$$

The term v_1 describes wall and external forces to which the system is subject. It equals zero here.

The SW potential is based on the approximation that the potential Φ can be approximated by two- and three-body terms only. This implies

$$\Phi(1, \dots, N) = \sum_i \sum_{j,j>i} v_2(r_{ij}) + \sum_{i,j,k} \sum_{i<j<k} v_3(r_i, r_j, r_k),$$

where

$$v_2(i,j) = \epsilon f_2\left(\frac{r_{ij}}{\sigma}\right)$$

and

$$v_3(r_i, r_j, r_k) = \epsilon f_3(r_i/\sigma, r_j/\sigma, r_k/\sigma).$$

The two-body and three-body forces f_2 and f_3 are defined by

$$f_2(i,j) = g_{ij} A_{ij}\left(B_{ij} r_{ij}^{-p_{ij}} - r_{ij}^{-q_{ij}}\right) \exp\left[(r_{ij} - a_{ij})^{-1}\right]$$

and

$$f_3(i,j,k) = h(r_{ij} r_{ik}, \theta_{jik}) + h(r_{ji}, r_{jk}, \theta_{ijk}) + h(r_{ki}, r_{kj}, \theta_{ikj})$$

with

$$h(r_{ij}, r_{ik}, \theta_{jik}) = \lambda_{jik} \exp\left[\frac{\gamma_{jik}^{ij}}{r_{ij} - a_{jik}^{ij}} + \frac{\gamma_{jik}^{ik}}{r_{ik} - a_{jik}^{ik}}\right] (\cos\theta_{jik} - cos\theta_{jik}^{0})^2.$$

The main difference between the original SW potential and Watanabe's potential is the introduction of the bond-softening function g in front of the two-body pair interactions f_2 function.

The function g is defined as follows

$$g_{ij} = \begin{cases} g(z_i), & i = \text{O and } j = \text{Si} \\ g(z_j), & i = \text{Si and } j = \text{O} \\ 1, & \text{otherwise,} \end{cases}$$

where z_i and z_j are the coordination number of O atoms and with

$$g(z) = m_1[\exp(m_2 - z)/m_3 + 1]^{-1} \exp[m_4 (z - m_5)^2].$$

The coordination number z_i is such that when i is an oxygen atom, it counts all Si atoms surrounding it within the cutoff distance $r < R + D$ given in the definition of f_c:

$$z_i = \sum_{j=\text{Si}} f_c(r_{ij}),$$

where f_c is the cutoff function that determines whether the Si-O bond is formed or not according to the interatomic distance r_{ij}. Its explicit form is

$$f_c(r) = \begin{cases} 1, & r < R - D \\ 1 - \dfrac{r - R + D}{2D} + \dfrac{sin[\pi(r - R + D)/D]}{2\pi}, & R - D \le r < R + D \\ 0, & r \ge R + D. \end{cases}$$

Parameters of the Watanabe's potential are listed in Tables A-2 and A-3.

Table A-2. Parameters for the Two-Body Interactions in the Watanabe's Potential

	Si-Si	Si-O	O-O
A	7.049556277	115.364065913	-12.292427744
B	0.602245584	0.9094442793	0.0
p	4	2.58759	0
q	0	2.39370	2.24432
a	1.8	1.4	1.25

In LAMMPS, the two-body interactions Si-O will come from Si-O-O.

Table A-3. Parameters for the Watanabe's Potential

	Si-Si-Si	Si-O-Si	Si-Si-O	Si-O-O	O-Si-Si
λ	16.404	10.667	10.667	3.1892	2.9572
γ	1.0473	0.25	1.93973	0.3220	0.71773
a	1.8	1.4	1.9	1.65	1.4
cos(θ)	-1/3	-1/3	-1/3	-1/3	-0.615523800000

In LAMMPS, the two-body interactions will come from Si-O-O.

Some comments about Watanabe's potential follow.

- σ and ϵ for Si/SiO_2 material are the same as in the SW potential. They correspond to silicon. $\sigma = 2.0951\dot{A}$ and $\epsilon = 500$ kcal/mol.

- Si-O-O and O-O-O triplets are omitted because O-O bonds are not considered in the definition of the potential. That means that the only nonzero contribution for O-O pairs corresponds to A_{OO} terms in the pair function f_2 corresponding to repulsive terms. The three-body potential is zero for Si-O-O and O-O-O triplets.

- Watanabe's potential is exactly the SW potential if silicon atoms only are present because then $g = 1$. However it should be noted that Watanabe's potential uses different parameters values for λ and γ.

A.2.4 Results

To simulate Si/SiO_2 interfaces, we chose several different SiO_2 structures. Their definitions were taken from [4]. We list them in the following.

The structure of α-quartz is in the hexagonal $P3_221$ space-group symmetry. Its primitive vector can be expressed as

$$A_1 = \frac{1}{2}ae_x - \frac{\sqrt{3}}{2}ae_y,$$

$$A_2 = \frac{1}{2}ae_x - \frac{\sqrt{3}}{2}ae_y,$$

and

$$A_3 = ce_z,$$

where *a* and *c* are the lattice parameters corresponding to a conventional tetragonal unit cell. In each primitive unit cell, there are three atom-triplets of SiO_2 with atomic positions:
Si: $(u, 0, 0)$; $(u, u, 1/3)$; $(0, u, 2/3)$.
O : (x, y, z); $(y - x, -x, z + 1/3)$, $(x - y, -y, -z)$; $(-y, x - y, z + 2/3)$; $(y, x, 2/3 - z)$, $(-x, y - x, 1/3 - z)$ where we took $u = 0.4697$, $x = 0.4135$, $y = 0.2669$, and $z = 0.1191$.

The structure of β-quartz has an overall $P6_222$ space-group symmetry. The corresponding atomic positions for space group $P6_222$ can be written as follows:
Si: $(1/2, 1/2, 1/3)$; $(1/2, 0. 0)$; $(0, 1/2, 2/3)$.
O: $(u, -u, 5/6)$; $(-u-, u, 5/6)$; $(u, 2u, 1/2)$; $(-u, -2u, 1/2)$; $(2u, u, 1/6)$; $(-2u, -u, 1/6)$ with $u = 0.197$.

The structure of α-cristobalite has a tetragonal $P4_12_11$ space-group symmetry, whose corresponding primitive unit cell is

$$r = ae_x + ae_y + ce_z$$

and has the following atomic positions:
Si: $(u, u, 0)$; $(-u, -u, 1/2)$; $(1/2 - u, u + 1/2, 1/4)$; $(u + 1/2, 1/2 - u, 3/4)$;
O: (x, y, z); $(y, x, -z)$; $(-x, -y, z + 1/2)$; $(1/2 - y, x + 1/2, z + 1/4)$; $(y + 1/2, 1/2 - x, z + 3/4)$; $(-y, -x, 1/2 - z)$; $(1/2 - x, y + 1/2, 1/4 - z)$; $(x + 1/2, 1/2 - y, 3/4 - z)$; where $u = .30004$, $x = .23976$, $y = .10324$ and $z = .17844$.

Finally, there is β tridymite, which is the high-temperature and high-symmetry phase of tridymite. It has the $P6_2/mmc$ space-group symmetry, and it has the same primitive vectors as quartz. The atomic positions in the unit cell can be written as follows: Si: $(1/3, 2/3, u)$; $(2/3, 1/3, -u)$; $(2/3, 1/3, -u)$; $(2/3, 1/3, u + 1/2)$; $(1/3, 2/3, 1/2 - u)$;
O: $(1/3, 2/3, u)$; $(2/3, 1/3, 3/4)$; $(1/2, 0, 0)$; $(0, 1/2, 0)$; $(1/2, 1/2, 0)$; $(1/2, 0, 1/2)$; 1$(0, 1/2, 1/2)$; $(1/2, 1/2, 1/2)$ where $u = 0.44$.

Using the method described in previous sections, we were able to compute the Kapitza conductance of an Si/SiO_2 interface where SiO2 is α-quartz as shown in Figure A-8 at 300 K. We chose three different lengths for the Si/SiO2 system. A representation of the Si/SiO2 interface is shown in Figure A-7. We estimated the thermal conductivity to be 3.2 GW/m^2 K. This value is slightly higher than the one found in [6]. Mahajan et al. used amorphous silicon dioxide instead of a perfect SiO_2 structure as considered here and found a thermal conductivity of 1.98 GW/m^2 K.

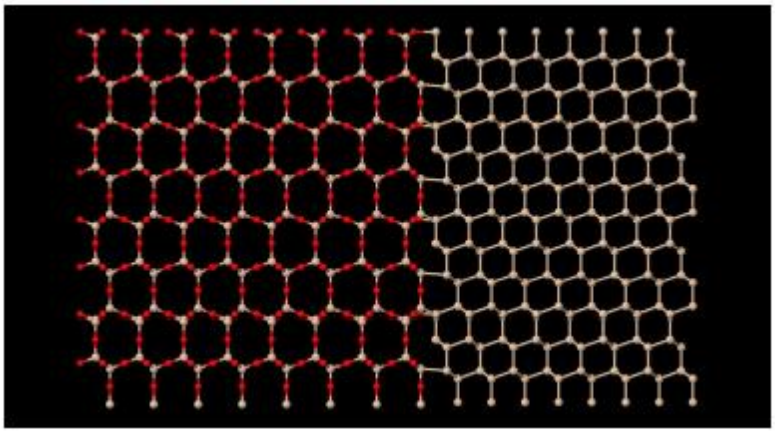

Figure A-7. Si/SiO_2 structure interface chosen for this work.

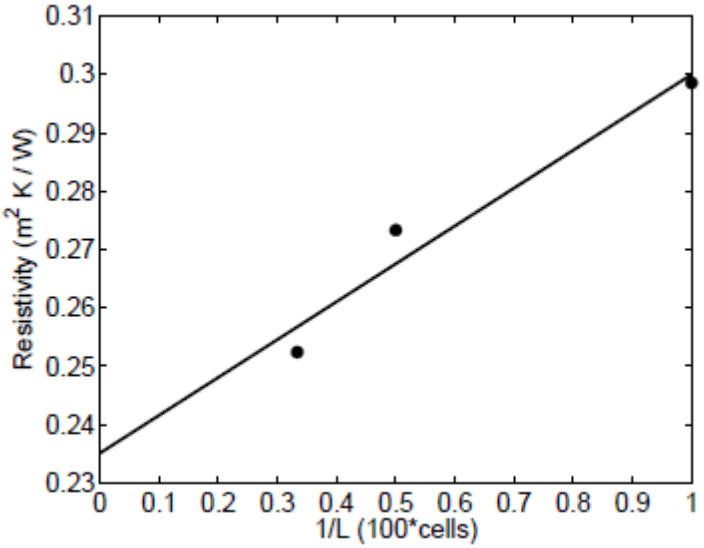

Figure A-8. Kapitza resistance versus system length for α-quartz. The extrapolated value for the thermal conductivity is 3.2 GW/m^2 K at 300 K.

Computation of Forces

The introduction of the g function in the pair body interactions, which is a function of the sum of radius r, complicates the derivative of f_2. Let's call f the original pair potential of SW. It is a function of r_{ij} only, as in

$$f(r_{ij}) = \epsilon A_{ij}\left(B_{ij} r_{ij}^{-p_{ij}} - r_{ij}^{-q_{ij}}\right) \exp\left[(r_{ij} - a_{ij})^{-1}\right].$$

We have

$$E_{pair} = \sum_i \sum_{j,j>i} v_2(i,j) = \sum_i \sum_{j,j>i} f_2\left(\frac{r_{ij}}{\sigma}\right) = \sum_i \sum_{j,j>i} g_{ij} f\left(\frac{r_{ij}}{\sigma}\right).$$

We have to derive

$$E_{pair} = \sum_i \sum_{j,j>i} g_{ij} f\left(\frac{r_{ij}}{\sigma}\right)$$

$$E_{pair} = \sum_i \sum_{j,j>i} g_{ij} f\left(\frac{r_{ij}}{\sigma}\right) 1_{\{i=Si\}} 1_{\{j=Si\}} + \sum_i \sum_{j,j>i} g_{ij} f\left(\frac{r_{ij}}{\sigma}\right) 1_{\{i=Si\}} 1_{\{j=O\}}$$

$$+ \sum_i \sum_{j,j>i} g_{ij} f\left(\frac{r_{ij}}{\sigma}\right) 1_{\{i=O\}} 1_{\{j=Si\}} + \sum_i \sum_{j,j>i} g_{ij} f\left(\frac{r_{ij}}{\sigma}\right) 1_{\{i=O\}} 1_{\{j=O\}}.$$

We replace g by its definition and we get

$$E_{pair} = \sum_i \sum_{j,j>i} f\left(\frac{r_{ij}}{\sigma}\right) 1_{\{i=Si\}} 1_{\{j=Si\}} + \sum_i \sum_{j,j>i} g(j=O) f\left(\frac{r_{ij}}{\sigma}\right) 1_{\{i=Si\}} 1_{\{j=O\}}$$

$$+ \sum_i \sum_{j,j>i} g(i=O) f\left(\frac{r_{ij}}{\sigma}\right) 1_{\{i=O\}} 1_{\{j=Si\}} + \sum_i \sum_{j,j>i} f\left(\frac{r_{ij}}{\sigma}\right) 1_{\{i=O\}} 1_{\{j=O\}}.$$

When $i = j$, we recognize the regular form of the SW potential. We already know the derivative of E_{pair} for this case. Let's look at

$$E_{Si-O} = \sum_{i=Si} \sum_{j=O,j>i} g(j=O) f\left(\frac{r_{ij}}{\sigma}\right) = \sum_{i=Si} \sum_{j=O,j>i} g\left(\sum_{k=Si} f_c\left(\frac{r_{jk}}{\sigma}\right)\right) f\left(\frac{r_{ij}}{\sigma}\right)$$

and

$$E_{O-Si} = \sum_{i=O} \sum_{j=Si,j>i} g(i=O) f\left(\frac{r_{ij}}{\sigma}\right) = \sum_{i=O} \sum_{j=Si,j>i} g\left(\sum_{k=Si} f_c\left(\frac{r_{ik}}{\sigma}\right)\right) f\left(\frac{r_{ij}}{\sigma}\right).$$

In ESi−O, g does not depend on i anymore and can be put outside of the sum on i. Let's now derive both expressions.

Note that

$$\frac{dr_{ij}}{dx_i} = \frac{x_i - x_j}{r_{ij}}$$

and

$$\frac{dr_{ij}}{dx_j} = \frac{x_j - x_i}{r_{ji}}.$$

The first expression is

$$\frac{dE_{Si-O}}{dx_i} = \sum_{i=Si} \sum_{j=O, j>i} \left[\frac{dg\left(\sum_{k=Si} f_c\left(\frac{r_{jk}}{\sigma}\right)\right)}{dx_i} \right] f\left(\frac{r_{ij}}{\sigma}\right) + g(z_j) \frac{df\left(\frac{r_{ij}}{\sigma}\right)}{dx_i}$$

or

$$\frac{dE_{Si-O}}{dx_i} = \sum_{i=Si} \sum_{j=O, j>i} \left[\frac{dg}{dz_j}(z_j) \left(\sum_{k=Si} \frac{df_c\left(\frac{r_{jk}}{\sigma}\right)}{dx_i} \right) f\left(\frac{r_{ij}}{\sigma}\right) + g(z_j) \frac{df\left(\frac{r_{ij}}{\sigma}\right)}{dr_{ij}} \frac{dr_{ij}}{dx_i} \right].$$

But we have that $i = Si$ and

$$\sum_{k=Si} \frac{df_c\left(\frac{r_{jk}}{\sigma}\right)}{dx_i} = \frac{df_c\left(\frac{r_{ji}}{\sigma}\right)}{dx_i}$$

that is the sum is zero if $i \neq k$. So the derivative becomes

$$\frac{dE_{Si-O}}{dx_i} = \sum_{i=Si} \sum_{j=O, j>i} \left[\frac{dg}{dz_j}(z_j) \frac{df_c\left(\frac{r_{ji}}{\sigma}\right)}{dx_i} f\left(\frac{r_{ij}}{\sigma}\right) + g(z_j) \frac{df\left(\frac{r_{ij}}{\sigma}\right)}{dr_{ij}} \frac{dr_{ij}}{dx_i} \right]$$

or

$$\frac{dE_{Si-O}}{dx_i} = \sum_{i=Si} \sum_{j=O, j>i} \left[\frac{dg}{dz_j}(z_j) \frac{1}{\sigma} \frac{df_c}{dr_{ij}}\left(\frac{r_{ji}}{\sigma}\right) \frac{dr_{ji}}{dx_i} f\left(\frac{r_{ij}}{\sigma}\right) + g(z_j) \frac{1}{\sigma} \frac{df}{dr_{ij}}\left(\frac{r_{ij}}{\sigma}\right) \frac{dr_{ij}}{dx_i} \right]$$

Finally, we have

$$\frac{dE_{Si-O}}{dx_i} = \sum_{i=Si} \sum_{j=O, j>i} \left[\frac{dg}{dz_j}(z_j) \frac{df_c}{dr_{ji}}\left(\frac{r_{ji}}{\sigma}\right) f\left(\frac{r_{ij}}{\sigma}\right) - g(z_j) \frac{df}{dr_{ij}}\left(\frac{r_{ij}}{\sigma}\right) \right] \frac{x_j - x_i}{r_{ij}\sigma}.$$

Note that one term is positive and the other negative.

The second expression is

$$\frac{dE_{O-Si}}{dx_i} = \sum_{i=O} \sum_{j=Si, j>i} \left[\frac{dg\left(\sum_{k=Si} f_c\left(\frac{r_{ik}}{\sigma}\right)\right)}{dx_i} \right] f\left(\frac{r_{ij}}{\sigma}\right) + g(z_i) \frac{df\left(\frac{r_{ij}}{\sigma}\right)}{dx_i}$$

or

$$\frac{dE_{O-Si}}{dx_i} = \sum_{i=O} \sum_{j=Si, j>i} \left[\frac{dg(z_i)}{dz} \frac{d\left(\sum_{k=Si} f_c\left(\frac{r_{ik}}{\sigma}\right)\right)}{dx_i} \right] f\left(\frac{r_{ij}}{\sigma}\right) + g(z_i) \frac{df\left(\frac{r_{ij}}{\sigma}\right)}{dx_i}$$

or again

$$\frac{dE_{O-Si}}{dx_i} = \sum_{i=O} \sum_{j=Si, j>i} \left[\frac{dg(z_i)}{dz} \left(\sum_{k=Si} \frac{1}{\sigma} \frac{df_c}{dr_{ik}}\left(\frac{r_{ik}}{\sigma}\right) \frac{dr_{ik}}{dx_i} \right) \right] f\left(\frac{r_{ij}}{\sigma}\right) + g(z_i) \frac{1}{\sigma} \frac{df}{dr_{ij}}\left(\frac{r_{ij}}{\sigma}\right) \frac{dr_{ij}}{dx_i}.$$

Finally, we have

$$\frac{dE_{O-Si}}{dx_i} = \sum_{i=O} \sum_{j=Si, j>i} \left[-\frac{dg(z_i)}{dz} \left(\sum_{k=Si} \frac{df_c}{dr_{ik}}\left(\frac{r_{ik}}{\sigma}\right) \frac{(x_k - x_i)}{r_{ik}\sigma} \right) f\left(\frac{r_{ij}}{\sigma}\right) + g(z_i) \frac{df}{dr_{ij}}\left(\frac{r_{ij}}{\sigma}\right) \frac{(x_j - x_i)}{r_{ij}\sigma} \right].$$

Similarly,

$$\frac{dE_{Si-O}}{dx_j} = \sum_{i=Si} \sum_{j=O, j>i} \left[-\frac{dg(z_j)}{dx_j} f\left(\frac{r_{ij}}{\sigma}\right) + g(z_j) \frac{df\left(\frac{r_{ij}}{\sigma}\right)}{dx_j} \right]$$

gives

$$\frac{dE_{Si-O}}{dx_j} = \sum_{i=Si} \sum_{j=O, j>i} \left[\frac{dg(z_j)}{dz} \left(\sum_{k=Si} \frac{df_c\left(\frac{r_{ik}}{\sigma}\right)}{dr_{jk}} \frac{dr_{jk}}{dx_j} \right) f\left(\frac{r_{ij}}{\sigma}\right) + g(z_j) \frac{df\left(\frac{r_{ij}}{\sigma}\right)}{dr_{ij}} \frac{dr_{ij}}{dx_j} \right]$$

or finally,

$$\frac{dE_{Si-O}}{dx_j} = \sum_{i=Si} \sum_{j=O, j>i} \left[-\frac{dg(z_j)}{dz} \left(\sum_{k=Si} \frac{df_c}{dr_{jk}}\left(\frac{r_{jk}}{\sigma}\right) \frac{(x_k - x_j)}{r_{jk}\sigma} \right) f\left(\frac{r_{ij}}{\sigma}\right) + g(z_j) \frac{df}{dr_{ij}}\left(\frac{r_{ij}}{\sigma}\right) \frac{(x_j - x_i)}{r_{ij}\sigma} \right]$$

and also

$$\frac{dE_{O-Si}}{dx_j} = \sum_{i=O} \sum_{j=Si, j>i} \left[\frac{dg\left(\sum_{k=Si} f_c\left(\frac{r_{jk}}{\sigma}\right)\right)}{dx_j} f\left(\frac{r_{ij}}{\sigma}\right) + g(z_i) \frac{df\left(\frac{r_{ij}}{\sigma}\right)}{dx_j} \right]$$

gives

$$\frac{dE_{O-Si}}{dx_j} = \sum_{i=O} \sum_{j=Si, j>i} \left[\frac{dg(z_i)}{dz} \left(\sum_{k=Si} \frac{df_c\left(\frac{r_{ik}}{\sigma}\right)}{dx_j} \right) f\left(\frac{r_{ij}}{\sigma}\right) + g(z_i) \frac{df\left(\frac{r_{ij}}{\sigma}\right)}{dx_j} \right].$$

But we have that $j = Si$ and

$$\sum_{k=Si} \frac{df_c\left(\frac{r_{ik}}{\sigma}\right)}{dx_j} = \frac{df_c\left(\frac{r_{ij}}{\sigma}\right)}{dx_j}$$

that is the sum is zero if $j \neq k$j . So the derivative becomes

$$\frac{dE_{O-Si}}{dx_j} = \sum_{i=O} \sum_{j=Si, j>i} \left[\frac{dg(z_i)}{dz} \frac{df_c\left(\frac{r_{ij}}{\sigma}\right)}{dr_{ij}} \frac{dr_{ij}}{dx_j} f\left(\frac{r_{ij}}{\sigma}\right) + g(z_i) \frac{df\left(\frac{r_{ij}}{\sigma}\right)}{dr_{ij}} \frac{dr_{ij}}{dx_j} \right]$$

and finally,

$$\frac{dE_{O-Si}}{dx_j} = \sum_{i=O} \sum_{j=Si, j>i} \left[\frac{dg(z_i)}{dz} \frac{df_c}{dr_{ij}}\left(\frac{r_{ij}}{\sigma}\right) f\left(\frac{r_{ij}}{\sigma}\right) + g(z_i) \frac{df}{dr_{ij}}\left(\frac{r_{ij}}{\sigma}\right) \right] \frac{(x_j - x_i)}{r_{ij}\sigma}.$$

In conclusion, we have

$$\frac{dE_{Si-O}}{dx_i} = \sum_{i=Si} \sum_{j=O, j>i} \left[\frac{dg}{dz_j} \frac{-1}{r_{ji}} \frac{df_c\left(\frac{r_{ji}}{\sigma}\right)}{dr_{ji}} f + g(z_j) \frac{-1}{r_{ij}} \frac{df}{dr_{ij}} \right] (x_j - x_i)$$

$$\frac{dE_{Si-O}}{dx_j} = \sum_{i=Si} \sum_{j=O, j>i} \left[\frac{dg}{dz_j} \left(\sum_{k=Si} \frac{-1}{r_{jk}} \frac{df_c\left(\frac{r_{jk}}{\sigma}\right)}{dr_{jk}} (x_k - x_j) \right) f - g(z_j) \frac{-1}{r_{ij}} \frac{df}{dr_{ij}} (x_j - x_i) \right]$$

$$\frac{dE_{O-Si}}{dx_i} = \sum_{i=O} \sum_{j=Si, j>i} \left[\frac{dg}{dz_i} \left(\sum_{k=Si} \frac{-1}{r_{ik}} \frac{df_c\left(\frac{r_{ik}}{\sigma}\right)}{dr_{ik}} \frac{(x_k - x_i)}{r_{ik}\sigma} \right) f + g(z_i) \frac{-1}{r_{ij}} \frac{df\left(\frac{r_{ij}}{\sigma}\right)}{dr_{ij}} (x_j - x_i) \right]$$

$$\frac{dE_{O-Si}}{dx_j} = \sum_{i=O} \sum_{j=Si, j>i} \left[\frac{dg}{dz_i} \frac{-1}{r_{ij}} \frac{df_c\left(\frac{r_{ij}}{\sigma}\right)}{dr_{ij}} f + g(z_i) \frac{-1}{r_{ij}} \frac{df\left(\frac{r_{ij}}{\sigma}\right)}{dr_{ij}} \right] (x_j - x_i).$$

A.3 References

[1] P. L. Kapitza. "The study of heat transfer in helium II," *J. Phys. USSR*, 4: 181 (1941).

[2] J. A. Katerberg, C. L. Reynolds Jr., and A. C. Anderson. "Calculations of the thermal boundary resistance," *Phys. Rev. B* 16(2): 673–679 (1977).

[3] C. Kimmer, S. Aubry, A. Skye, and P. K. Schelling. "Scattering of phonons from a high-energy grain boundary in silicon: Dependence on angle of incidence," *Phys. Rev. B* 75: 144105 (2007).

[4] C. L. Kuo and P. Clancy. –Development of atomistic meam potentials for the silicon-oxygen-gold ternary system," *Modelling and simulation in materials science and engineering* 13(8):1309–1329 (2005).

[5] W. A. Little. –The transport of heat between dissimilar solids at low temperatures, *Can. J. Phys*. 37: 334 (1959).

[6] S. S. Mahajan, G. Subbarayan, and B. G. Sammakia. –Estimating kapitza resistance between si-sio2 interface using molecular dynamics simulations," *2008 11th Intersociety Conference on Thermal and Thermomechanical Phenomena in Electronic Systems (ITHERM '08)*, pages 1055–62 (2008).

[7] S. Pettersson and G. D. Mahan. –Theory of the thermal boundary resistance between dissimilar lattices," *Phys. Rev. B* 42: 7386 (1990).

[8] P. K. Schelling, S. R. Phillpot, and P. Keblinski. –Comparison of atomic-level simulation methods for computing thermal conductivity," *Phys. Rev. B* 65: 144306 (2002).

[9] P. K. Schelling, S. R. Phillpot, and P. Keblinski. –Phonon wave-packet dynamics at semiconductor interfaces by molecular-dynamics simulation," *Appl. Phys. Lett*. 80: 2484 (2002).

[10] P. K. Schelling, S. R. Phillpot, and P. Keblinski. –Kapitza conductance and phonon scattering at grain boundaries by simulation," *J. Appl. Phys*. 95: 6082 (2004).

[11] S. Simons. –Thermal contact resistance between insulators," *J. Phys. C* 7: 4048 (1974).

[12] F. H. Stillinger and T. A. Weber. –Computer simulation of local order in condensed phases of silicon," *Phys. Rev. B* 31(8): 5262 (1985).

[13] E. T. Swartz and R. O. Pohl. –Thermal-boundary resistance," *Rev. Mod. Phys*. 61: 605 (1989).

[14] Y. Tu and J. Tersoff. –Structure and energetics of the Si- SiO2 interface," *Phys. Rev. Lett*. 84(19): 4393–4396 (2000).

[15] T. Watanabe, H. Fujiwara, H. Noguchi, T. Hoshino, and I. Ohdomari. –Novel interatomic potential energy function for si, o mixed systems," *Jpn. J. Appl. Phys*. 38: L366 (1999).

[16] T. Watanabe, B. Ni, P. K. Schelling, P. Keblinski, and S. R. Phillpot. –Thermal conductance across grain boundaries in diamond from molecular dynamics simulation," *J. Appl. Phys*. 102: 063503 (2007).

[17] D. A. Young and H. J. Maris. –Lattice-dynamics calculation of the Kapitza resistance between fcc lattices," *Phys. Rev. B* 40: 3685 (1989).

[18] X. W. Zhou, S. Aubry, R. E. Jones, A. Greenstein, and P. Schelling. –Towards more accurate molecular dynamics calculation of thermal conductivity: Case study of GaN bulk crystals," *Phys. Rev. B* 79: 115201–115218 (2009).

Appendix B. Phonon Transport Across Interfaces: Predicted Thermal Conductivity of Twisted Silicon Stack

This appendix describes the model that was created for the twist boundary stack experiment in the study of phonon transport across interfaces. The model calculates the predicted thermal conductivity of a stack as a function of the number of layers, temperature, and layer thickness. We used the model to determine the measurement system requirements and found that our proposed stack design of 10 layers could not produce a thermal conductivity sufficiently different from the baseline (untwisted) case to be discerned by the available measurement techniques.

B.1 General Description

Consider a stack of slabs with grain-boundary-like interfaces as a group of resistors connected in series. There are two types of resistors in this system: those associated with the bulk thermal conductivity in the slabs and those associated with the disorder at the interfaces.

The resistance of each slab is

$$R_{slab} = t/kwL,$$

where t is the layer thickness, k is the thermal conductivity, w is the layer width, and L is the layer length.

The resistance of the interfaces is

$$R_{interface} = 1/\sigma_k wL,$$

where σ_k is the Kapitza conductance.

The resistance of a stack with n interfaces is thus

$$R = (n+1)R_{slab} + nR_{interface}$$

$$= ((n+1)\,t/k + n/\sigma_k)/wL.$$

The measured thermal conductivity will be

$$k_{meas} = (n+1)t/(RWL)$$

$$= (n+1)t\sigma_k k/[(n+1)t\sigma_k + nk].$$

B.2 Sanity Checks

If the Kapitza conductance goes to infinity, this expression reduces to $k_{meas} = k$. That is good. However, if the slab conductance goes to infinity, the expression reduces to

$$k_{meas} = (n+1)t\sigma_k/n.$$

The above equation looks a bit odd but makes sense upon further inspection. The $(n+1)t$ term is simply the thickness of the stack. If you adjust t to hold it constant as the number of interfaces increases, then the measured thermal conductivity declines as the number of interfaces increases, as expected. The thermal conductivity tends to the thickness of a slab times the Kapitza conductance for an infinite number of interfaces. This limit also makes sense as the Kapitza conductance of an interface would be sort of ~~–~~averaged" over its adjacent slab. With an infinite number of slabs, the fact that there are actually $n+1$ slabs becomes insignificant.

B.3 Results

At room temperature, the thermal conductivity of single-crystal silicon is roughly 150 W/m K. The Kapitza conductance for the Σ29 interface at this temperature has been reported as 0.5245 GW/m^2 K at 300 K [1] (i.e., Fig. 8 in that reference). We therefore have for ten 100 μm slabs the following:

$$k_{meas} = 149.61 \text{ W/m K},$$

which is such a small difference that it effectively renders the effect of the twist immeasurable using standard techniques.

To look at the effect of various parameters, we can set the parameters at the nominal conditions and then vary one parameter. In our first calculation, we hold the thickness constant and change the number of layers. This calculation yields the result shown in Figure B-1.

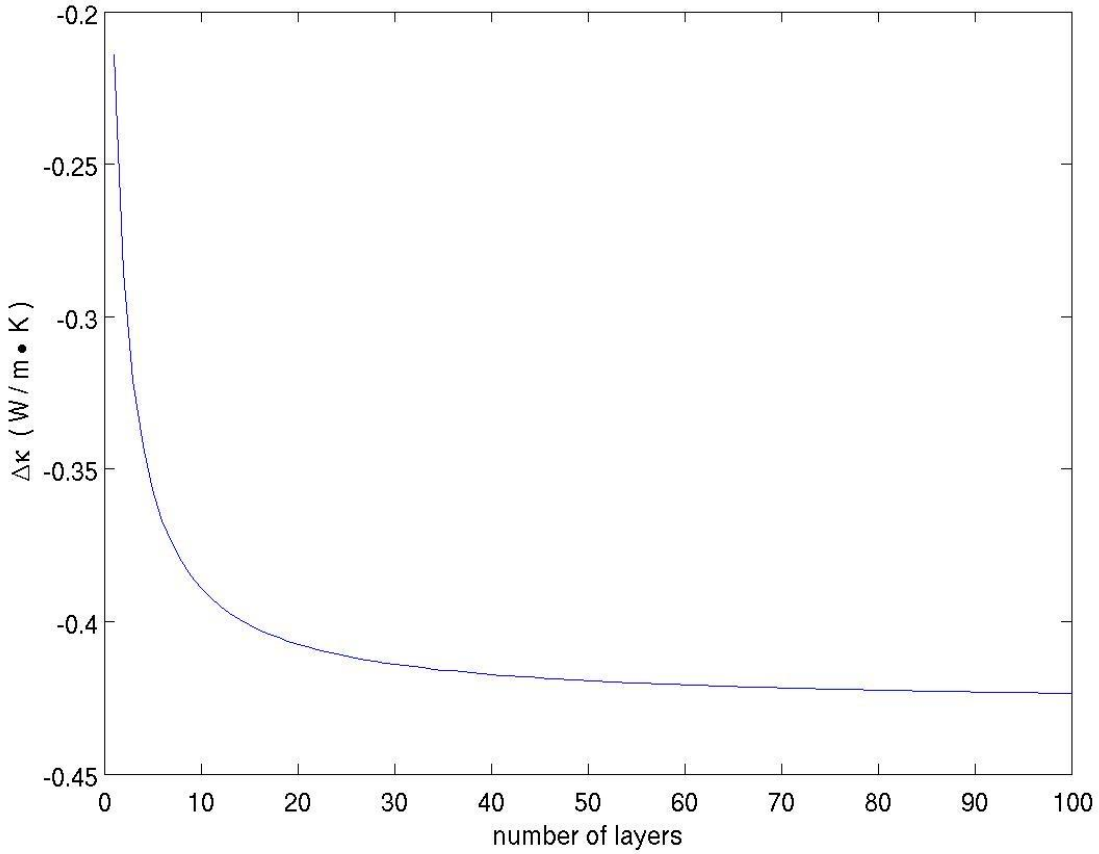

Figure B-1. Difference in measured thermal conductivity between twisted stack and bulk material as a function of number of layers in stack.

We can conclude that the number of layers has a rather weak effect on the measured difference in thermal conductivity, and we are reasonably close to the asymptote at 10 layers. (Note that all the terms in the equation contain either n or $n + 1$, so this behavior is expected.)

If we return the number of layers to 10, the nominal value, and instead vary the thickness, we find the result shown in Figure B-2.

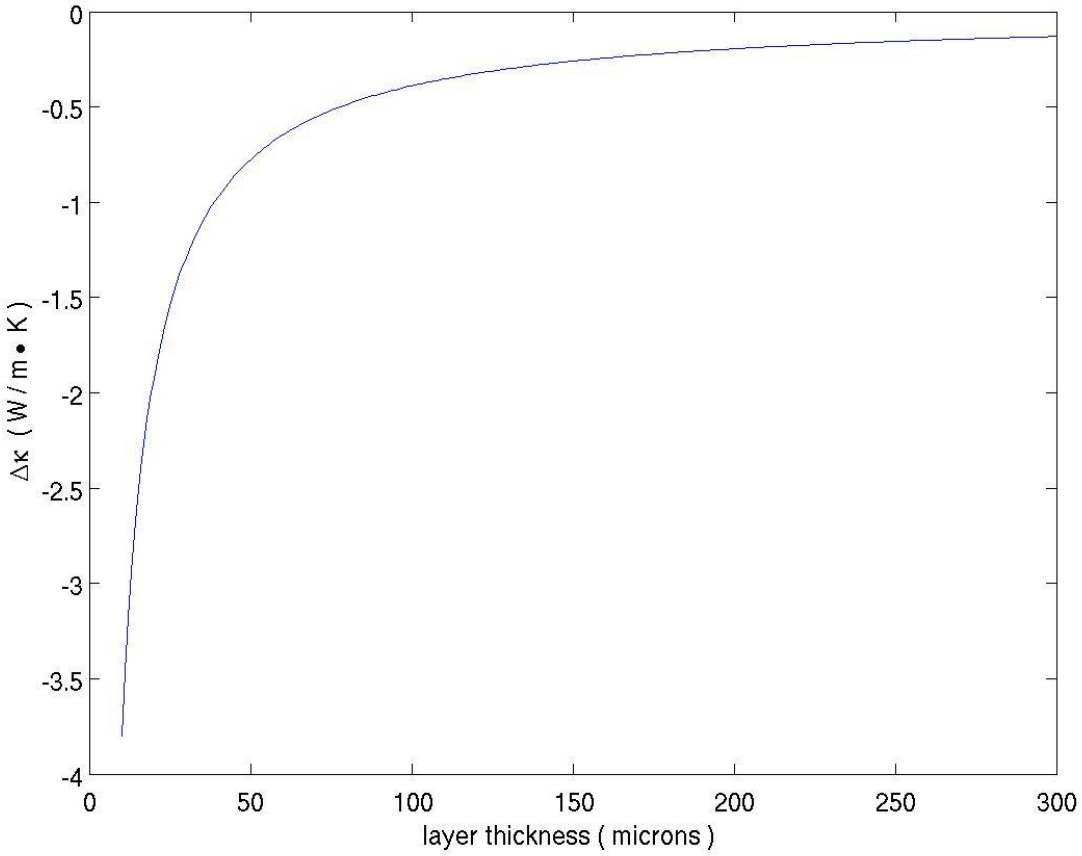

Figure B-2. Difference in measured thermal conductivity between twisted stack and bulk material as a function of layer thickness for 10 layers.

It appears from Figure B-2 that layer thickness has a stronger effect on the total difference in measured thermal conductivity than does the number of layers. By halving the layer thickness, we could double the observed difference. If we can handle even thinner layers, we can do much better because the curve becomes very steep below 50 μm.

Now, if we vary the temperature and use nominal values for layer thickness and the number of layers, we find the result shown in Figure B-3.

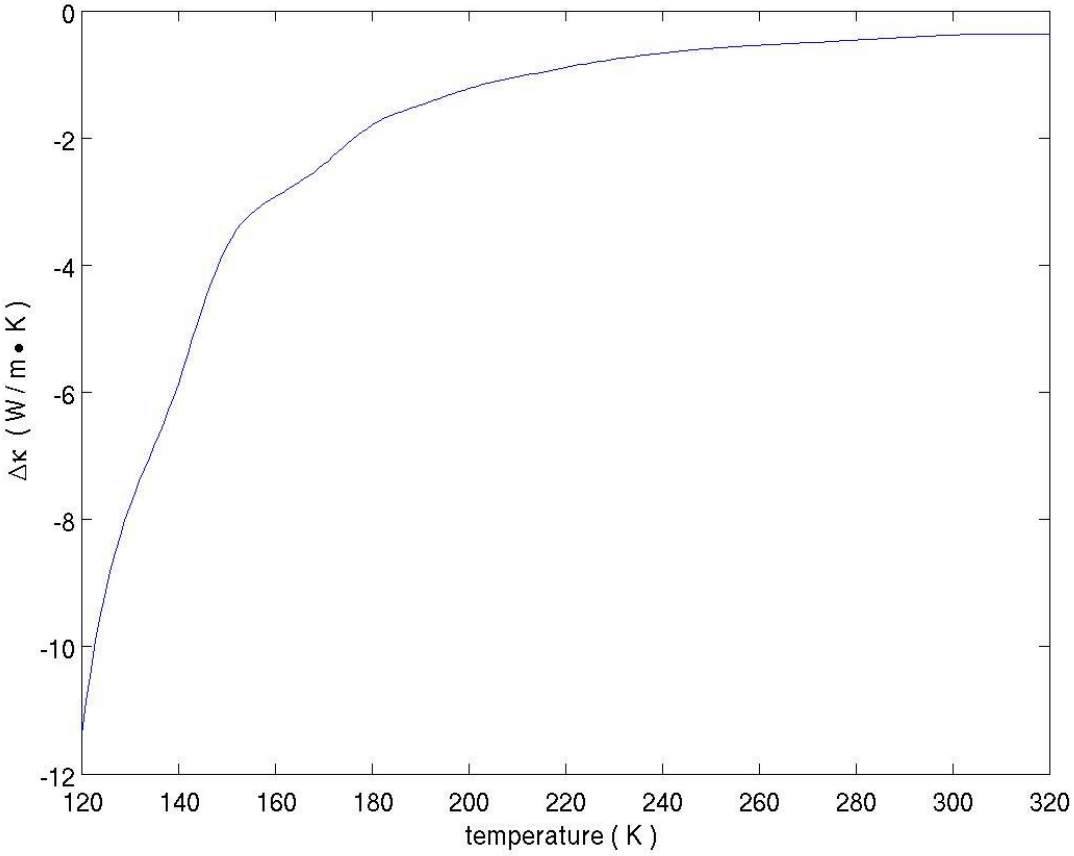

Figure B-3. Difference in measured thermal conductivity between twisted stack and bulk material as a function of temperature for 10 layers of 100 μm thickness each.

Although the influence of changing temperature in Figure B-3 looks promising, note that the thermal conductivity increases quickly as the temperature decreases, a condition that has been plotted as a pure difference. However, if the experimental error is a fraction of the measured quantity, our situation looks more that shown in Figure B-4.

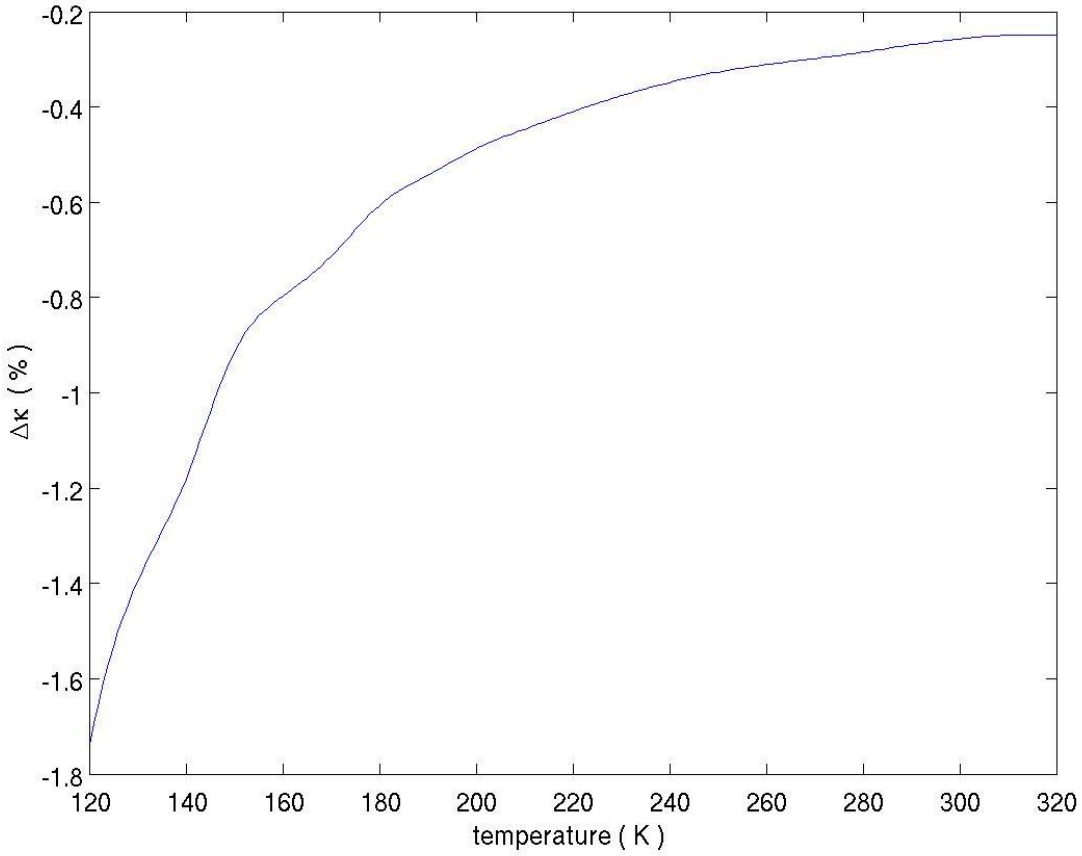

Figure B-4. Difference in measured thermal conductivity between twisted stack and bulk material as a percentage of the bulk value.

Figure B-4 indicates that the differences that we seek to measure are much smaller than the experimental error and will therefore be impossible to discern. It also looks like we may want to consider thinner layers and lower temperatures.

B.4 References

[1] C. Kimmer, S. Aubry, A. Skye, and P. K. Schelling. ―Scattering of phonons from a high-energy grain boundary in silicon: Dependence on angle of incidence,‖ *Phys. Rev. B* 75(14): 144105 (2007).

Appendix C. Phonon Transport Across Interfaces: Picosecond Measurements of Kapitza Resistance of the Interfaces (Published Paper #1)

This appendix contains a published paper. The only changes made from the published work was the reformatting of paragraphs and the resizing of figures and captions to fit within the general style of this document. The original was a two-column format.

Imaging carrier and phonon transport in Si using ultrashort optical pulses

D. H. Hurley[a1], O. B. Wright[b], O. Matsuda[b], Brian E. McCandless[c], Subhash Shinde[d]

[a]Idaho National Laboratory, P.O. Box 1625, Idaho Falls, Idaho 83415-2209, USA
[b]Department of Applied Physics, Hokkaido University, Sapporo 060-8628, Japan
[c]Institute of Energy Conversion, University of Delaware, Newark, DE 19716 USA
[d]Sandia National Laboratory, P.O. Box 5800, Albuquerque, NM 87185-0603, USA

ABSTRACT

A series of experiments have been conducted that microscopically image thermal diffusion and surface acoustic phonon propagation within a single crystallite of a polycrystalline Si sample. The experimental approach employs ultrashort optical pulses to generate an electron-hole plasma and a second probe pulse is used to image the evolution of the plasma. By decomposing the signal into a component that varies with delay time and a steady state component that varies with pump modulation frequency, the respective influence of carrier recombination and thermal diffusion are identified. Additionally, the coherent surface acoustic phonon component to the signal is imaged using a Sagnac interferometer to monitor optical phase.

Keywords: Thermal transport, phonon, electron transport, recombination, surface acoustic wave, grain boundary

1. INTRODUCTION

Studies of ultrafast optical excitation and propagation of phonon pulses hold the potential to unlock fundamental carrier and phonon transport properties of solar electric and optoelectronic materials. This approach, termed picosecond acoustics[1], is a valuable tool to study carrier[2] and phonon transport[1], since phonon generation and propagation are indicative of carrier relaxation[3], carrier diffusion[4], carrier-phonon interaction[5] and phonon diffusion[6]. In the present study ultrashort optical pulses are used to generate an electron-hole plasma in a Si polycrystal and a second probe pulse is used to microscopically image evolution of the plasma and heat diffusion

[1] Email: david.hurley@inl.gov

within a single crystallite. Additionally, the coherent surface acoustic phonon component to the signal is imaged using a Sagnac interferometer to monitor optical phase.

The sample is a Boron doped (p-type) Si polycrystal with a doping concentration of 2x1016/cm3. The sample surface was mechanically polished without subsequent surface passivation resulting in a large density of surface defects. An electron backscatter micrograph of the sample is shown in the inset of Fig. 1. This micrograph gives the crystallite orientation in false color. The region of interest, which is removed from any grain boundaries, is denoted by the dashed square in the inset. The orientation of this crystallite is specified by a crystal plane perpendicular to the sample normal (i,j,k)=(6,7,6) and a crystal direction parallel to the laboratory y axis [u,v,w]=[-7,-12,21]. The present investigation is to serve as a baseline study from which to compare future studies that investigate the influence of boundaries (e.g. grain boundaries and bicrystal interfaces) on phonon transport.

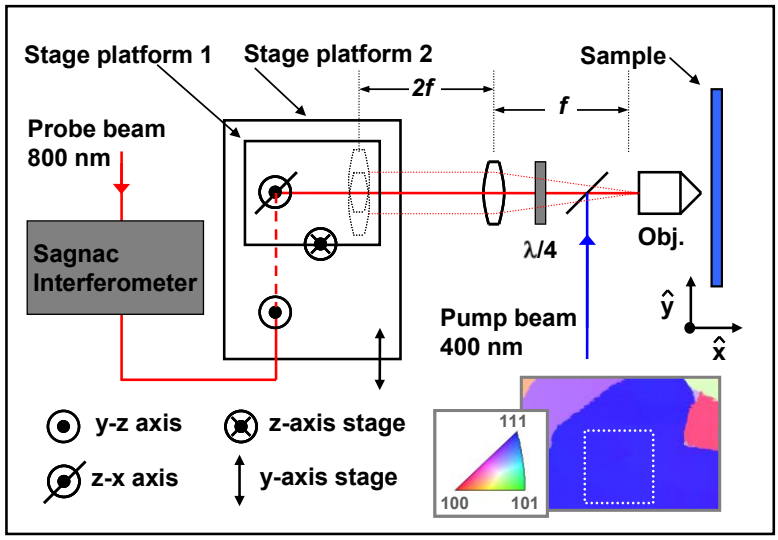

Fig. 1. Experimental setup. A single probe or two interferometric beams can be used. The probe beam is scanned relative to the pump beam at the focal point of the microscope objective by using the translation stage telescope combination.

1.1 Experimental setup

The experimental setup used for imaging changes in reflectivity and optical phase is shown in Fig. 1. It is similar to the setup presented by Tachizaki et al.7 and involves translation of a probe beam relative to a fixed pump beam. The experimental apparatus can employ either a single probe pulse for monitoring changes in probe reflectivity or two interferometric probe pulses for monitoring changes in optical phase and reflectivity. The probe is then sent through a telescope and focused onto the sample using a microscope objective. Both lenses of the telescope have a 100 mm focal length. The first lens is attached to a stage system that allows the lens and the probe beam to be translated in the y-z plane (the probe beam propagation vector remains collinear with the lens axis). The second lens serves to converts the y-z motion of the beam into a change in entrance angle into the objective. Since the objective is placed at the focal

point of the second lens, the entrance angle can be changed without translation in the y-z plane. The pump beam is guided along the optical axis of the objective using a dichroic beam splitter place after the telescope. This system provides a convenient means to scan the probe beam relative to the pump beam for situations that allow for only single-sided access.

1.2 Results

The first experiment involves imaging changes in probe reflectivity for different pump probe delay times. The pump was modulated at 100 kHz to aid in lock-in detection. The pump (λ=400nm, pulse energy=0.026nJ) and probe (λ= 800 m, pulse energy=0.013nJ) are derived from a Ti:Sapphire laser with a pulse duration ~ 1 ps. The series of images in Fig. 2 gives the lock-in amplitude (top) and lock-in phase (bottom) of the change in reflectivity at 3 delays times: t=0ps, t=50ps and t=100 ps.

To better understand the evolution of these images, it is helpful to decompose the signal into two components. The first component is broad band and varies with delay time (transient). The second component is narrow band and varies with pump modulation frequency (diffusion wave). Both components are driven by the diffusion of heat and photoexcited carriers. Initially (t=0ps and t=50 ps) the transient components to the signal are dominant. To illustrate this point consider the lock-in phase signal at these early times. There is little lateral variation in the phase signal for an area that encompasses the excitation region. Initially, the primary gradient in temperature and carrier density is in a direction perpendicular to the surface (pump skin depth=82 nm). Thus any lock-in phase variation of the transient signal would be in a direction perpendicular to the surface. Moreover, the reflectivity change of the probe is a phase average response over a distance equal to approximately one probe skin depth (10 μm) which is considerably larger than the thermal diffusion length $(D_t t)^{1/2}$ and the plasma diffusion length $(D_e t)^{1/2}$ at these early times (D_t is the thermal diffusivity, D_e is the ambipolar diffusivity and t is the pump delay time).

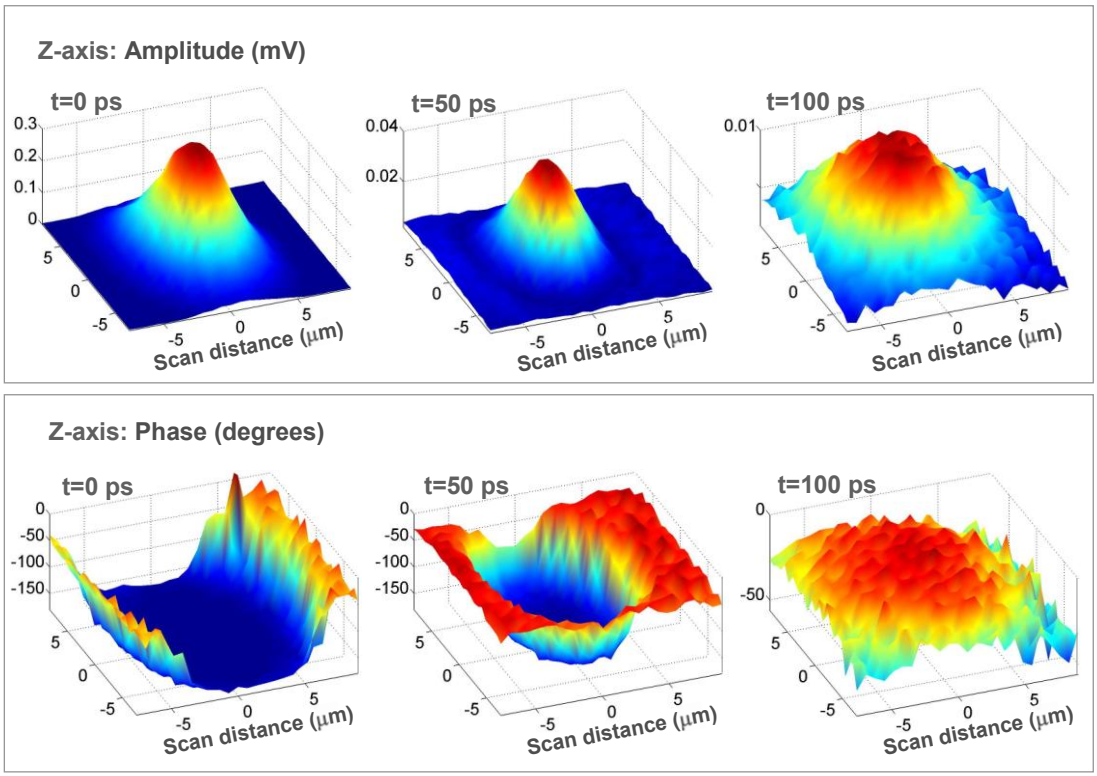

Fig. 2. Images of the amplitude and phase of the probe reflectivity change as a function of delay time. At early times the transient component that varies with delay time is dominant while at large delay times the steady state diffusion wave component is dominant.

The lock-in amplitude and phase images at 100 ps show the characteristics of a diffusion wave. In this case the lock-in phase and amplitude are associated with the amplitude and phase lag of the diffusion wave. Unlike the previous phase signals, the phase lag linearly decreases with increasing distance from the source (a constant was added to all of the phase data so as to give a maximum value of zero at t=100ps). Moreover, the full width at half maximum (FWHM) of the amplitude signal at 100 ps is considerably larger than the FWHM of the previous amplitude signals. In Fig. 3a, the FWHM of the central region of the amplitude signal as a function of delay time is shown. The FWHM continues to decrease up to approximately 80 ps. After this time the FWHM suddenly jumps up to a value of approximately 10 μm and appears to remain constant with increasing delay. Continuing to accurately map the FWHM with increasing delay raises concern regarding slight defocusing of the laser spot due to beam divergence. This issue is conveniently circumvented by looking at t=-10 ps which is equivalent to t = 13.1 ns (the inverse of the laser repetition frequency). This enables a large temporal scan without a large spatial scan. A comparison between the normalized amplitude profile at t = 0 ps and t = 13.1 ns is shown in Fig. 3b. The FWHM at t = 13.1 ns is 10.7 μm which compares closely with the FWHM values after a delay of 90 ps. Why the FWHM steadily decreases[4] at early times can be understood by considering the addition of two Gaussian profiles: one representing the transient component and one representing the steady state diffusion wave component. The lock-in phase data presented in Fig. 2 shows that these two components are ~180 degrees out of phase. Thus the functional form of the amplitude profile for z=0 is approximated by the following:

$$\frac{\Delta R}{R} = \left| A \ \exp\left(\frac{-y^2}{a_t^2 / 4\ln(2)}\right) - \exp\left(\frac{-y^2}{a_s^2 / 4\ln(2)}\right) \right|$$

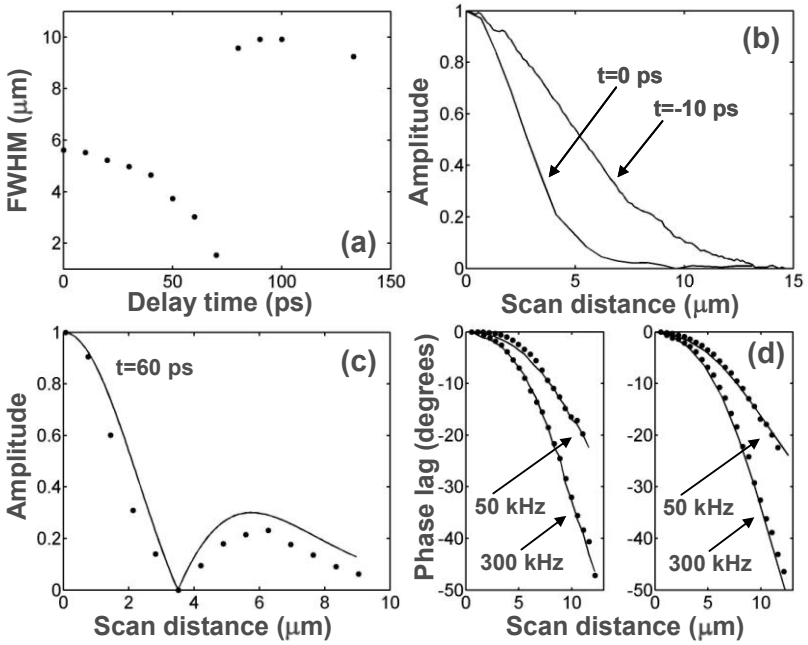

Fig. 3. Examination of the diffusion wave component. Fig. 3a gives the FWHM of the amplitude versus delay time. Fig. 3b gives the amplitude profile for two different delay times. Fig. 3c compares the experimentally measured amplitude profile (dots) to a simulated profile (solid). Fig. 3d (left) compares the steady state phase profile for the pristine sample (dots) and the sample coated with a 30 nm Al film (solid). Fig. 3d (right) compares the predicted phase profile (solid) to the experimentally measured profile for the pristine sample (dots).

where a_t and a_s are the FWHM corresponding to the transient and diffusion wave components and A represents the relative magnitude of the these two terms. (A more accurate representation of the combined amplitude response would consider the lateral variation in both the amplitude and phase of the transient and steady state components. Furthermore, while the amplitude variation of the transient component closely follows the Gaussian spatial distribution of the laser spot, the amplitude of the steady state diffusion component is only approximated using a Gaussian distribution.) At t=0 ps the FWHM is related to a convolution between the probe and pump profiles and serves as an upper limit to the FWHM of the pump beam profile. By measuring a_t (5.8 μm) and a_s (10 μm) for short and long delay times, the expression given above can be fitted to the profile for any given delay using A as a fitting parameter. The results of this procedure for a delay of 60 ps are shown in Fig. 3c. The best fit was obtained for A=2.0 and a sum square error of 0.31. Note that the FWHM of the central region is smaller than the FWHM at t=0 ps. This clearly shows the interference between the transient and diffusion wave components.

This analysis helps explain the physical mechanism responsible for the sudden transition to steady state behavior. The initial decrease in the transient component is due to the evolution of the electron-hole plasma and diffusion of heat. However, considerable insight can be gained by considering only the electron hole plasma. The change in probe reflectivity associated with the expanding electron-hole plasma is proportional to the change in the density of photoexcited electrons.[8] At t=100 ps, the electron density is approximately four times smaller than the initial density (diffusion length at t = 100 ps is ~ 200 nm and the corresponding volume associated with the electron-hole plasma has increased over the initial volume by a factor of approximately four). However, from Fig. 2, the maximum change in the amplitude of the probe reflectivity at 100 ps is approximate 30 times smaller than the contribution at t=0. Thus, diffusion of the electron-hole plasma alone can not account for the dominance of the steady state component at t >100ps. Recombination of the photoexcited carriers on this time scale provides an alternative explanation. The Auger recombination pathway can be neglected since the recombination time for the range of carrier concentrations used extends from 2 ns to 200 ns. The range in recombination time (τ=1/CN^2, C=5x10^{-31} cm^6/s) is estimated using the maximum carrier density range (3x10^{18}/cm^3 - 3x10^{19}/cm^3).[9] Surface recombination associated with defect sites[10,11] is another possible pathway. The density of surface defects is expected to be high for the unpassivated sample under investigation. Studies have shown that the recombination time in unpassivated Si is of the same order as the transition time from transient to steady state behavior reported here.[12,13]

If indeed the electrons recombine after ~100 ps, then the steady state component should be driven solely by the diffusion of heat (thermal wave). To verify this assertion a second experiment was conducted that involved coating the sample with a thin (30 nm) aluminum film. The aluminum film serves two purposes. First, most of the pump energy is absorbed in the aluminum film. Thus, few photoexcited carriers are created in the silicon substrate. Second, the influence of diffusing electrons is effectively screened by the aluminum film leaving only a thermal wave component. The lock-in phase responses for the pristine sample (solid) and the coated sample (dotted) for a delay time t=133ps are shown on the left hand side of Fig. 3d. Two different pump modulation frequencies were used (50 kHz and 300 kHz). Additionally, the thermal wave was modeled taking into account the effect of the aluminum film. This model is similar to that of Reichling and Gronbeck[14] and uses a Gaussian source profile. The results of this model are presented on the right hand side of Fig. 3d. The close agreement between the pristine substrate and the coated substrate as well as the close agreement between the pristine substrate and prediction confirm that after transition the steady state is to be associated with a thermal wave. It should be noted that the predicted thermal wave phase for the bare substrate and the coated sample are almost identical owing to the near parity in Si and Al thermal diffusivity. Moreover for these modulation frequencies, the thermal wavelength (~12 μm at 200 kHz for both materials) is large relative to the film thickness and as a result the thermal wave penetrates a considerable distance into the Si substrate and is a function primarily of the substrate thermal properties.

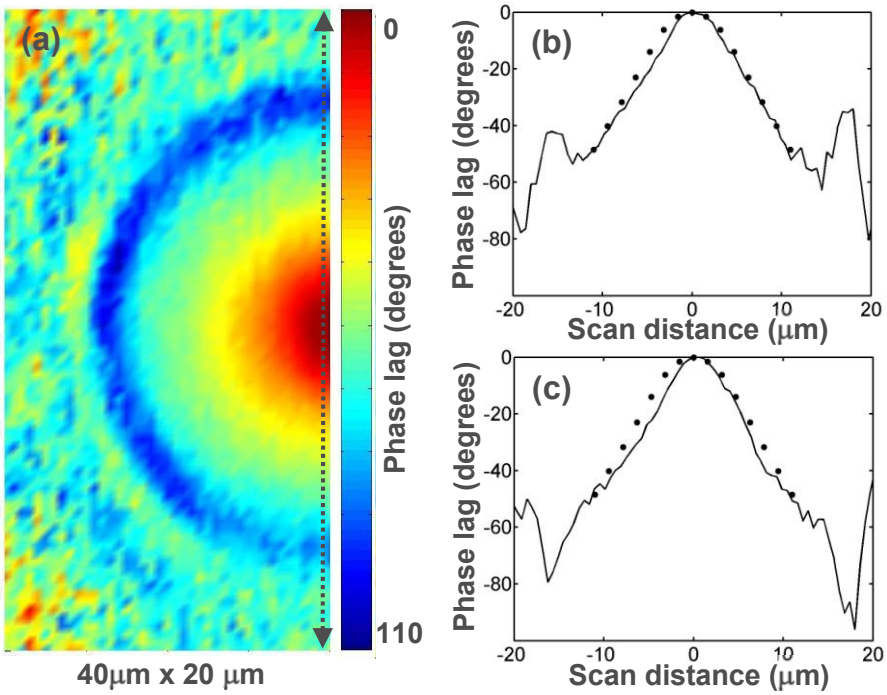

Fig. 4a. Interferometric image of thermal wave and the surface acoustic phonon pulse. Fig. 4b and 4c. Profile of the image along the superposed line for maximum positive and negative interferometric phase sensitivity.

The photoexcited electrons, in addition to being a source of thermal waves, also serve to excite coherent acoustic phonon pulses. In Si, the photoexcitation of carriers into the conduction band followed by the fast relaxation to the band edge and subsequent phonon assisted recombination produce a localized hydrostatic stress in the material. This stress is given by the sum of the thermal stress ($\propto B\beta\Delta T$) and the electronic stress arising from the hydrostatic deformation potential $\propto (B\partial E_g/\partial pN)$, where B is the bulk elastic modulus and β is the linear thermal expansion coefficient. This stress distribution serves to launch bulk and surface acoustic phonon pulses. In the present case involving same side generation and detection, only acoustic phonon pulses that propagate along the surface of the sample are resolved.

The surface acoustic phonon pulse is imaged using a common path Sagnac interferometer to detect changes in optical phase as well as changes in probe reflectivity.[15,16,17] The interferometer relies on the interference between a probe pulse that arrives before the pump (reference pulse) and a second probe pulse that arrives after the pump pulse (signal pulse). The polarity of the optical phase sensitivity of the interferometer can be changed using a $\lambda/4$ plate.[15] An interferometric phase image of the thermal wave component and the surface acoustic phonon pulse are shown in Fig. 4a. The pump modulation frequency was set to 200 kHz to aid in the imaging of both the thermal wave and the surface acoustic phonon pulse. At this modulation frequency the thermal wave amplitude dominates the surface acoustic phonon amplitude; however, by monitoring the lock-in phase instead of the lock-in amplitude, both the thermal wave and the surface acoustic phonon pulse are imaged with comparable signal contrast. The image was formed by raster scanning the interferometric probe for a fixed pump probe delay time (3ns). The information contained in Fig. 4a is better understood by taking a cross section of

the data along the superposed line shown on the right hand side of Fig. 4a. The data in Fig. 4b and 4c correspond to maximum positive and negative interferometric phase sensitivity respectively. The linear variation near the center corresponds to the thermal wave component of the signal. Since this is the steady state component of the signal, the interferometer only senses changes in probe reflectivity. The low frequency detection limit (~1GHz) of the two beam interferometer is related to path length difference of the two beams upon striking the sample. This is well above the steady state component at the pump modulation frequency (200 kHz). The slope of this variation is the same in both figures and is directly related to the thermal diffusivity.[18] The predicted variation in the thermal wave phase (dots) is also shown in Fig. 4b and 4c.

The rapid variation in the lock-in phase signal near the edges of Figs. 4b and 4c correspond to the surface acoustic phonon pulse. The surface acoustic pulse is a transient component, and as a result the Sagnac interferometer senses changes in optical phase as well as strain induced changes in reflectivity. However, since the polarity of the surface acoustic pulse changes for positive and negative interferometric phase sensitivity, the optical phase contribution is the dominant contributor to the signal. The shape of the surface acoustic phonon wavefront is related to the symmetry of the elastic stiffness tensor and has been modeled previously.[19]

1.3 Conclusion

In conclusion, we have microscopically imaged thermal diffusion and surface acoustic phonon propagation within a single crystallite of a polycrystalline Si sample. The experimental approach holds the potential to measure the thermal diffusivity, the elastic stiffness tensor and the carrier recombination time. This approach should find wide application in the investigation of carrier and phonon transport properties in novel solar electric and optoelectronic materials.

REFERENCES

[1] Thomsen C., Grahn H. T., Maris H. J., Tauc J., "Surface Generation and Detection of Phonons by Picosecond Light Pulses," Phys. Rev. B, 34, 4129 (1986).

[2] Wright O. B., Perrin B., Matsuda O., Gusev V. E., "Ultrafast carrier diffusion in gallium arsenide probed with picosecond acoustic pulses,"Phys. Rev. B, 64, 081202(R) (2001).

[3] von der Linde D., Kuhl J., Klingenberg H., "Raman Scattering from Nonequilibrium LO Phonons with Picosecond Resolution," Phys. Rev. Lett. 44, 1505 (1980).

[4] Yoon H. W., Wake D. R., Wake J. P., Morkoc H., "Inplane Transport of photoexcited carriers in GaAs Quantum-wells," Phys. Rev. B 46, 13461 (1992).

[5] Wright O. B., Gusev V. E., "Ultrafast acoustic phonon generation in gold," Physica B 220, 770 (1996).

[6] Cahill D. G., Ford W. K., Goodson K. E., Mahan G. D., Majumdar A., Maris H. J., Merlin R., Phillpot S. R. "Nanoscale thermal transport," J. Appl. Phys. 93, 793 (2003).

[7] Tachizaki T., Muroya T., Matsuda O., Sugawara Y., Hurley D. H., Wright O. B., "Scanning ultrafast Sagnac interferometry for imaging two-dimensional surface wave propagation," Rev. Sci. Instrum. 77, 043713 (2006).

[8] Opsal J., Rosencwaig A., "Thermal and plasma wave depth profiling in silicon," Appl. Phys. Lett., 47, 498 (1985).

[9] V. E. Gusev, A. A. Karabutov, *Laser Optoacoustics* (AIP Press, New York, 1993).

[10] Shockley W., Read W. T., "Statistics of the Recombinations of Holes and Electrons," Phys. Rev., 87, 835 (1952).

[11] Hall R. N., –Electron-Hole Recombination in Germanium," Phys. Rev., 87, 387 (1952).

[12] Doany R. E., Grischkowsky D., Chi C-C., –Carrier lifetime versus ion-implantation dose in silicon on sapphire," Appl. Phys. Lett., 50, 460 (1987).

[13] Bambha N. K., Nighan W. L., Campbell I. H., Fauchet P. M., –Trapping time in processed polycrystalline silicon measured by picosecond time-resolved reflectivity," J. Appl. Phys., 63, 2316 (1988).

[14] Reichling M., Gronbeck H., –Harmonic heat flow in isotropic layered systems and its use for thin film thermal conductivity measurements," J. Appl. Phys., 75, 1914 (1994).

[15] Hurley D. H., Wright O. B., –Detection of Ultrafast Phenomena Using a Modified Sagnac Interferometer," J. Opt. Lett. 24, 1305 (1999).

[16] Sugawara Y., Wright O. B., Matsuda O., Takigahira M., Tanaka Y., Tamura S., Gusev V.E., –Watching ripples on crystals," Phys. Rev. Lett. 88, 185504 (2002).

[17] Hurley D. H., Telschow K. L., –Simultaneous microscopic imaging of elastic and thermal anisotropy," Phys. Rev. B (R), 71, 241410 (2005).

[18] Maznev A. A., Hartmann J., Reichling M., –Thermal wave propagation in thin films on substrates," J. Appl. Phys. 78, 5266 (1995).

[19] Farnell G. W. and Adler E. L., in *Physical Acoustics*, edited by W. P. Mason and R. N. Thurston (Academic, New York, 1972), Vol. 9, p. 109-166.

Appendix D. Phonon Transport Across Interfaces: Picosecond Measurements of Kapitza Resistance of the Interfaces (Published Paper #2)

This appendix contains a published paper. The only changes made from the published work was the reformatting of paragraphs and the resizing of figures and captions to fit within the style of this document. The original was a two-column format.

Time resolved imaging of carrier and thermal transport in silicon

D. H. Hurley[1], O. B. Wright[2], O. Matsuda[2], S. L. Shinde[3]
[1]*Materials Science and Engineering, Idaho National Laboratory (INL), P.O. Box 1625, Idaho Falls, ID 83415-2209, USA*
[2]*Division of Applied Physics, Graduate School of Engineering, Hokkaido University, Sapporo 060-8628, Japan*
[3]*Sandia National Laboratories (SNL), New Mexico, PO Box 5800,Albuquerque, NM 87185, USA*

We use ultrashort optical pulses to microscopically image carrier and thermal diffusion in two spatial dimensions in pristine and mechanically polished surfaces of crystalline silicon. By decomposing changes in reflectivity in the latter sample into a transient component that varies with delay time and a steady-state component that varies with pump chopping frequency, the influence of thermal diffusion is isolated from that of carrier diffusion and recombination. Additionally, studies using carrier injection density as a parameter are used to clearly identify the carrier recombination pathway.

Great potential exists for the use of nanostructured semiconductor materials in energy conversion systems, including advanced superlattice-based photovoltaics[1] and nanoscale thermoelectric materials.[2] In spite of this, there is still considerable debate regarding the detailed mechanisms governing thermal transport in these systems.[3] Continued progress in this field requires the development of spatially and temporally resolved metrology tools with well-characterized experimental parameters.

Laser-based methods have emerged as a leading candidate for making precise thermal transport measurements due to their non-contact nature and well-defined optical coupling conditions. Laser excitation can be implemented in the frequency domain using amplitude modulated continuous wave (cw) laser heating[4,5,6] or in the time domain using pulsed laser heating.[7,8] The probe beam either reflects off the material surface, sampling the heated region (through thermoreflectance), or propagates along the surface, sampling the heated gas just above the surface (through the mirage effect).[9] For imaging applications, the highest lateral spatial resolution is obtained by scanning a probe beam spot at normal incidence. The spatial resolution depends on the thermal wavelength or the diffusion length, and is ultimately limited by the laser spot size.

For thermal transport measurements on semiconductors, a metallic transducer layer is typically used to avoid complicated data analysis owing to the presence of a diffusing photoexcited electron-hole plasma.[10,11] However, the transducer layer introduces new experimental parameters. It is thus advantageous to use measurement schemes involving

uncoated semiconductor materials. Such experiments require relating the changes in optical properties to the co-evolution of the plasma and the temperature fields.

For pulsed-laser measurements, transport properties in the depth direction are solely monitored when the pump optical spot size is much larger than the plasma or thermal diffusion lengths [12,13,14]. In such an example closely related to the present study, Tanaka *et al*.[15] have imaged plasma and thermal diffusion in an uncoated ion-irradiated crystalline Si sample. By changing the delay between the pump and probe pulses, they measured the relative contributions of the plasma and temperature fields to the change in probe reflectivity. However, they did not probe times greater than the carrier recombination time.

Alternatively, for pulsed-laser measurements, one can also monitor transport properties in the lateral direction when the pump optical spot size is on the order of or much smaller than the plasma or thermal diffusion lengths. For short laser pulse durations, t_l<1 ns, this approach requires near-field optical focusing.[16] Similarly, for chopped cw laser excitation, the chopping frequency can be varied to determine the relative contributions of the plasma and temperature fields;[10] however, unlike pulsed-laser studies the thermal and plasma waves cannot easily be decoupled.

Recently, a new approach[17,18] has emerged that uses elements of both time and frequency domain methods. This hybrid approach uses a time-delayed probe pulse to laterally image transient as well as steady-state contributions to the change in the probe reflectivity. In this paper we use this method to image plasma and thermal diffusion in a crystalline silicon sample damaged by mechanical polishing, thereby enabling lateral thermal transport to be completely decoupled from that of the plasma. For probe delays that are large in comparison to the carrier recombination time, it is shown that the optical reflectivity changes arise solely from thermal diffusion. In this way, the in-plane thermal properties of the substrate can be accurately probed.

The experimental setup used for imaging changes in reflectivity is shown at the top of Fig. 1. It is similar to the setup presented by Tachizaki et al.[19] and involves translation of a probe beam relative to a fixed pump beam at normal incidence. A single probe pulse monitors changes in probe reflectivity. The probe beam is sent through a confocal lens pair (of focal length 100 mm) and is focused onto the sample at near-normal incidence using a microscope objective. The first lens in the confocal system is attached to a stage that allows the lens and the probe beam to be translated in the x-y plane. The probe beam propagation vector remains collinear with the lens axis. The second lens converts the x-y motion of the beam into a change in entrance angle into the objective. The pump beam is guided along the optical axis of the objective using a dichroic beam splitter placed after the lens pair. The pump and probe beams, of wavelengths 400 nm and 800 nm and incident pulse energies 0.026 nJ and 0.013 nJ, respectively, are derived from a Ti:Sapphire laser with a pulse duration ~200 fs. The respective spot diameters of the pump and probe beams at the sample are 4.6 μm and 4.0 μm (at FWHM intensity). The pump beam was chopped at a frequency in the range f_0=10-50 kHz to enable measurements of diffusion processes at these frequencies. The maximum transient temperature rise caused by a single pump pulse is 5 K,[20] and the steady-state temperature rise is ~0.5 K.[5] Typical values of the relative change in reflectivity of the probe beam ($\Delta R/R_o$) ranged from ~10^{-4} to 10^{-3}.

The two samples studied are cleaved from a single boron-doped (p-type) (100) Si wafer with a doping concentration of 2×10^{16} cm^{-3}, with two different surface preparations. One sample, referred to as the mechanically polished sample, is obtained by polishing the as-received (100) surface using a (3 μm) diamond slurry and then (0.05 μm) colloidal silica.[21] This process significantly damages the crystal lattice in the near-surface region (~1 μm)[22]. This sample is then annealed at 300°C to relieve the residual stress caused by polishing. The second sample is in the as-received state. In this case the vendor used a dilute HF etch to remove any residual surface damage. In all cases investigated, the crystal [011] axis is aligned with the laboratory x-axis.

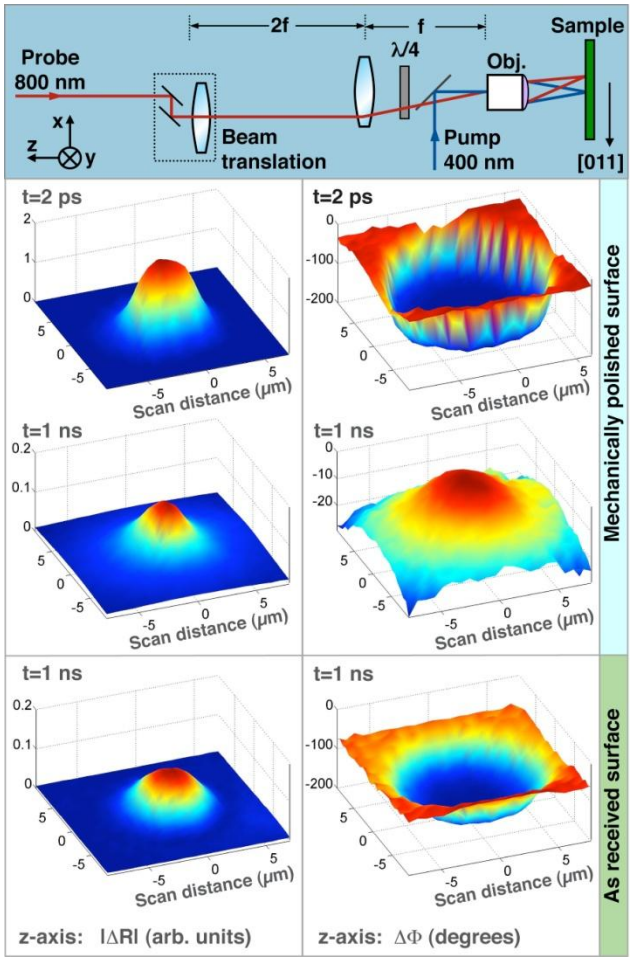

FIG. 1. Top: Experimental setup. The dashed box represents a dual stage system that that allows the lens and the probe beam to be translated in the *x*-y plane. A single objective is used for focusing light onto the sample. Bottom: Images of the amplitude and phase of the probe reflectivity change as a function of delay time, using a chopping frequency f_0=50 kHz. At early delay times, the transient component that varies with delay time is dominant. At large delay times, for the mechanically polished surface, the steady-state component is dominant.

The series of images in Fig. 1 represent the modulus $|\Delta R(t)|$ (left column) and phase lead $\Delta\Phi(t)$ (right column) of the reflectivity variation measured by the lock-in amplifier at a chopping

frequency f_0=50 kHz at two delay times: t=2 ps and t=1 ns. We first consider the results for the mechanically polished surface. We decompose the signal into two components. The first is a transient component that depends on the delay time, and depends on a summation of the effects of thermal and plasma waves at harmonics of the laser pulse repetition frequency (76 MHz).[23,24] The second is a steady-state component associated with a temperature oscillation at the pump chopping frequency. The relative magnitude of these components depends on f_0 and t. For these measurements at f_0=50 kHz, the transient component is dominant at relatively short times on the order of a few ps: at t=2 ps there is little lateral spatial variation in the phase over the excitation region, and the primary gradients in temperature and carrier density are in a direction perpendicular to the surface (over the pump optical skin depth of 82 nm). Thus, at t=2 ps, $\Delta\Phi(t)$ should primarily be influenced by such perpendicular gradients. $\Delta R(t)$ is an averaged response over the probe skin depth (~10 μm), which is considerably larger than the pump skin depth (82 nm)[25] as well as the plasma and thermal diffusion lengths at 2 ps (28 nm and 13 nm, respectively). [26]

The images of $|\Delta R(t)|$ and $\Delta\Phi(t)$ for the mechanically polished surface at t=1 ns are markedly different. Unlike the behavior at t=2 ps, $\Delta\Phi$ decreases steadily with increasing distance from the source. Moreover, the profiles of $|\Delta R(t)|$ and $\Delta\Phi(t)$ no longer vary with increasing delay time, instead showing a steady-state behavior. The rapid decrease in the transient component is due to the short (<1 ns) recombination time, τ_r, associated with surface trap sites.[27] After t=1 ns, the transient component vanishes, leaving only the steady-state component.

For the as-received sample measured under the same experimental conditions, $|\Delta R|$ at t=2 ps (not shown) is essentially the same as that for the mechanically polished surface. However, $|\Delta R|$ and $\Delta\Phi$ for t=1 ns, as shown in Fig. 1, are qualitatively different from that of the mechanically polished surface: the transient component remains dominant, as evidenced by the flat $\Delta\Phi$ spatial profile. This is understandable given that the plasma and thermal diffusion lengths at 1 ns, ~700 nm, and ~300 nm respectively, are considerably smaller than the laser spot size for this sample. Compared to the mechanically polished sample, surface passivation by etching results in a much slower surface recombination velocity and a persistence of the transient component.[22]

Further analysis of the results for the mechanically polished sample is beneficial because, for delay times greater than the carrier recombination time, the experimental results can be analyzed using a simplified thermal wave model in three spatial dimensions (3D). This model, which has been discussed in detail in a previous paper,[28] considers thermal waves produced by a sinusoidal heat input. Because of the relatively low chopping frequencies here, we do not consider the effect of thermal waves at frequencies corresponding to harmonics of the laser pulse repetition frequency.[23,24] The volumetric thermal wave source associated with the chopped pump beam is taken to have a Gaussian profile in the lateral direction determined by the cross-correlation of the pump and probe spot sizes[29] and a decaying exponential profile in the depth direction (over the pump beam optical skin depth of 82 nm). While it is assumed that the damaged layer will have an appreciably smaller thermal conductivity than the pristine substrate, for the pump chopping frequencies considered it can be shown that the perturbation caused by the damaged layer on the thermal wave phase profile is relatively small.[30] We will thus assume that the sample is homogeneous. The literature value of the optical skin depth for crystalline Si at the pump wavelength is used.[25] Figure 2(a) shows the experimental profiles at t=1.5 ns, at two

different chopping frequencies f_0=10 and 50 kHz, compared with $\Delta\Phi(x)$ obtained from the thermal wave model, where x is the lateral scan distance. The thermal diffusivity used for the model results presented in Fig. 2(a) is obtained by fitting the predicted and experimentally measured thermal wave phase profiles $\Delta\Phi(x)$. The best fit value for the thermal diffusivity $D=(8.8 \pm 0.2)\times10^{-5}$ m^2s^{-1} is very close to the literature value $D=8.71\times10^{-5}$ m^2s^{-1} for pure crystalline Si.[26,31,32] The good correspondence between experiment and simulation at f_0=10 kHz (corresponding to a thermal diffusion length l=53 μm) and 50 kHz (l=24 μm) confirms that after t=1.5 ns the electrons have recombined and that the steady-state component is driven solely by thermal diffusion. Our value for D illustrates that the surface damaged layer does not significantly alter $\Delta\Phi(x)$.

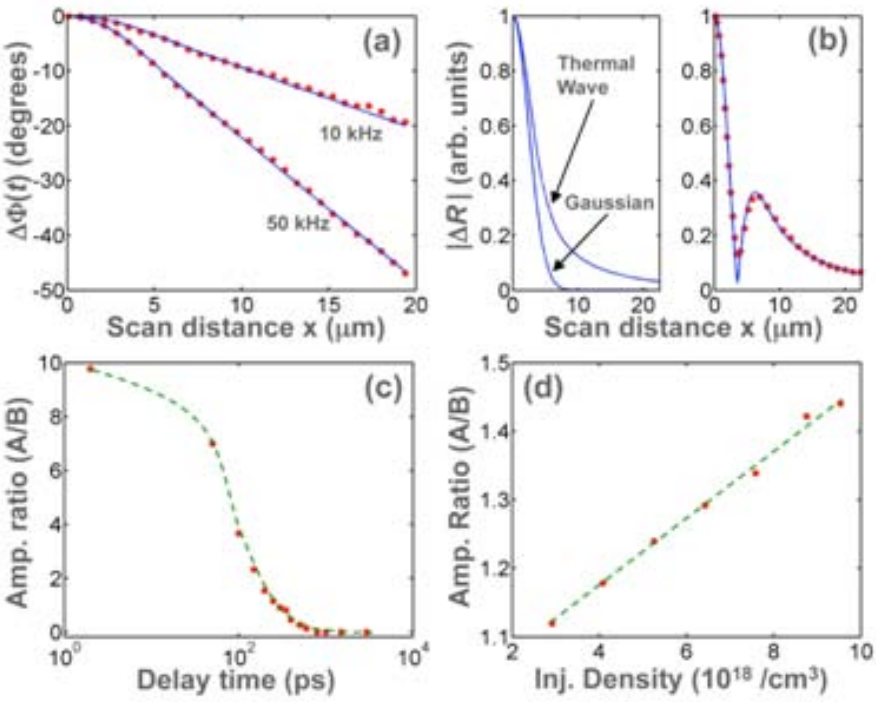

FIG. 2. (a) Experimental phase lead profile $\Delta\Phi$ (dotted) measured at t=1.5 ns and a 3D simulation based on thermal waves (solid) (b) Right: Experimental $|\Delta R|$ (dots) and corresponding theoretical profile according to Eq. (1) (solid line). Left: Theoretical profile for $|\Delta R|$ arising from the thermal waves. The Gaussian represents the cross correlation of the pump and probe spots. (c) Amplitude ratio A/B versus delay time. (d) Amplitude ratio A/B versus plasma injection density for a delay time of 250 ps. The dashed lines in (c) and (d) are guides to the eye. The chopping frequency corresponding to (b)-(d) is f_0=50 kHz.

To better understand the plasma dynamics for this mechanically polished sample, we examine an intermediate delay time: the right-hand plot in Figure 2(b) shows $|\Delta R|$ for f_0=50 kHz and t=200 ps, at which delay the magnitude of the transient and steady-state components are comparable. The reflectivity change associated with the steady-state component is proportional to the surface temperature oscillation, of amplitude $\Delta\hat{T}_{SS}(x)$, and to the surface carrier density oscillation, of amplitude $\Delta\hat{N}_{SS}(x)$, of the thermal and plasma waves, respectively, at the chopping

frequency. Because the carrier recombination time (approximated here to be less than 1 ns) is much smaller than the pump chopping period, $\Delta\hat{N}_{ss}(x)$ can be neglected. The reflectivity change associated with the transient component is proportional to the transient change in surface temperature, $\Delta\hat{T}_{tr}(x,t)$, and to the transient change in surface carrier density, $\Delta\hat{N}_{tr}(x,t)$. For early times before a significant fraction of the carriers have recombined, the transient component is dominated by the diffusing plasma.[10] A simple model that reproduces $|\Delta R(x)|$ in the mechanically polished sample for a specific delay time is given by

$$\left|\frac{\Delta R(x)}{R}\right| \propto \left| A(t)\ \Delta\hat{N}_{tr}(x,t)e^{i\theta_{tr}} + B\ \Delta\hat{T}_{ss}(x)e^{i\theta_{ss}(x)} \right| \quad (1)$$

where $A(t)$ and B are respectively the relative contributions of the plasma component and steady-state component, and $\theta_{ss}(x)$ and θ_{tr} are the respective phases of the thermal wave and transient component. $\Delta\hat{T}_{ss}(x)$ and $\theta_{ss}(x)$ are taken from the 3D thermal wave simulation described above. The coefficient B is not a function of time, and is determined from the measurements of $|\Delta R|$ for f_0=50 kHz and t=1 ns, a time for which $|\Delta R|$ is solely associated with the thermal wave. $\Delta\hat{N}_{tr}(x,t)$ is assumed to mimic the Gaussian spatial profile of the autocorrelation of the pump and probe pulses at t=2 ps. The flat phase profile of the transient component is determined by the constant value of θ_{tr} equal to the difference between $\Delta\Phi$ at t=1 ns (dominated by the thermal wave) and $\Delta\Phi$ at t=2 ps (dominated by the plasma wave) at x=0 (the spot center). This phase difference, illustrated in Fig. 1, is ~180°, indicating that these two components have opposite signs.[10] This model, which neglects the diffusing nature of the plasma (i.e., it replaces the plasma wave with a static amplitude profile and phase), is reasonable since the plasma diffusion length (700 nm) for a 1-ns recombination time is only a small fraction of the pump and probe spot sizes. $\Delta\hat{T}_{ss}(x)$ and $\Delta\hat{N}_{tr}(x,t)$ are shown on the left-hand side of Fig. 2(b). Equation (1) can be fitted to $|\Delta R(x)|$ for any given delay using A/B as a fitting parameter. The result of this procedure for t=200 ps is shown on the right-hand side in Fig. 2(b). In Fig. 2(c), we plot A/B vs. ln(t).

The vanishing of the transient component at long delay times further illustrates that the photoexcited carriers in the mechanically polished sample have recombined after 1 ns. Carrier-density-dependent Auger recombination can be neglected because the recombination time connected with this pathway is estimated to be in excess of 20 ns.[33] Rather, our data is consistent with fast recombination associated with the Shockley-Read-Hall (SRH)[27,34,35,36] recombination pathway. SRH recombination sites arise from lattice defects in highly damaged surface layers. In our mechanically polished sample, this layer extends to approximately 1 μm below the surface,[22] which is larger than the plasma diffusion length of ~700 nm at 1 ns.[26] The diffusing photoexcited carriers therefore cannot escape from the damaged layer before recombination.

The experimentally derived functional dependence of A/B on the average injected carrier density N_0 sampled by the probe spot is shown in Fig. 2(d) for a delay of 250 ps.[37,38] A/B increases linearly with increasing fluence and hence with increasing injection density N_0. Previous studies on polycrystalline Si have shown that SRH recombination centers saturate at high N_0.[39,40] This behavior is consistent with the observed increase in the transient component

with increasing N_0. Moreover, the screening of SRH sites slows recombination, leading to the observed persistence of the transient component, which is primarily governed by the diffusing plasma.

In conclusion, we use ultrashort optical pulses to microscopically image carrier and thermal diffusion in two spatial dimensions in pristine and mechanically polished surfaces of crystalline silicon. By decomposing changes in optical reflectivity into a transient component that varies with delay time and a steady-state oscillating component at the pump chopping frequency, the respective influences of carrier recombination and thermal diffusion are identified. We demonstrate that for probe delays that are large in comparison to the carrier recombination time in the mechanically polished sample, thermal and plasma diffusion can be completely decoupled. By means of a 3D heat diffusion model for the oscillating temperature at the pump chopping frequency, we derive the thermal diffusivity of the polished sample. Furthermore, studies as a function of carrier injection density are used to confirm the recombination pathway in this sample. This study provides a useful starting point for the further investigation of the 3D diffusion of thermal and plasma waves in a variety of treated semiconductor surfaces.

This work was supported by an INL and SNL LDRD under DOE Contract DE-AC07-05ID14517. Accordingly, the U.S. Government retains a nonexclusive, royalty-free license to publish or reproduce the published form of this contribution, or allow others to do so, for U.S. Government purposes.

[1] G.J. Conibeer, D. König, M.A. Green, and J.F. Guillemoles, Thin Solid Films **516**, 6948 (2008).
[2] R. Venkatasurbramanian, Phys. Rev. B **61**, 3091 (2000).
[3] D. G. Cahill, W. K. Ford, K. E. Goodson, G. D. Mahan, A. Majumdar, H. J. Maris, R. Merlin, and S. R. Phillpot, J. Appl. Phys. **93**, 793 (2003).
[4] W. B. Jackson, N. M. Amer, C. Boccara, and D. Fournier, Appl. Opt. **20**, 1333 (1981).
[5] J. Opsal, A. Rosencwaig, and D. L. Willenborg, Appl. Opt. **22**, 3169 (1983).
[6] J. Hartmann, P. Voigt, and M. Reichling, J. Appl. Phys. **81**, 2966 (1997).
[7] C. A. Paddock and G. L. Eesley, J. Appl. Phys. **60**, 285 (1986).
[8] Yee Kan Koh, S. L. Singer, W. Kim, J. M. O. Zide, Hong Lu, D. G. Cahill, A. Majumdar, and A. C. Gossard, J. Appl. Phys. **105**, 54303 (2009).
[9] A. C. Boccara, D. Fournier, and J. Badoz, Appl. Phys. Lett. **36**, 130 (1980).
[10] J. Opsal, and A. Rosencwaig, Appl. Phys. Lett. **47**, 498 (1985).
[11] W. S. Capinski, H. J. Maris, R. Ruf, M. Cardona, K. Ploog, and D. S. Katzer, Phys. Rev. B **59**, 8105 (1999).
[12] M. G. Grimaldi, P. Baeri, and E. Rimini, Appl. Phys. A: Solids Surf. **33**, 107 (1984).
[13] O. B. Wright and V. E. Gusev, Appl. Phys. Lett. **66**, 1190 (1995).

[14] A. J. Sabbah and D. M. Riffe, J. Appl. Phys. **88**, 6954 (2000).
[15] T. Tanaka, A. Harata, and T. Sawada, J. Appl. Phys. **82**, 4033 (1997).
[16] M. Vollmer, H. Giessen, W. Stolz W, W. W. Ruhle, L. Ghislain, and V. Elings, Appl. Phys. Let. 74, 1791 (1999).
[17] T. Bienvill, L. Belliard, P. Siry and B. Perrin, Superlattices and Microstructures **35**, 363 (2004).
[18] D. H. Hurley, and K. L. Telschow, Phys. Rev. B **71**, 241410 (2005).
[19] T. Tachizaki, T. Muroya, O. Matsuda, Y. Sugawara, D. H. Hurley, and O. B. Wright, Rev. Sci. Instrum. 77, 043713 (2006).
[20] C. Thomsen, H.T. Grahn, H. J. Maris, and J. Tauc, Phys. Rev. B **34**, 4129 (1986).
[21] The colloidal silica contains dilute sodium peroxide. Thus, there is some chemical polishing in addition to mechanical polishing.
[22] R. Stickler, and G. R. Booker, J. Electrochem. Soc. **111**, 485 (1964).
[23] D. G. Cahill, Rev. Sci. Instrum. **75**, 5119 (2004).
[24] A. J. Schmidt X. Chen and G. Chen, Rev. Sci. Instrum. **79**, 114902 (2008).
[25] The index of refraction used in this calculation is for crystalline Si, and is taken from, Handbook of Optical Constants of Solids, edited by Edward Palik (Elsevier, 1998). It has been observed that the index of refraction for a mechanically polished surface can differ from that of a passivated surface: M. Ohlidal, I. Ohlidal, F. Lukes, Surf. Sci. **55**, 467 (1976).
[26] The plasma and thermal diffusion lengths are given by $l=(Dt)^{1/2}$, where D is either the ambipolar diffusion coefficient or the thermal diffusivity, and t is the pump-probe delay time. The literature value of the carrier-density-dependent ambipolar diffusion coefficient is taken from, Chun-Mao Li, T. Sjodin, Hai-Lung Dai, Phys. Rev. B **56**, 15252 (1997). The value of the thermal diffusivity is taken from, H.R. Shanks, Phys. Rev. **130**, 1743 (1963).
[27] F. E. Doany, D. Grischkowsky, and C. –C. Chi, Appl. Phys. Lett. **50**, 460 (1987).
[28] D. H. Hurley, and M. K. Fig, J. Appl. Phys., **104**, 123703 (2008).
[29] O. B. Wright R. Li Voti, and O. Matsuda, J. Appl. Phys. **91**, 5002 (2002).
[30] The error incurred by assuming the sample to be homogeneous can be estimated using a simple expression for the thermal wave dispersion taken from, Maznev, J. Hartmann, and M. Reichling, J. Appl. Phys. **78**, 52661995. For a 1 μm damaged layer with a thermal conductivity that is one half that of single crystal Si, the difference in the thermal wave phase over a 20 μm scan distance is 0.02°.
[31] The best fit was obtained by minimizing the standard deviation. The uncertainty corresponds to a value of D that has an associated standard deviation that is 30% larger than the minimum.
[32] Thompson, J. C. and B. A. Younglove, *J. Phys. Chem. Solids* **20,** 112 (1961) 146-149. At 300 K the thermal conductivity is practically independent of the doping concentration.
[33] The Auger recombination time is given by $\tau=1/CN^2$, where N is the carrier density and the Auger recombination coefficient ($C=4\times10^{-31}$ cm^{6}s^{-1}) is taken from V. E. Gusev and A. A. Karabutov, *Laser Optoacoustics (*AIP Press, New York, 1993.)
[34] W. Shockley, and W.T. Read, Phys. Rev. **87**, 835 (1952).
[35] R. N. Hall, Phys. Rev. **87**, 387 (1952).
[36] N.K. Bambha, W.L. Nighan, Jr., I.H. Campbell, and P.M. Fauchet, J. Appl. Phys. **63**, 2316 (1988).
[37] The average injected carrier density as measured by the probe spot is taken as the maximum carrier density at the centre of the pump spot reduced by a factor of $1/(1+w_{probe}^2 / w_{pump}^2)$, where w_{pump} and w_{probe} are the respective spot diameters of the pump and probe beams.
[38] B was assumed to be proportional to the pump fluence.
[39] E. Fabre, M. Mautref, and A. Mircea, Appl. Phys. Lett. **27**, 239 (1975).
[40] S. R. Dhariwal, L.S. Kothari, and S.C. Jain, Solid-St. Electron. **24**, 749 (1981).

Appendix E. Phonon Transport Along Interfaces: A Modified Holland Model for Monte Carlo Simulation of Silicon and Germanium

The Holland model for thermal conductivity is revisited in the context of its use in Monte Carlo simulations of silicon and germanium. Recent measurements on isotopically enriched samples of these materials make it possible to separate the effects of interphonon and isotope scattering when determining the constants in the scattering model. Fitting interphonon scattering first, a slight modification in the isotope scattering model is suggested that appears to work well above 100 K for both silicon and germanium with no fitting parameters. Because Monte Carlo simulations enforce boundary scattering outside of the relaxation time approximation, data at temperatures well above the thermal conductivity peak are used to avoid the confounding influence of boundary-scattering models employed in previous work.

E.1 Introduction

Despite their introduction more than forty years ago, the Callaway [1] and Holland [2] models for thermal conductivity are still often used in materials where phonons dominate thermal transport. The Callaway model assumed a Debye phonon spectrum explicitly, whereas the Holland model attempted to introduce some effect of dispersion by representing the longitudinal acoustic (LA) and transverse acoustic (TA) branches separately, as well as breaking the TA branch into two linear segments.

Although the dispersion relation employed by Holland appears far closer to experimentally measured relations, the Debye assumption still lurks below the surface. In particular, Holland's expressions assume the equivalence of phonon phase and group velocities [3, 4]. For LA phonons and low-frequency TA phonons, this assumption is consistent with the assumed dispersion relation. For high-frequency TA phonons, even with a linear dispersion relation, this is an incorrect assumption due to the nonzero y-intercept. This issue becomes important as more realistic dispersion relations are introduced in analytic and numerical models, such as discrete ordinates [5, 6] and Monte Carlo [7, 8, 9] solutions to the Boltzmann transport equation (BTE).

E.2 Mathematical Formulation

The familiar expression for thermal conductivity, κ, based on phonon transport properties is

$$\kappa = \frac{1}{3} C v \lambda, \tag{E-1}$$

where C is the specific heat, v is the average phonon group speed, and λ is the average phonon mean free path. This expression can be derived directly from kinetic theory arguments [10, 11]. In the expression, averaging across frequency and polarization is performed separately for each term. A more rigorous treatment can be obtained by starting from the BTE under the relaxation time assumption, where the rate of return to equilibrium is assumed proportional to the departure

from equilibrium, with the proportionality constant known as the ~~"r~~elaxation time" τ. This process (see [12]) yields an integral expression:

$$\kappa_i = \frac{1}{(2\pi)^3} \sum_p \int (\vec{v} \cdot \hat{\imath})^2 \, \tau C \delta \vec{k}, \tag{E-2}$$

where the $1/(2\pi)^3$ term is the density of states under the periodicity assumption [11], the summation is over all polarizations p, the temperature gradient is along the unit vector $\hat{\imath}$, $\vec{k}$ is the wave vector, and all quantities are wave-vector and polarization dependent [2]. It is worth noting that the derivation in [12] makes it clear that the specific heat per normal mode, C, is strictly based on the equilibrium distribution.

As in the vast majority of previous work, materials herein are assumed isotropic. Under this assumption, the vector integral over the wave vector may be replaced by a scalar integral over the wave number by converting to a spherical integral over a sphere of radius k and observing that the integrands of interest are independent of the azimuthal and polar angles [13].

The alternative path to a scalar integral, taken by most researchers, is to perform the integral in terms of frequency, ω. In the presence of dispersion, this choice can be problematic because it introduces a $d\omega/dk$ term, which can become infinite. Interestingly, Holland moves to a scalar integral in terms of k but then rewrites it in terms of ω after introducing the Debye assumption. In the current work, the integral will remain in terms of k. An added benefit of this choice is that it obviates the need to recover k from ω, which often drives the selection of simple dispersion-fitting functions that can be easily inverted [14].

Performing the integration and normalizing k by $2\pi/a$ (reduced wave number), Equation E-2 becomes

$$\kappa = \frac{4\pi}{3a^3} \sum_p \int v^2 \tau C k^2 \delta k, \tag{E-3}$$

where the $1/3$ springs from the dot product by noting that $v^2 = v_x^2 + v_y^2 + v_z^2$ so, in an isotropic medium, on average, $v_{x,y,z}^2 = 1/3 \, v^2$ [12].

At this point, it may be noted that only two models are required to evaluate Equation E-3: dispersion and relaxation time. It may be further observed that, because relaxation time typically depends on frequency, all terms in Equation E-3 ultimately depend on the dispersion model.

E.3 Dispersion Relation

A dispersion relation is the key link between the simulation and the material. It relates the wave number of a phonon to its frequency, which determines its energy and its phase speed. Also important, the slope of the frequency versus wave-number relationship at a given wave number, k, determines the group speed of a wave packet centered at k, which is the speed at which it will

carry information. Because BTE solutions are most often aimed at quantifying energy transport, group speed is a critical parameter.

Dispersion relations for a number of materials have been measured experimentally via neutron scattering [15, 16], as well as computed using *ab initio* molecular dynamics techniques [17]. For computational convenience, an analytical representation of the dispersion relation is ideal. The literature contains a number of proposals for such representations, many of which are reviewed in [4]. In this work, a fourth-order polynomial was chosen. The dispersion relation is therefore represented by

$$\omega = A_1 k + A_2 k^2 + A_3 k^3 + A_4 k^4. \tag{E-4}$$

E.3.1 Silicon

Fitting Equation E-4 to neutron-scattering data for the [100] direction in silicon from Brockhouse [15] and Nilsson and Nelin [16], the coefficients are found to be

$$\begin{aligned} A_1 &= 16.889222 \\ A_2 &= -2.597880 \\ A_3 &= -4.385738 \\ A_4 &= 2.132736 \end{aligned}$$

for the LA (longitudinal acoustic) branch and

$$\begin{aligned} A_1 &= 11.396625 \\ A_2 &= -5.132308 \\ A_3 &= -6.17036 \\ A_4 &= 4.403547 \end{aligned}$$

for the degenerate TA (transverse acoustic) branches to yield ω in teraHertz.

The resulting polynomial representation of the dispersion relation is compared to the experimental data in Figure E-1.

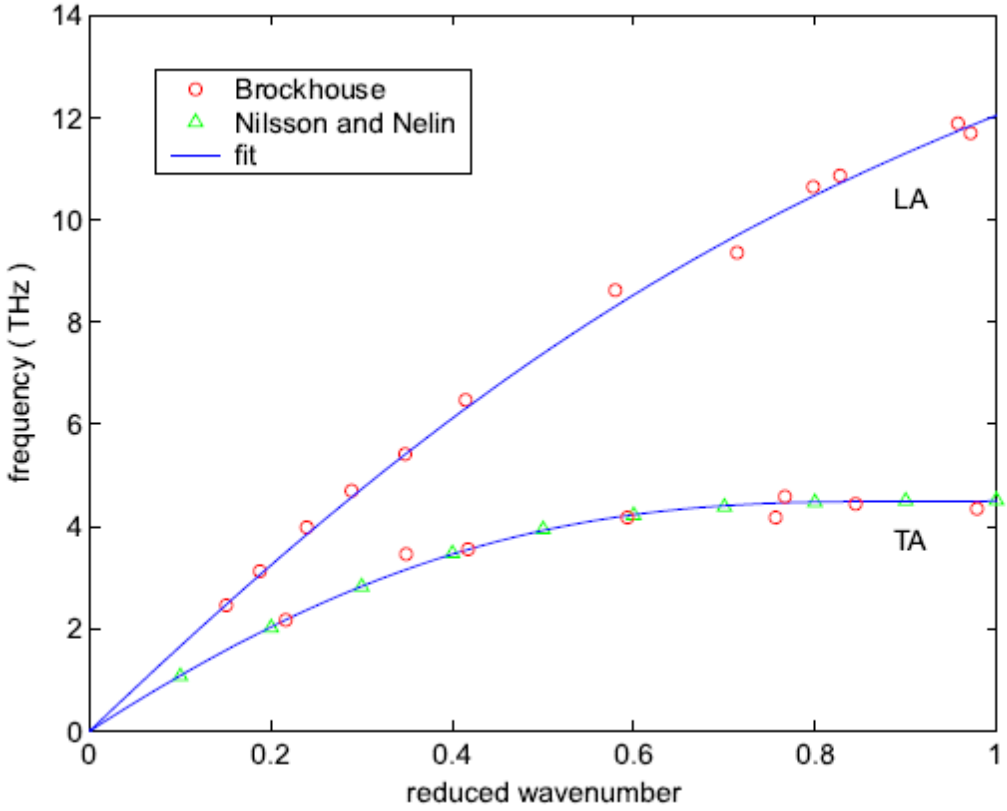

Figure E-1. Comparison of the dispersion relation fit in [100] silicon to experimental data [15, 16].

As a check on the isotropic assumption, the dispersion fit, and the *k*-space integral formulation, we can calculate the specific heat per unit volume via

$$C = \frac{\partial U}{\partial T} \sum_{p} \frac{4\pi\hbar^2}{k_B a^3 T^2} \int_0^1 \omega^2 n^2 e^{\frac{\hbar\omega}{k_B T}} k^2 dk, \tag{E-5}$$

where U is the energy per unit volume, which is obtained by integrating the phonon energy, $\hbar\omega$, over the distribution function.

The result of Equation E-5 as a function of temperature is shown in Figure E-2. While reasonable agreement is obtained at low temperatures, the calculated specific heat departs increasingly from the measured values as T increases. Surmising that the error is due to the omission of optical modes from the calculation, they are included in an approximate manner by assuming that all three modes oscillate at 14 THz, which makes evaluation of Equation E-5 trivial. Adding this contribution to the previous result and plotting in Figure E-2, good agreement is obtained over the entire temperature range.

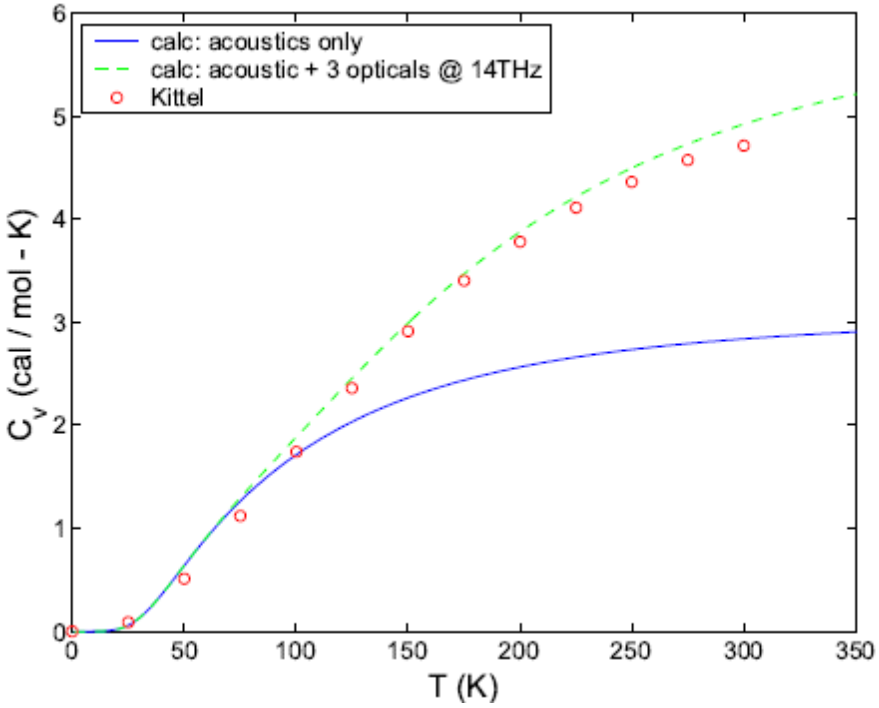

Figure E-2. Comparison of measured specific heat to values computed with Equation E-5 under the dispersion model and k-space integrals used in the current work.

E.3.2 Germanium

Repeating this process for germanium, Equation E-4 is fitted to neutron-scattering data for the [100] direction from Nilsson and Nelin [18]. The resulting coefficients are

$$A_1 = 9.2324$$
$$A_2 = -2.4655$$
$$A_3 = 2.2048$$
$$A_4 = -1.7608$$

for the LA branch and

$$A_1 = 6.222$$
$$A_2 = -0.801$$
$$A_3 = -8.427$$
$$A_4 = 5.488$$

for the (degenerate) TA branches to yield ω in teraHertz.

The resulting polynomial representation of the dispersion relation is compared to the experimental data in Figure E-3. In this case, the fourth-order polynomial had great difficulty fitting the nearly constant frequency region at the Brillouin zone edge (large k). The fit is therefore constrained to a zero slope at a subunity k and a constant ω is used above this value.

The cutoff k was determined via trial and error and was fixed at $k = 0.796$ for the fit shown in Figure E-3.

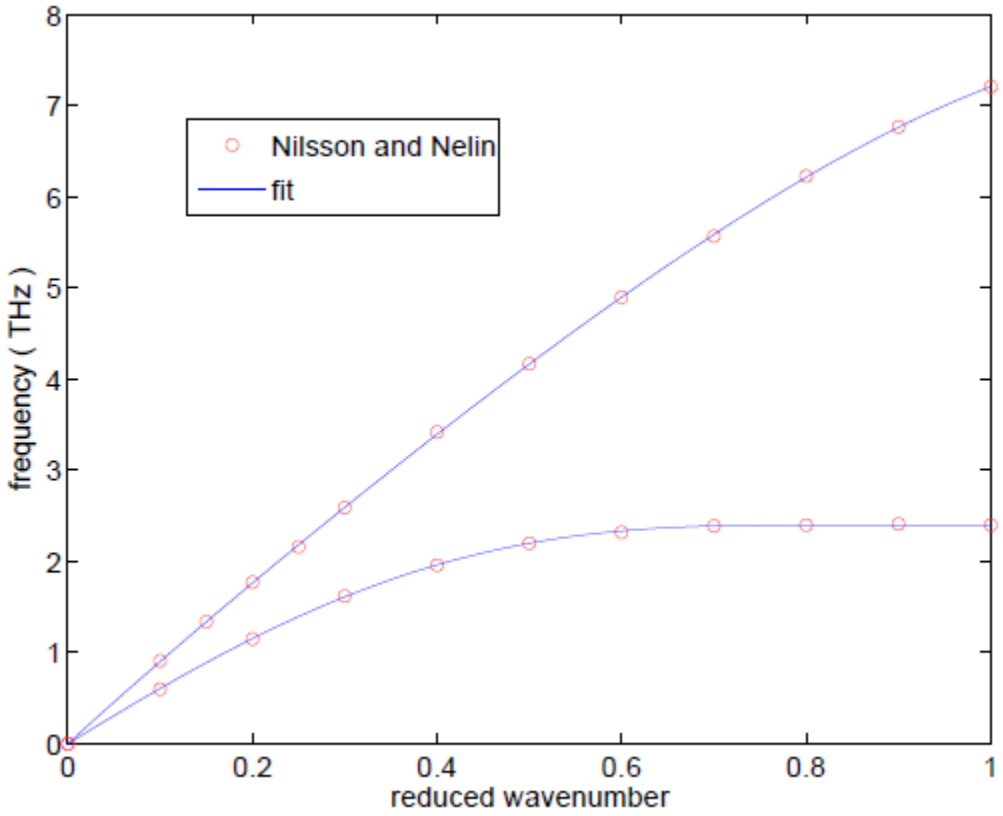

Figure E-3. Comparison of the dispersion relation fit in [100] germanium to experimental data [18].

E.3.3 Phonon Group Speed

An accurate representation of the carrier speed is critical to any transport simulation. For phonons, information is carried at the group speed of the wave packet centered at k, which is given by

$$v_g = \frac{d\omega}{dk}. \tag{E-6}$$

This derivative is trivial to compute under the polynomial approximation to the dispersion relation of Equation E-4, yielding

$$v_g = A_1 + 2A_2k + 3A_3k^2 + 4A_4k^3. \tag{E-7}$$

The resulting group speeds for silicon are shown in Figure E-4(a). Two weaknesses in the current polynomial dispersion model are apparent in this figure. First, the TA group speed drops slightly below zero at $k = 0.193$, then reemerges and reaches 128 m/s at $k = 1$. In this work, the group speed is manually set to zero above $k = 0.193$. A second issue is that the LA group speed does not go to zero at $k = 1$. Given the good fit to the highest k measured in the experiments, it is likely that the speed drops very rapidly to zero near $k = 1$, thus the region in wave-number space with an incorrect speed is relatively small. It may be noted, however, that $k = 1$ is the most probable LA wave number at room temperature, though the distribution is rather flat and TA modes are much more numerous. While it is likely that the effects of this shortcoming are minimal, this conclusion cannot be guaranteed, thus alternative dispersion models should be investigated in future work.

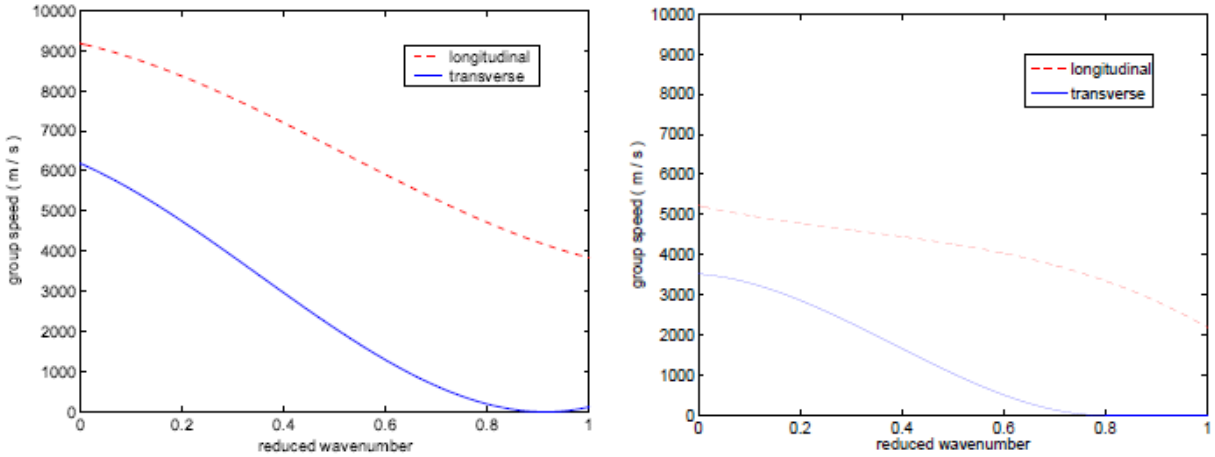

(a) silicon (b) germanium

Figure E-4. Phonon group speed under dispersion model for silicon and germanium.

The group speeds for germanium are shown in Figure E-4(b). Note that the group speed for the TA modes is set to zero for $k > 0.796$ to reflect the k cutoff in the dispersion relation.

E.4 Relaxation Time

E.4.1 Interphonon Scattering

The relaxation time model employed by Holland for interphonon (three phonon) scattering for LA phonons is drawn from an expression derived by Herring [19] for low temperature Normal (momentum conserving) processes involving LA phonons:

$$\tau_{L_{3ph}}^{-1} = B_L \omega^2 T^3 \tag{E-8}$$

although Holland [2] argues in Appendix A that this expression captures Umklapp (momentum destroying) processes as well.

For interphonon scattering in TA modes, Holland employs two models. For low frequencies, Herring's low-temperature expression for Normal processes involving TA phonons is adopted:

$$\tau_{L_{3ph}}^{-1} = B_T \omega T^4. \tag{E-9}$$

For high frequencies, an expression derived in Appendix A of Holland's paper for *U* processes involving dispersive (group speed differs significantly from phase speed) TA phonons is employed:

$$\tau_{TU_{3ph}}^{-1} = B_{TU} \frac{\omega^2}{sinh\left(\frac{\hbar\omega}{k_B T}\right)}, \tag{E-10}$$

where $\hbar$ is the Planck constant divided by 2π and k_B is the Boltzmann constant.
This expression, while developed for *U* processes alone, is used for all high-frequency modes because Holland argues that *N* processes are weak at low temperatures and follow the U process functional form at high temperatures.

The availability of ~~"i~~sotopically enriched" samples for both silicon [20] and germanium [21] allows the unknown coefficients B_L, B_T, and B_{TU} to be determined without the potentially confounding effect of isotope scattering. The effect of boundary scattering can also be eliminated by using data taken above a sufficiently high temperature. The temperature at which boundary scattering becomes important is sample-size dependent and, for the purposes of this work, was chosen as the inflection point in the thermal conductivity versus temperature curve to the right of the low-temperature peak. For most data sets, this temperature is in the neighborhood of 100 K.

The fitting process yields the following coefficients for silicon

B_L	$= 5.7079\times10^{-24}$	s/K^3
B_T	$= 3.5353\times10^{-13}$	$1/K^4$
B_{TU}	$= 7.0609\times10^{-19}$	s

and the following coefficients for germanium

B_L	$= 2.2128\times10^{-23}$	s/K^3
B_T	$= 1.9019\times10^{-12}$	$1/K^4$
B_{TU}	$= 3.8399\times10^{-19}$	s

when the switchover from low- to high-frequency scattering for transverse modes is made at $k = 0.5$.

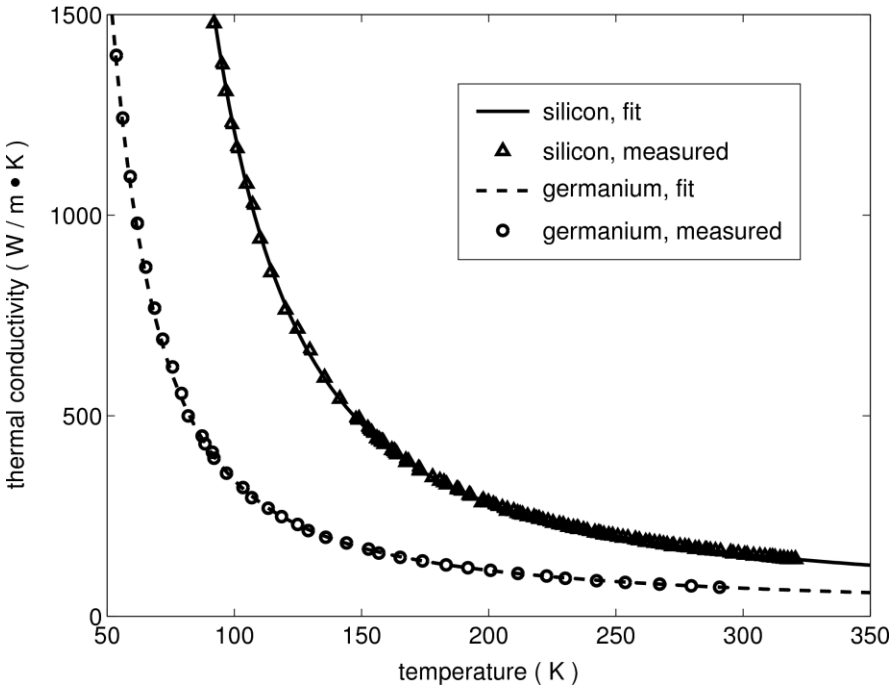

Figure E-5. Comparison of model output for thermal conductivity of isotopically enriched silicon and germanium to measured data. Germanium data is from Ozhogin [21] for 99.99% ^{70}Ge and silicon data is from Kremer [20] for 99.9829% ^{28}Si.

The thermal conductivity predicted by the model with the above coefficients are compared to the measurements in Figure E-5. Agreement is excellent across the entire temperature range.

E.4.2 Impurity Scattering

Most authors have assumed an impurity scattering (due solely to mass difference) of the form

$$\tau^{-1} = A\omega^4 \tag{E-11}$$

attributed to Klemens [22], where

$$A = \frac{a^3}{4\pi v^3} \sum_j c_j \left(\frac{\Delta M_j}{M} \right)^2 . \tag{E-12}$$

The summation in Equation E-12 is over the impurity mass, c_j is the fraction of atomic sites occupied by impurity j, and ΔM_j is the difference between its mass and the reference value M. In this equation, Klemens makes no distinction between phase and the group speed, so v is a speed to be defined (Holland [2] uses the average group speed across the acoustic branches).

In keeping with our *k*-space formulation, a form closer to that of Ziman [10] is adopted herein:

$$\tau_i^{-1} = \frac{4\pi v_g k^4}{2aM} \sum_j c_j \left(\frac{\Delta M_j}{M} \right)^2 . \tag{E-13}$$

The extra 2*M* in the denominator was inferred following fitting naturally occurring silicon and germanium using the interphonon scattering constants noted in the previous section and a free parameter in the impurity-scattering term. This formulation requires that *M* be in atomic mass units, where units are irrelevant in Equation E-12. In all calculations, the frequency and polarization-dependent group speeds shown in Figure E-4 were used in Equation E-13. It may be noted that the two formulations are identical (apart from the additional 2*M*) under Klemens' assumption of equivalent phase and group speeds.

A comparison of measured data and model output for naturally occurring silicon and germanium with impurity scattering given by Equation E-13 is shown in Figure E-6. For both materials, the thermal conductivity is somewhat underpredicted at high temperatures and distinctly overpredicted at very low temperatures. At temperatures above roughly 100 K, however, the agreement is quite good overall.

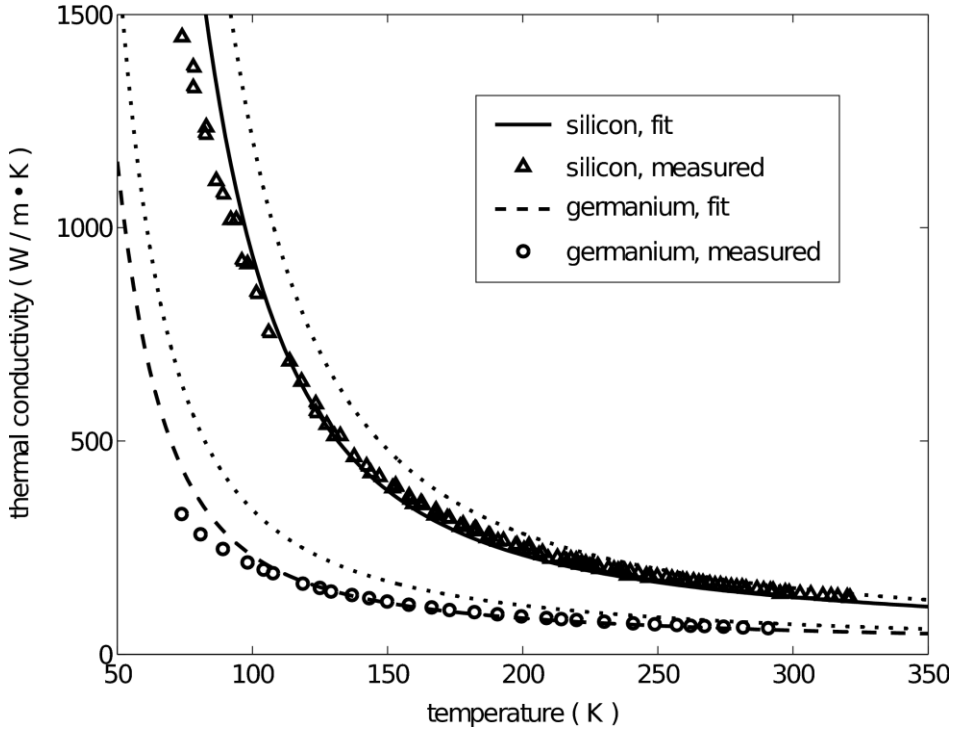

Figure E-6. Comparison of model output for thermal conductivity of natural silicon and germanium to measured data. Germanium data is from Ozhogin [21] and silicon data is from Kremer [20]. Dotted lines show isotopically enriched results from the previous figure for comparison.

E.5 References

[1] J. Callaway. –Model for lattice thermal conductivity at low temperatures," *Physical Review* 113(4): 1046–1051 (1959).

[2] M. G. Holland. –Analysis of lattice thermal conductivity," *Physical Review* 132(6): 2461–2471 (1963).

[3] K. C. Sood and M. K. Roy. –Longitudinal phonons and high-temperature heat conduction in germanium," *Journal of Physics: Condensed Matter* 5(3): 301–312 (1992).

[4] J. D. Chung, A. J. H. McGaughey, and M. Kaviany. –Role of phonon dispersion in lattice thermal conductivity modeling," *Journal of Heat Transfer* 126(3): 376–380 (2004).

[5] D. Terris, K. Joulain, D. Lemonnier, and D. Lacroix. –Modeling semiconductor nanostructures thermal properties: The dispersion role," *Journal of Applied Physics* 105(7): 073516 (2009).

[6] R. Yang and G. Chen. –Thermal conductivity modeling of periodic two-dimensional nanocomposites," *Physical Rev. B* 69(19): 195316 (2004).

[7] S. Mazumder and A. Majumdar. –Monte Carlo study of phonon transport in solid thin films including dispersion and polarization," *Journal of Heat Transfer* 123(4): 749–759 (2001).

[8] O. Essner, P. Dollfus, S, Galdin-Retailleau, and J. Saint-Martin. –Improved Monte Carlo algorithm of phonon transport in semiconductor nanodevices," *Journal of Physics: Conference Series* 92: 012079 (2007).

[9] L.-C. Liu, M.-J. Huang, R. Yang, M.-S. Jeng, and C.-C. Yang. –Curvature effect on the phonon thermal conductivity of dielectric nanowires," *Journal of Applied Physics* 105(10): 104313 (2009).

[10] J. M. Ziman. *Electrons and Phonons; The theory of transport phenomena in solids. The international series of monographs on physics*. Clarendon Press, Oxford, 1960.

[11] C. Kittel. *Introduction to Solid State Physics*. Wiley, New York, 7th edition, 1996.

[12] A. Majumdar. –Microscale heat conduction in dielectric thin films," *Journal of Heat Transfer* 115: 7–16 (1993).

[13] E. S. Piekos, S. Graham, and C.C. Wong. –Multiscale thermal transport," Technical Report SAND2004-0531, Sandia National Laboratories, Albuquerque, New Mexico (2004).

[14] E. Pop, R. W. Dutton, and K. E. Goodson. –Analytic band Monte Carlo model for electron transport in Si including acoustic and optical phonon dispersion," *Journal of Applied Physics* 96(9): 4998–5005 (2004).

[15] B. N. Brockhouse. "Lattice vibrations in silicon and germanium," *Physical Review Letters* 2(6): 256–258 (1959).

[16] G. Nilsson and G. Nelin. "Study of the homology between silicon and germanium by thermal-neutron spectrometry," *Physical Review B* 6(10): 3777–3786 (1972).

[17] P. Giannozzi, S. de Gironcoli, P. Pavone, and S. Baroni. "*Ab initio* calculation of phonon dispersions in semiconductors," *Physical Review B* 43(9): 7231–7242 (1991).

[18] G. Nilsson and G. Nelin. "Phonon dispersion relations in Ge at 80 ◦K," *Physical Review B* 3(2): 364–369 (1971).

[19] C. Herring. "Role of low-energy phonons in thermal conduction," *Physical Review* 95(4): 954–965 (1954).

[20] R. K. Kremer, K. Graf, M. Cardona, G. G. Devyatykh, A. V. Gusev, A. M. Gibin, A. V. Inyushkin, A. N. Taldenkov, and H.-J. Pohl. "Thermal conductivity of isotopically enriched ^{28}Si: Revisited," *Solid State Communications* 131(8):499–503 (2004).

[21] V. I. Ozhogin, A. V. Inyushkin, A. N. Taldenkov, A. V. Tikhomirov, G. E. Popov, E. Haller, and K. Itoh. "Isotope effect in the thermal conductivity of germanium single crystals," *Journal of Experimental and Theoretical Physics Letters* 63(6):490–4 (1996).

[22] P. G. Klemens. "Thermal conductivity and lattice vibrational modes," In F. Seitz and D. Turnbull, editors, *Solid State Physics* 7:1–98. Academic Press, NY (1958).

Appendix F. Phonon Transport Along Interfaces: Monte Carlo Simulation of Structures for Assessing Phonon-Surface Interaction

Designed to operate in a regime where continuum codes are invalid, but too large to be accessible to molecular dynamics (MD) techniques, the test ligaments in the differential surface-scattering assessment structure described in Section 3 are modeled under the ―phonon gas" assumption. Under this assumption, phonon transport is governed by the Boltzmann equation. The solution scheme employed in this work most closely resembles the method known as direct simulation Monte Carlo (DSMC). This technique was developed by Bird [1] for simulating gas behavior surrounding reentry vehicles at high altitude, where the continuum assumption breaks down. Later analysis showed rigorously the relationship between DSMC and the Boltzmann equation [2], and it has been employed in flows ranging from free molecular to fully continuum [3, 4].

Mazumder and Majumdar [5] published the first application of a similar technique to phonons in 2001. The simulation tool employed in the current work, described in detail previously [6], draws from Mazumder and Majumdar as well as Bird. The relaxation time-based scattering model is a modified version of Holland's model [7] with new coefficients fit to the thermal conductivity of both natural and isotopically enriched silicon, as described in Appendix E.

F.1 Simulation Parameters

The simulation domain consists of either a bent or straight ligament and a small portion of the platforms on either side of it, as shown in Figure F-1. Due to the very large thickness (2 μm) compared to width (100 nm) of the ligaments, the simulations are performed in only the two spatial dimensions shown in Figure F-1. An isothermal boundary condition is enforced on the three ―internal" edges of the platform sections. An adiabatic boundary condition, with a varying specularity parameter, is enforced on the free edge of the platform section (where the ligament attaches) as well as along the edges of the ligament.

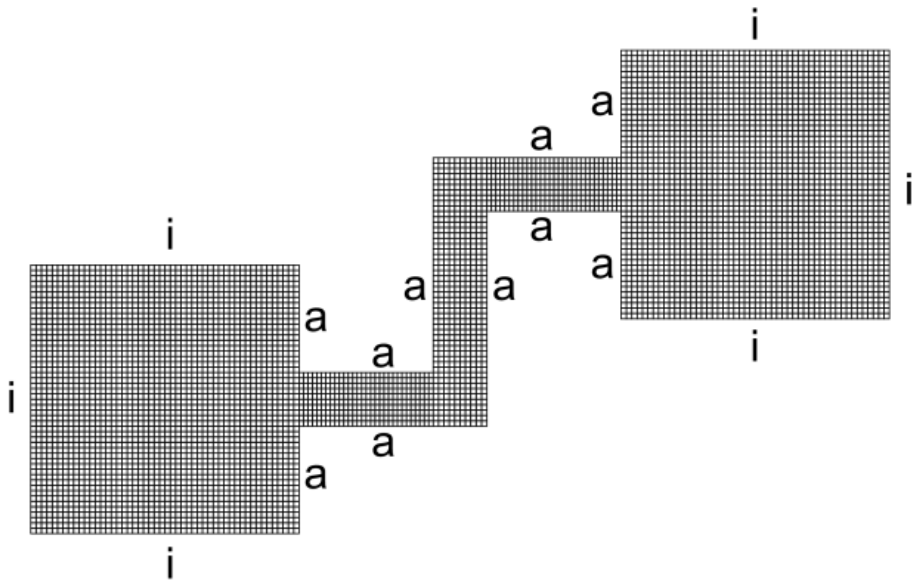

Figure F-1. Computational domain showing a bent ligament and portions of the platforms on either side. The grid used for all simulations is also shown. Boundary conditions on each face are marked with an 'i' for isothermal and an 'a' for adiabatic.

The simulation grid of uniform, 100 nm square cells is also shown in Figure F-1. While the numerical technique allows the cell size to be enlarged as the temperature decreases due to the increasing phonon mean free path, the grid shown is employed for all simulations presented herein. This grid size was set conservatively at the highest temperature, so it is very conservative at the lowest temperature. The target particle count is set at two million for all simulations. This target provides approximately three hundred particles per cell, which is also conservative.

F.2 Results

A temperature distribution for the complete domain of a bent ligament at 200 K with specular reflection is shown in Figure F-2. A key feature of note in these results is that the temperature varies very little across the narrow dimension of the ligament. This fact is exploited herein by averaging the observed temperature in cells across the ligament when computing a temperature distribution. This increases the effective number of samples embodied in the reported temperature by a factor of 10.

An in-plane flux distribution for the complete domain of a straight ligament with diffuse reflection at 200 K is also shown in Figure F-2. The in-plane flux is computed by computing a vector magnitude from the average energy times speed reported by the simulation in the two spatial directions shown in Figure F-1. In this figure, the parabolic profile expected in pressure-driven fluid flows in channels (Poiseuille flow) is visible. Also in parallel with viscous fluids, an ~~–e~~ntrance region" is visible at the high-temperature end of the ligament, where the velocity distribution transitions from uniform to parabolic across the channel as the boundary layers from each wall grow and coalesce.

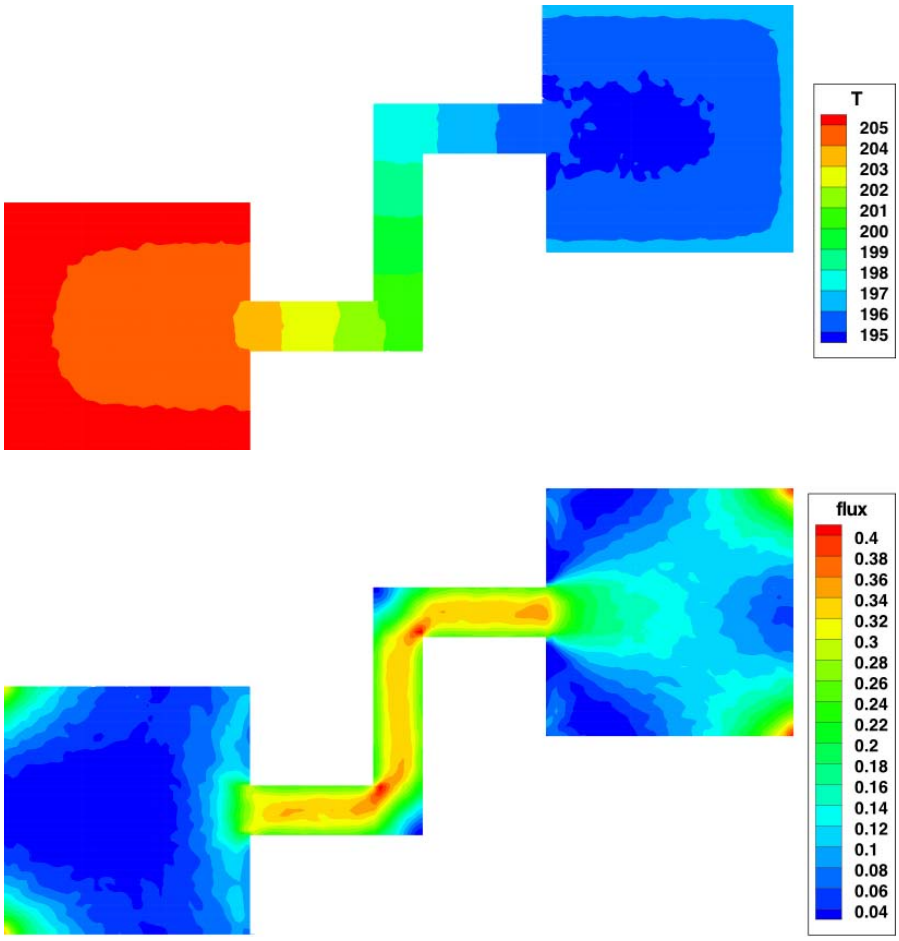

Figure F-2. (Color online) Temperature and flux distributions for the bent ligament at 200 K with fully diffuse reflection on adiabatic walls. Temperature units are K and flux units are GW/m^2.

A comparison of flux distributions for the straight and bent ligaments at 200 K with either fully specular or fully diffuse surface interaction is shown in Figure F-3. In both cases, the straight ligament is shown to have a greater net flux. Confirming the operating principle of the measurement device, the difference in net flux between the ligaments is greater for the specular case, where the straight channel walls have no effect on the tangential momentum of traversing phonons.

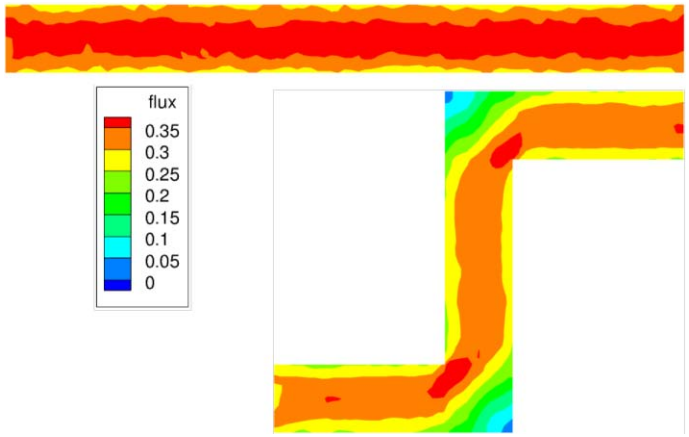

(a) diffuse reflection

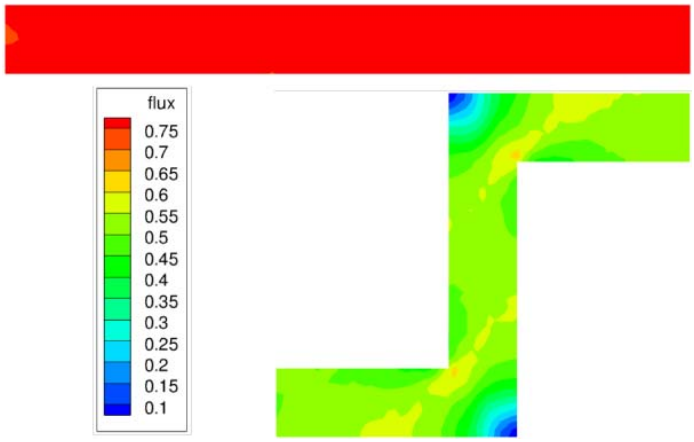

(b) specular refection

Figure F-3. (Color online) Comparison of flux distributions between the straight and bent ligaments for fully diffuse and fully specular reflections at 200 K.

In order to explore the operation of this device over a range of specularity parameters and temperatures, a more convenient means of comparison is desirable. Toward this end, it is asserted that an effective thermal conductivity can be defined for the ligaments, despite the fact that they operate in a noncontinuum regime and thermal conductivity is an inherently continuum parameter.

The effective thermal conductivity for each case is computed by dividing the net flux through the ligament, measured at its isothermal surfaces, by a temperature gradient measured in its interior. This temperature gradient is found by fitting a straight line to the cross-ligament averaged temperature over a region centered on the ligament midpoint. To maintain parity between the straight and bent ligaments, the size of this region is set at 300 nm. This choice corresponds to the portion of the vertical segment of the bent ligament with adiabatic boundaries on both sides.

It is expected that the most challenging case for determining an effective thermal conductivity will be the straight ligament with fully specular reflections at the lowest

temperature. In this case, phonon scattering by surfaces and other phonons is minimized, making it difficult to reach a local equilibrium. The temperature distribution for the complete ligament, along with the fit computed from data in the 300 nm center region is presented in Figure F-4. While significant nonlinearity is indeed visible at the ends, the center third is well approximated by a linear fit.

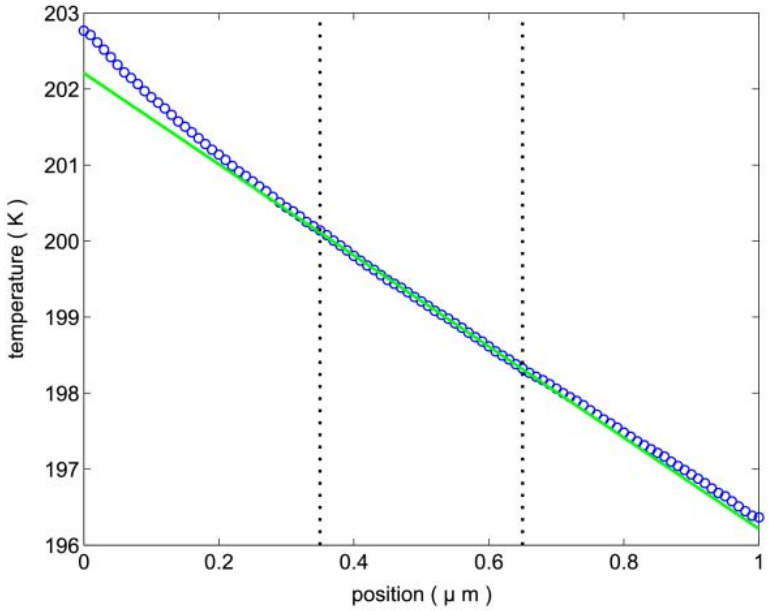

Figure F-4. Temperature distribution and linear fit for the straight ligament at 200 K. The dotted lines bound the region included in the fit.

A check on the validity of the ~~"e~~effective thermal conductivity" formulation may be made by repeating the process with a different temperature gradient to ensure that the result is independent of this parameter, as required by Fourier's law. For a 10 K and 5 K temperature difference across the ligament, the computed thermal conductivities were found to differ by only 2%, so this requirement appears to be satisfied.

The difference in effective thermal conductivity between the straight and bent ligaments is shown Figure F-5. Several key features of the differential arrangement are visible in this figure. First, the results are presented as the effective thermal conductivity of the bent ligament subtracted from that of the straight ligament. Because the straight ligament provides an opportunity for phonon travel without surface interactions that is absent in the bent ligament, this difference is expected to be always positive. The data do not contradict this expectation. Second, for all temperatures, the difference between the straight and bent ligaments increases with the specularity parameter. This behavior may be explained by noting that specular reflections do not destroy tangential momentum, thus they provide no resistance to flow parallel to a surface. Under purely specular reflection, therefore, a surface can only provide resistance by assuming an orientation with a component perpendicular to the flow direction, so the sensitivity to geometry is maximized. Third, for similar reasons, the difference in thermal conductivity between the straight and bent ligaments increases as the temperature decreases. In this case, increasing

sensitivity to geometry is caused by weakening interphonon interactions, which are also destroyers of tangential momentum.

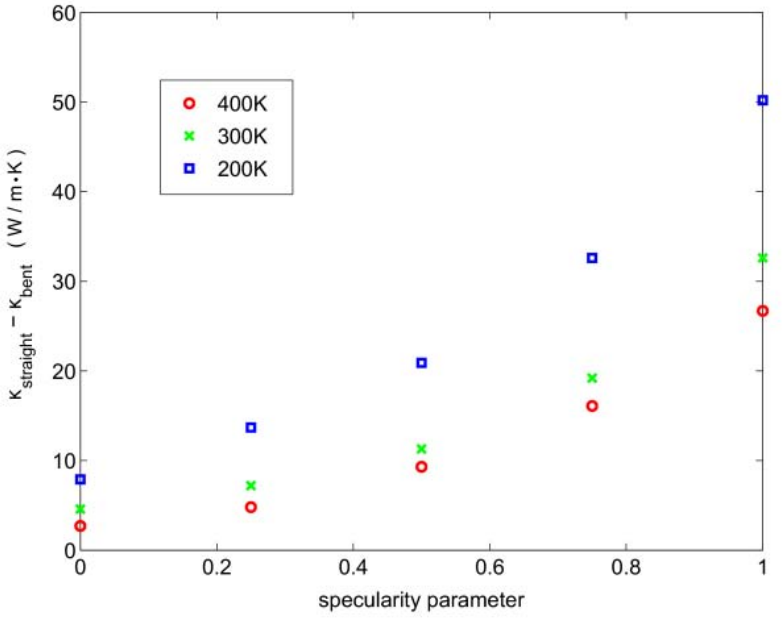

Figure F-5. Effective thermal conductivity difference between the straight and bent ligaments as a function of specularity parameter and temperature.

Normalizing the data of Figure F-5 by the temperature-dependent bulk thermal conductivity yields the results shown in Figure F-6. For diffuse reflections in particular, the normalization produces a remarkable collapse of the data. This behavior may be explained by considering the kinetic theory-based expression for thermal conductivity:

$$\kappa = \frac{1}{3} C v \lambda, \tag{F-1}$$

where C is the volumetric heat capacity, v is the average phonon group speed, and λ is the average phonon mean free path [8, 9]

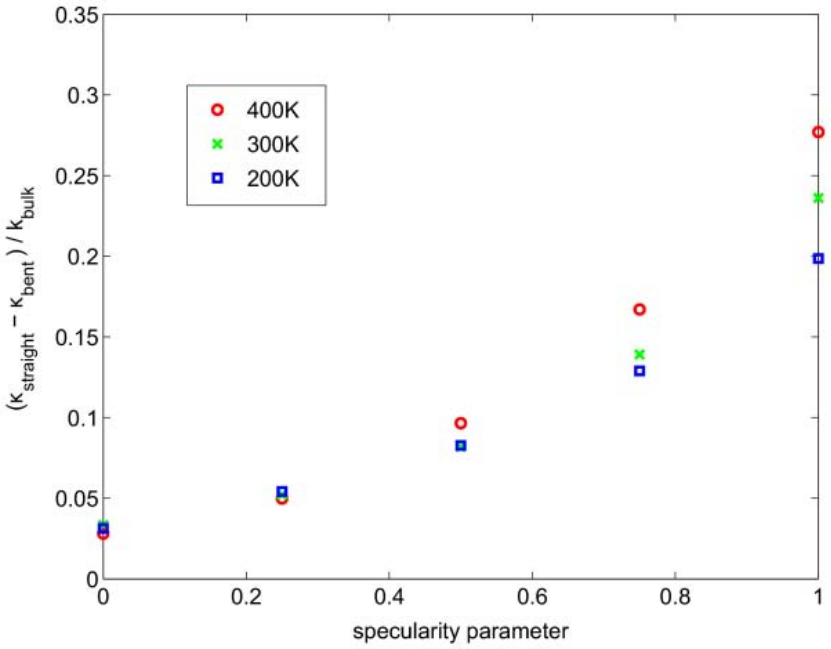

Figure F-6. Effective thermal conductivity difference between the straight and bent ligaments as a function of specularity parameter and temperature, normalized by the bulk thermal conductivity at the specified temperature.

Under the dispersion model used in the simulations, the group velocity is assumed zero for optical modes and transverse acoustic modes with reduced wave numbers greater than 0.913 [10]. Consequently, these modes, usually included in the heat capacity, disappear when the average of the heat capacity times the group speed is computed on a mode-by-mode basis. The results of such a computation are shown in Figure F-7. From this figure, it may be observed that the average *Cv* increases by about 20% between 200 K and 400 K. The thermal conductivity, however, decreases by a factor of 2.6 over this temperature range. It may therefore be concluded from Equation F-1 that the thermal conductivity in this temperature range is primarily controlled by the mean free path.

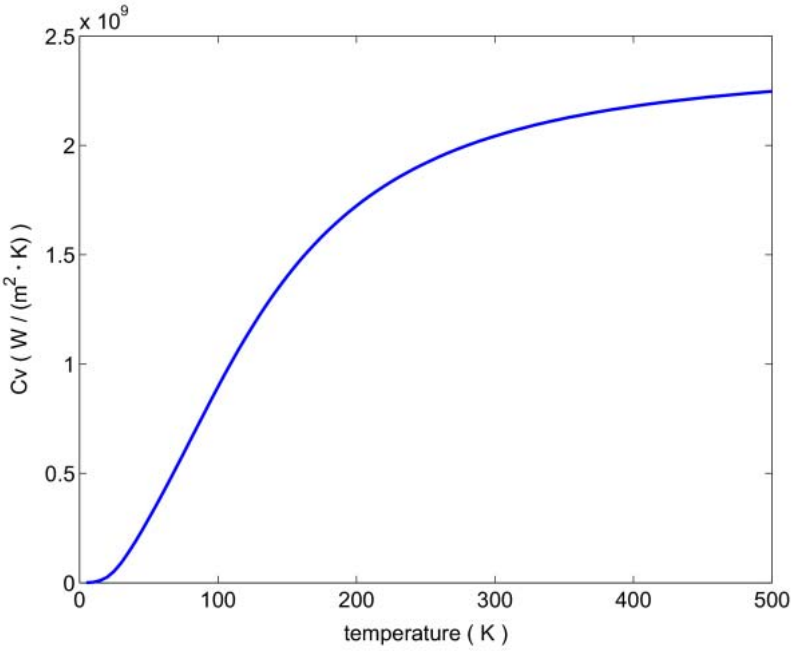

Figure F-7. Volumetric heat capacity times phonon group speed under the dispersion model used in the simulations.

The mean free path may be expressed as

$$\lambda = v\tau, \tag{F-2}$$

where τ is the relaxation time. The relaxation time may be divided into two components τ_i and τ_b that represent the relaxation times due to "intrinsic" (i.e., interphonon, impurity, and defect) and "boundary" scattering, respectively. It is expected that τ_i will be a reasonably strong function of temperature while τ_b will be a reasonably weak function of temperature. With these definitions, and using Matthiessen's rule to combine the relaxation times for each ligament (*B* for bent and *S* for straight), the thermal conductivity difference for the structure may be expressed as

$$\kappa_S - \kappa_B = \frac{\frac{1}{3}Cv^2\left(\frac{1}{\tau_{b_B}} - \frac{1}{\tau_{b_S}}\right)}{\left(\frac{1}{\tau_i} + \frac{1}{\tau_{b_B}}\right)\left(\frac{1}{\tau_i} + \frac{1}{\tau_{b_S}}\right)}. \tag{F-3}$$

Equation F-3 captures two key trends shown in Figure F-5. First, the positivity of $\kappa_S - \kappa_B$ implies that $\tau_{b_S} > \tau_{b_B}$, which, as noted previously, is intuitively expected because phonons traversing the straight structure will have, on average, fewer surface interactions so they will take longer to relax. Second, the decrease in $\kappa_S - \kappa_B$ with temperature observed in Figure F-5 is a

consequence of the well-known decrease in τ_i with temperature, increasing both terms in the denominator sufficiently to overpower the increase in *Cv* with temperature.

Normalizing by the bulk thermal conductivity eliminates the factor $\frac{1}{3}Cv^2$ and introduces an additional τ_i in the denominator. After some rearrangement, the resulting expression becomes

$$\frac{\kappa_S - \kappa_B}{\kappa_{bulk}} = \frac{\frac{1}{\tau_{b_B}} - \frac{1}{\tau_{b_S}}}{\frac{1}{\tau_i} + \frac{1}{\tau_{b_B}} + \frac{1}{\tau_{b_S}} + \frac{\tau_i}{\tau_{b_B}\tau_{b_S}}}. \tag{F-4}$$

Under the assumptions employed herein, temperature independence of the thermal conductivity difference normalized by bulk thermal conductivity implies that the terms involving τ_i in Equation F-4 are insignificant, particularly in comparison to their effect in Equation F-3. The breakdown of this normalization as the specularity parameter increases suggests that the dominance of boundary scattering is lost with increasing specularity, which is expected because it may be argued that boundary scattering at the specular limit has no ability to restore equilibrium in the straight ligament. The term τ_{b_S} therefore tends to infinity, leaving only τ_i and τ_{b_B} in the denominator of Equation F-3. Due to geometric effects, τ_{b_B} remains finite in this limit, but its dominance over τ_i is lost, so the result becomes temperature dependent. Because τ_i decreases with increasing temperature, Equation F-4 predicts that the normalized conductivity difference at the specular limit should decrease with increasing temperature. Figure F-6 shows the opposite trend, which highlights the limits of this simple analysis and the assumption of a temperature-independent τ_b.

It is interesting to note that the above formulation, when applied to the quotient κ_B/κ_S used by Liu et al. [11] in the study of curved nanowires, yields

$$\frac{\kappa_B}{\kappa_S} = \frac{\tau_{b_B}}{\tau_{b_S}} \tag{F-5}$$

in the limit of $\tau_b << \tau_i$. These authors showed that κ_B/κ_S varied only 2% when the wire thickness was increased from 10 nm to 56 nm with diffuse reflection at the adiabatic surfaces. Equation F-5 implies that τ_{b_B}/τ_{b_S} is insensitive to thickness in this case. This observation is likely true for the geometry treated herein as well, but examination of this issue will be left for future work.

F.3 Conclusions

Monte Carlo simulations have shown that a differential measurement of thermal transport through a bent and straight ligament is sensitive to the extent to which phonon-surface

interactions tend to destroy tangential momentum (i.e., the specularity parameter). Normalizing the difference in effective thermal conductivity between these ligaments by the bulk value at the mean temperature yields a remarkable collapse of the data. Noting that the variation of the bulk thermal conductivity in the temperature range of interest is dominated by the mean free path, this observation provides evidence that the chosen design forces a difference in the number of surface interactions experienced by phonons traversing the straight and bent ligaments, as intended.

F.4 References

[1] G. A. Bird. *Molecular Gas Dynamics and the Direct Simulation of Gas Flows*. Oxford Engineering Science. Oxford University Press, New York, NY (1994).

[2] W. Wagner. ―A convergence proof of Bird's direct simulation Monte Carlo method for the Boltzmann equation," *Journal of Statistical Physics* 66(3–4): 1011–1044 (1992).

[3] E. S. Oran, C. K. Oh, and B. Z. Cybyk. ―Direct simulation Monte Carlo: Recent advances and applications," *Annual Review of Fluid Mechanics* 30: 403–441 (1998).

[4] J. M. Reese, M.A. Gallis, and D.A. Lockerby. ―New directions in fluid dynamics: non-equilibrium aerodynamic and microsystem flows," *Philosophical Transactions of the Royal Society A* 361(1813): 2967–2988 (2003).

[5] S. Mazumder and A. Majumdar. ―Monte Carlo study of phonon transport in solid thin films including dispersion and polarization," *Journal of Heat Transfer* 123(4):749–759 (2001).

[6] E. S. Piekos, S. Graham, and C. C. Wong. ―Multiscale thermal transport," Technical Report SAND2004-0531, Sandia National Laboratories, Albuquerque, New Mexico, 2004.

[7] M. G. Holland and L. J. Neuringer In *Proceedings of the International Conference on the Physics of Semiconductors, Exeter 1962*, page 475, London, 1962. The Institute of Physics and the Physical Society, London.

[8] J. M. Ziman. *Electrons and Phonons: The Theory of Transport Phenomena in Solids*. The international series of monographs on physics. Clarendon Press, Oxford, 1960.

[9] C. Kittel. *Introduction to Solid State Physics*. Wiley, New York, 7th edition, 1996.

[10] E. S. Piekos. ―A modified Holland model for Monte Carlo simulation of silicon and germanium," to be published.

[11] L.-C. Liu, M.-J. Huang, R. Yang, M.-S. Jeng, and C.-C. Yang. ―Curvature effect on the phonon thermal conductivity of dielectric nanowires," *Journal of Applied Physics* 105(10): 104313 (2009).

Distribution

External

Dr. Sylvie Aubry
Stanford University - Ms 4040
Mechanics and Computation Group
Department of Mechanical Engineering
Durand Building, Room 201. Stanford, CA 94304

David Hurley
Idaho National Laboratory
P.O. Box 1625
Idaho Falls, ID 83415-2209
(208) 526-3665

Internal

1	0346	E. S. Piekos	
1	1415	T. A. Friedmann	
1	1304	J. P. Sullivan	
1	0352	S. L. Shinde	
1	1415	D. E. Peebles.	
1	1833	J. A Emerson	
1	1421	J. A Simmons	
1	1078	W. L. Hermina	
1	1415	D. R. Sandison	
1	0885	J. E. Johannes	
1	9161	S. W. Allendorf	
1	1315	R. Q. Hwang	
1	1427	J. M. Phillips	
1	0899	Technical Library	9536 (electronic)
1	0123	D. Chavez	1011